University of Latvia
Faculty of Physics and Mathematics

Heat and mass transfer in electromagnetically driven recirculated turbulent flows

Andrejs Umbraško

Advisor: Dr. Phys. Andris Jakovičs

A thesis submitted for the degree of

Doctor of Philosophy (Physics)

Riga, 2010

Abstract

This work is devoted to the problem of heat and mass transfer processes in the turbulent recirculated liquid metals flows driven by the electromagnetic forces. This kind of flows often takes place in various practical applications like melting of metals and alloys. Experimental investigations using physical model of induction furnace have shown that the flows are unstable and large amplitude low-frequency oscillations were revealed by velocity measurements. However, the existing turbulence modeling approaches were not able to calculate correct temperature distribution for mentioned flow types.

Extended numerical and experimental studies have been performed for three different types of induction furnaces, where the velocity profiles and temperature fields were examined. The modelling results of the crucible induction furnace have shown the necessity for the adequate simulation of the low-frequency oscillations observed in the experiment, while the model of the induction crucible furnace gave the possibility to study thoroughly the characteristics of these flow instabilities. The new modelinfg approach based on Large Eddy Simulation technique has been applied in order to capture this phenomenon numerically, since traditional two-equation turbulence models do not provide necessary opportunities. The measurements and numerical calculations of the model induction crucible furnace, which were focused on the specific parameters of the low-frequency oscillations, gave the possibility to improve the proposed modeling method and also to determine its application possibilieties.

The LES technique has been further applied for the modelling of the Aluminium and Titan-Aluminium melting process in the induction furnace with the cold crucible. The corresponding temperature and velocity measurements have been done in Aluminium melt. The fully three-dimensional electromagnetic analysis of the installation has been used as a base for the transient three-dimensional coupled hydrodynamic and thermal calculations. The parameter study has been performed in order to derive the tendencies for possible optimization of the melting process in induction furnace with cold crucible.

Contents

List of Figures

Nomenclature

Roman Symbols

$\boldsymbol{A}$	Magnetic vector potential
$\boldsymbol{B}$	Magnetic flux density vector
$\boldsymbol{E}$	Electric field strength vector
$\boldsymbol{F}$	Lorentz force density
$\boldsymbol{H}$	Magnetic field strength vector
$\boldsymbol{J}$	Current density vector
$\boldsymbol{J}_B$	Induced current density
$\boldsymbol{v}$	Fluid velocity
c	Speed of light
c_p	Specific heat
f	Frequency of electric current
g	Gravitational acceleration
h	Enthalpy
k	Turbulent energy
p	Fluid pressure

Q Joule heat density

Greek Symbols

δ Electromagnetic field penetration depth

ϵ Turbulent energy dissipation rate

γ Surface tension coefficient

λ Thermal conductivity

μ Fluid dynamic viscosity

μ_r Relative magnetic permeability

μ_0 Magnetic permeability of space

Φ Magnetic scalar potential

π $\simeq 3.14\ldots$

σ Electrical conductivity

σ_t Turbulent Prandtl number

ε Emissivity coefficient

1 Introduction

The recirculated flows, which are driven by the electromagnetic forces (Lorentz forces), are observed in many industrial processes, especially in the induction furnaces for melting of metals (Fig. 1.1). Today industrial processes often are significantly multi-physical and their research should include several physical disciplines. Typical examples are induction furnaces for melting of metals. Their efficient design is impossible without understanding of processes which take place in these installations. There has been a lot of investigations devoted to the study of electromagnetic and thermal problems only, but in most cases when we deal with liquid metal the hydrodynamic part of analysis can not be neglected. The temperature distribution and chemical alloy composition are heavily influenced by melt convective motion, therefore the knowledge of the flow characteristic parameters allows optimizing the homogenization of the melt and improve the quality of the end product. The experimental studies of these processes are usually limited or even impossible due to the complications with access to the area of interest because of high temperatures and chemical hostility of the material. Hence, the numerical modeling often is the only possibility to perform such kind of investigations.

Fluid flow and transfer processes in industrial metallurgical installations have become a subject of numerical modeling many years ago. Melting of alloys in cylindrical induction crucible furnaces can be mentioned as a wide spread example. This process can be approximated with two-dimensional (2D) model due to its axial-symmetric geometry and averaged flow pattern in these installations, which is formed by the influence of electromagnetic forces, usually comprises of two or more toroidal dominating recirculating vortices. At the same time, together with *prima facie* simplicity, the high-Reynolds-number flow leads to turbulence. That's why, despite the axis-symmetric geometry, which allows using

2D electromagnetic and thermal models, the hydrodynamic processes have three-dimensional character and require 3D modeling. This fact, in the absence of a universal and always reliable modeling approach and presence of wide choice of non-universal turbulence schemes, turns it into a non-trivial problem up to now. There are three main approaches to turbulence modeling:

- turbulent viscosity models, when only time-averaged flow is resolved, but all turbulence scales are modeled;
- direct numerical simulation (DNS), when all scales down to dissipative ones are resolved on extremely fine mesh and with appropriately small time-step;
- large eddy simulation (LES), when mesh size defines which scales are resolved and which are modeled.

The DNS scheme remains unusable for practical applications up to present day because of significant requirements for computational resources. The mesh size grows as $Re^{2.25}$, which gives more than a billion nodes for typical industrial scale flow with $Re > 10^4$. The computer memory needed to store only the main four single precision variables exceed 150 GBytes, what may be is not completely unrealistic, considering modern computational clusters capabilities, but certainly is not cost-effective solution. Therefore, the choice should be done between two other possibilities for industrial applications.
Flow patterns obtained with two-dimensional solvers based on Reynolds Averaged Navier-Stokes (RANS) equations usually are in good agreement with estimated and measured time-averaged flow velocity values. However, also the temperature field and admixtures' concentration is often object of interest. The spatial distribution of the temperature and alloys compound concentration depends strongly on the heat and mass exchange between vortices of mean flow. When only the time-averaged flow is modeled, the heat flux in the direction normal to stream lines is proportional to the material's physical and additional turbulent thermal conductivity. The same is valid for mass transfer due to diffusivity. Therefore, the reliability of the simulation result is strongly connected with the adequate modelling of the turbulent properties of the flow.

Our numerical investigations show that two-equation turbulence models, e.g. k-e and others based on Reynolds Averaged Navier-Stokes (RANS), fail to describe correctly the heat and mass transfer processes between the main vortices, when standard parameters set is used. The examination of the roots of this failure reveals, that the calculated turbulent quantities are very different from expected ones, especially in the zone of vortices interaction. After the expectations based on the experimental data, there is a lot of turbulent movement in this zone, while discussed models predict very low turbulence between the vortexes and relatively high in the vortices' centers. However, these models could be adjusted for every kind of particular flow situation, but it is not always acceptable, especially, when experimental data are not available for comparison. Hence, it is necessary to investigate advanced simulation methods for more generic and, therefore, flexible solutions.

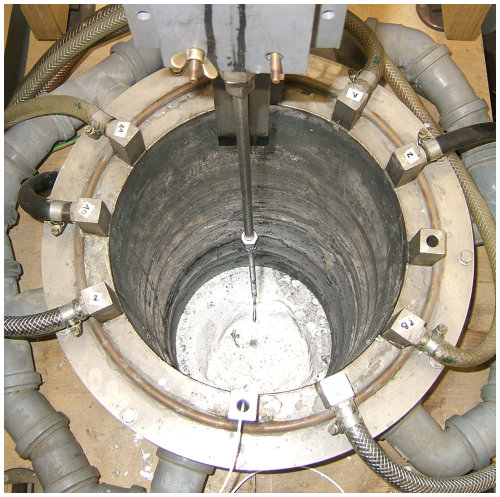

Figure 1.1: Experimental induction furnace installed in the Institut for Electrotechnology Leibniz University of Hanover

Nowadays, due to the permanent growth of accessible high-power computational resources, it is possible to run more complicated transient and three-dimensional (3D) numerical calculations of fluid dynamic problems using advanced turbulent models with higher time and mesh resolution requirements and to get reliable results in reasonable time. The becoming more and more popular LES model satisfies the flexibility and usability requirements set by industrial applications. Main advantages of this approach come from the its main feature, that the turbulent motion is replaced with sub-grid (turbulent) viscosity only for the scales, which are smaller, than the mesh size. Therefore, it is possible to resolve the fluid motion from the macroscale of dominating flow structures down to the meso-/upper micro- scale, depending on the finite element volume or, in

other words, available computational resources. This naturally includes effects of non-isotropic turbulence, which are covered in RANS based models with set of additional equations and model coefficients.

Present work is focused on the research of the recirculated flows, using numerical tools as well as experimental investigations. Special attention is devoted to the heat and mass transfer processes. Each chapter contains experimental and numerical results obtained for the laboratory or industrial installation, where recirculated flow has important influence on the process.

The objectives of this work are:

- Examine the possibilities of the modelling of the transfer processes using available computational tools and resources. Most actual turbulence models have high demands for the mesh quality and computational resources and this sets the limits of the model physical dimensions. Therefore, it is important to investigate the applicability of this modelling technique to the practical problems.

- Verify the modelling results for model induction furnaces using vollected experimental data. The comparison of the measured and simulated velocity and temperature distribution can be supplemented by the characteristics of the flow oscillations, which can not be modeled with the RANS based models.

- Examine the possibilities of the developed numerical simulation method for modelling of practical applications, where large flow vortices are dominant in transfer processes.

The theoretical background occupies first chapter. The modelling techniques of liquid metal flows in induction furnaces are presented together with description of numerical tools used for this calculations.

The second chapter shows what brings the transient simulation of oscillating flow in terms of energy transfer on the example of crucible induction furnace. Due to the specifics of this furnace, the heat exchange between recirculating flow structures has determinative importance for achieving correct results. Comparison with the experimental data are also provided.

The third chapter describes the widely used induction crucible furnace, which has simple cylindrical geometry, and relatively trivial flow pattern The main differences between the RANS and LES modeling outcomes is shown and accomplished by the results of experiments. The smooth pattern of RANS simulation appears to hide beneath itself highly oscillating flow, where the symmetry can be seen only after long-period time-averaging of transient results.

The induction furnace with cold crucible, which is described in the fourth chapter, is more challenging for the numerical modeling due to presence of several additional physical effects, like distinctive free surface deformation in electromagnetic field and solidification/melting interface inside the melt. Also, this installation cannot be unconditionally considered as axis-symmetric, already from the initial stage of electromagnetic modeling because of slit crucible wall. The advantages brought by LES model, such as adequate estimation of mass and heat transfer in recirculating flows, allow in perspective to simulate accurately the composition changes of alloys during directional solidification process.

2 Theoretical background and properties of numerical modeling of electromagnetically driven liquid metal flows

2.1 Electromagnetic systems and their numerical modeling

The present work deals with liquid metals flows, which are driven mainly by electromagnetic forces. This kind of flows are often observed in various metallurgical processes of different scale: from experimental centimeter-sized installations for melting of high-purity alloys up to industrial furnaces with several meter in diameter. They have in common that the melt moves in closed domain without inlets and outlets and this domain has relatively stable form for considered period of time. The energy is supplied to the system through the inductor, which usually has form of a coil with several turns, with an alternating harmonic electric current: $\boldsymbol{J}_I = \boldsymbol{J}_0 sin(\omega t)$ (Fig.2.1). The electromagnetic field is induced and it spreads out accordingly to the Maxwell equations:

$$\nabla \cdot \boldsymbol{E} = 0 \tag{2.1}$$

$$\nabla \cdot \boldsymbol{B} = 0 \tag{2.2}$$

$$\nabla \times \boldsymbol{E} = -\frac{\partial \boldsymbol{B}}{\partial t} \tag{2.3}$$

$$\nabla \times \boldsymbol{B} = \mu_0 \boldsymbol{J} + \mu_0 \epsilon_0 \frac{\partial \boldsymbol{E}}{\partial t} \tag{2.4}$$

It is considered, that there are no free electrical charges ρ in the domain.

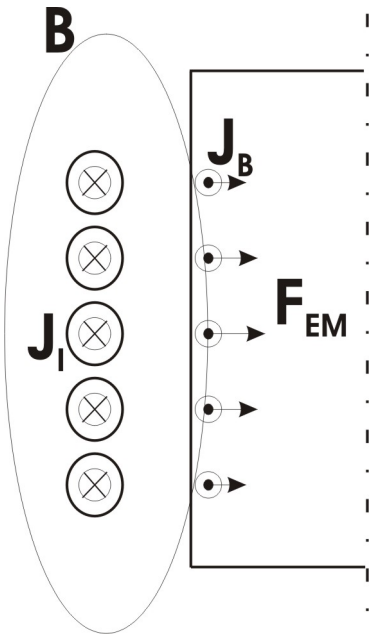

Figure 2.1: Sketch of the axis-symmetric induction system.

Taking into account Ohm's law,

$$\boldsymbol{J} = \sigma(\boldsymbol{E} + \boldsymbol{v} \times \boldsymbol{B}), \tag{2.5}$$

this equation system can be reduced to two equations for $\boldsymbol{B}$:

$$\nabla \cdot \boldsymbol{B} = 0 \tag{2.6}$$

$$\nabla \times \nabla \times \boldsymbol{B} = \mu_0 \sigma(-\frac{\partial \boldsymbol{B}}{\partial t} + \nabla \times \boldsymbol{v} \times \boldsymbol{B}) \tag{2.7}$$

Since 2.2, it is possible to write

$$\boldsymbol{B} = \nabla \times \boldsymbol{A}, \tag{2.8}$$

where $\boldsymbol{A}$ is vector-potential of the electromagnetic field. Therefore, the 2.3 can be written as:

$$\nabla \times \boldsymbol{E} = -\nabla \times \frac{\partial A}{\partial t} \tag{2.9}$$

or, after integration:

$$\boldsymbol{E} = -\frac{\partial \boldsymbol{A}}{\partial t} - \nabla \cdot \Phi, \tag{2.10}$$

where Φ is scalar potential. Putting together 2.8, 2.10 and 2.4 into 2.5 and neglecting displacement currents we receive an equation for magnetic potentials:

$$\frac{\partial \boldsymbol{A}}{\partial t} = \frac{1}{\mu_0 \sigma} \Delta \boldsymbol{A} - \nabla \Phi + \boldsymbol{v} \times \nabla \times \boldsymbol{A} \tag{2.11}$$

where the expression $\nabla \times \nabla \times \boldsymbol{A} = \nabla(\nabla \boldsymbol{A}) - \Delta \boldsymbol{A}$ and the fact that divergence of vector potential is zero are used. Last term on the right side of 2.11 usually is neglected due to its insignificance in the examined flow. Considerable magnetic field penetrates into the melt only in the depth of skin layer, but in this region the vector product of the $\boldsymbol{v}$ and $\nabla \times \boldsymbol{A}$ is very small, because both $\boldsymbol{v}$ and $\boldsymbol{B}$ are parallel to the wall and to each other. Therefore, we can write:

$$\frac{\partial \boldsymbol{A}}{\partial t} = \frac{1}{\mu_0 \sigma} \Delta \boldsymbol{A} - \nabla \Phi \tag{2.12}$$

The mentioned skin layer depth shows how far magnetic field diffuse into the conducting medium and it depends on the coefficient before the first term on the right side of 2.12 and frequency of the oscillating electromagnetic field:

$$\delta = \sqrt{\frac{1}{\pi f \sigma \mu_r \mu_0}}. \tag{2.13}$$

In the field of induction applications, this parameter may vary from several centimeters (low-frequency currents and/or low-conducting materials) down to the parts of millimeter (high-frequency currents and/or high-conducting materials). The magnetic field density in the skin layer usually has values of order 10^{-1} T and the current density of order 10^6 A/m^2. The electric current induced in the medium $\boldsymbol{J}_B$ produces Joule heat and it's interaction with magnetic field results in Lorentz force:

$$Q = \frac{\boldsymbol{J}_B^2}{\sigma} \tag{2.14}$$

$$\boldsymbol{F}_{EM} = \boldsymbol{J}_B \times \boldsymbol{B}, \tag{2.15}$$

The 2.15 is usually the main driving force of the conducting liquid motion and also can be the force which is responsible for the deformation of the liquid domain. Considering 2.4 the 2.15 can be rewritten as:

$$\boldsymbol{F}_{EM} = \frac{1}{\mu_0}(\boldsymbol{B}\nabla)\boldsymbol{B} - \nabla\left(\frac{\boldsymbol{B}^2}{2\mu_0}\right) \tag{2.16}$$

The terms on the right hand side are the rotational (driving) and pressure (deforming) parts of the Lorentz force correspondingly. The Lorentz force actually is oscillating with double frequency of the external electromagnetic field, but for the problems of induction stirring the time-average value can be taken if the frequency of the external field $f > 5$ Hz (10; 11).
The free surface deformation under the second term of the 2.16 can be calculated with help of following equation (12):

$$\rho g z + \gamma K + \frac{\boldsymbol{B}^2}{2\mu_0} = const, \tag{2.17}$$

where first term on the left side represents hydrostatic pressure and $K = 1/R_1 + 1/R_2$ is equal to the curvature of the free surface.

The magnetic Reynolds number, which is defined as

$$\mathrm{Re_m} = \mu_0 \sigma \mathrm{vL}, \tag{2.18}$$

has usually value $\mathrm{Re_m} < 1$ in typical induction applications, therefore magnetic field distribution in the melt has mainly diffusive character. This allows us to neglect the fluid motion in electromagnetic calulcations.
When the system is axis-symmetric (what is common for induction crucible furnaces), the equation 2.12 can be solved with numerical methods in 2D cylindrical coordinates. The task is simplified since vector $\boldsymbol{A}$ has only one component - tangential, while $A_z = A_r = 0$ and the $\nabla\Phi$ is zero:

$$\mu\sigma\frac{\partial A_\theta}{\partial t} = \frac{1}{r}\frac{\partial}{\partial r}(r\frac{\partial A_\theta}{\partial r}) + \frac{\partial^2 A_\theta}{\partial z^2} - \frac{A_\theta}{r^2} \tag{2.19}$$

The field values then are derived from 2.8:

$$B_z = \frac{1}{r}\frac{\partial(rA_\theta)}{\partial r} \tag{2.20}$$

$$B_r = -\frac{\partial A_\theta}{\partial z} \tag{2.21}$$

Also using 2.5 and 2.10:

$$J_\theta = -\sigma\frac{\partial A_\theta}{\partial t} \tag{2.22}$$

Finally, the non-zero Lorentz force components:

$$F_z = -J_\theta B_r \tag{2.23}$$

$$F_r = -J_\theta B_z \tag{2.24}$$

In case of harmonic analysis the solution variable A_θ can be written $= A_r cos(\omega t) - A_i sin(\omega t)$. This is suitable for the description of quasi-stationary harmonic field, when real (A_r) and imaginary (A_i) parts contain information about measurable field at $t = 0$ and $\omega t = -\pi/2\omega$, respectively. Then we can write a system of two equations for these time values:

$$-\mu\sigma\omega A_i = \frac{1}{r}\frac{\partial}{\partial r}(r\frac{\partial A_r}{\partial r}) + \frac{\partial^2 A_r}{\partial z^2} - \frac{A_r}{r^2} \tag{2.25}$$

$$\mu\sigma\omega A_r = \frac{1}{r}\frac{\partial}{\partial r}(r\frac{\partial A_i}{\partial r}) + \frac{\partial^2 A_i}{\partial z^2} - \frac{A_i}{r^2} \tag{2.26}$$

After applying boundary conditions $A_r = A_i = 0$ as $r, z \to \infty, r = 0$ and $A_i = J_I/\sigma\omega, A_r = 0$ in inductor area and solving this system 2.26 and 2.26 with finite difference or finite element method we can obtain the vector potential distributon at the orthogonal time moments.
The time-average magnitude of the Lorentz force and Joule heat can be obtained from the results of the complex analysis as

$$F = \frac{1}{2}(J_r B_r + J_i B_i) \tag{2.27}$$

$$Q = \frac{J_r^2 + J_i^2}{2\sigma} \tag{2.28}$$

These values appear then in the hydrodynamic and energy equations as source terms.

2.2 Fluid flow features and actual turbulence models

The fluid flow problem is defined by the laws of conservation of mass, momentum, and energy. These laws are expressed in terms of partial differential equations.

Here they are in the form for an incompressible fluid with constant viscosity:

$$\begin{aligned} \text{div } \boldsymbol{v} &= 0 && (2.29)\\ \rho\frac{\partial \boldsymbol{v}}{\partial t} + \rho(\boldsymbol{v}\nabla)\boldsymbol{v} &= -\nabla p + \mu\Delta\boldsymbol{v} + \rho\boldsymbol{g} + \boldsymbol{F}_{EM} && (2.30)\\ \frac{\partial q}{\partial t} + \text{div}(\boldsymbol{v}q) &= \lambda\Delta T + Q && (2.31) \end{aligned}$$

where $\vec{\mathbf{g}}$ - acceleration due to gravity, μ - dynamic viscosity, and λ - thermal conductivity. The two last terms on the right hand side represent the forces, which are responsible for the movement of the fluid. The density usually depends on the temperature as $\rho = \rho_0(1 - \beta(T - T_0))$, where β is the thermal expansion coefficient and T_0 some reference temperature. This particularly is true, when the temperature deviation is small. Then, considering that $\rho_0\vec{\mathbf{g}}$ is constant in the whole domain the corresponding term in 2.30 becomes $-\rho_0\vec{\mathbf{g}}\beta(T - T_0)$. This is called buoyancy force.

The relation between the electromagnetic and buoyancy forces shows what kind of convection is dominating. In the absence of the external forces important parameter is the dimensionless Grashof number, which illustrates the ratio between buoyancy and viscous forces:

$$\text{Gr} = \frac{\rho_0 g\beta(T - T_0)L^3}{\mu} \tag{2.32}$$

It has the order of magnitude about $1 \cdot 10^4$ in typical induction applications, which is much lower than than critical value of 10^8, when the natural convection becomes turbulent. The dimensionless Reynolds number is introduced to estimate the ratio of inertial and viscous forces:

$$\text{Re} = \frac{vL\rho}{\mu} \tag{2.33}$$

If inertial effects are great enough comparing to viscous effects, it means that the value of Reynolds number is above 2000-3000, the flow is assumed to be turbulent. Turbulence means that the velocity is fluctuating at every point of the flow field. In this case, the instantaneous velocity can be expressed in terms of a mean value and a fluctuating component:

$$v_x = \overline{v}_x + v'_x, \tag{2.34}$$

where $\overline{v}_x$ is the mean component of velocity in x-direction, and v'_x - fluctuating component of velocity in x-direction. If this expression is used for the instantaneous velocity in the Navier-Stokes equations, the equations may be then time averaged, but the time average of the fluctuating component is zero:

$$\frac{1}{\delta_t}\int_0^{\delta_t} v'_x dt = 0$$

where δ_t is a time interval long enough for this expression to be true and short enough so that transient effects do not affect this integration. After the substitution of equation (2.34) into the momentum equations (2.30), the time averaging leads to additional terms like this:

$$\sigma_x^R = -\frac{\partial}{\partial x}(\overline{\rho v'_x v'_x}) - \frac{\partial}{\partial y}(\overline{\rho v'_x v'_y}) - \frac{\partial}{\partial z}(\overline{\rho v'_x v'_z}) \tag{2.35}$$

where σ^R - Reynolds stress term.
These terms are assumed to be equivalent of a viscous stress term with an unknown coefficient, for example:

$$-\overline{\rho v'_x v'_y} = \mu_t \frac{\partial v_x}{\partial y}$$

This approach to turbulence modeling allows to combine the diffusion terms in the original equation (2.30) if the effective viscosity is defined as the sum of laminar and turbulent viscosities:

$$\mu_{ef} = \mu + \mu_t \tag{2.36}$$

The solution of the turbulence problem provides an estimation of the turbulent viscosity for Navier-Stokes equation.

There are developed several ways to model turbulent flow. The simplest case is to set constant turbulent viscosity, which is much larger than the molecular viscosity (25).

More advanced is the k-ϵ turbulence model which is the most widespread in engineering applications and it has many modifications adapted for various flow conditions (31). In the standard k-ϵ turbulence model the turbulent viscosity is calculated with help of the following expression:

$$\mu_t = C_\mu \rho \frac{k^2}{\epsilon} \tag{2.37}$$

where k - turbulent kinetic energy,

ϵ - turbulent kinetic energy dissipation rate,

$C_\mu = 0.09$

There are two differential transport equations for k and ϵ:

$$\rho\frac{\partial k}{\partial t} + \mathrm{div}(\rho \boldsymbol{v} k) = \nabla\Big(\frac{\mu_t}{\sigma_k}\nabla k\Big) + G - \rho\epsilon \tag{2.38}$$

$$\rho\frac{\partial \epsilon}{\partial t} + \mathrm{div}(\rho \boldsymbol{v} \epsilon) = \nabla\Big(\frac{\mu_t}{\sigma_\epsilon}\nabla \epsilon\Big) + C_{1\epsilon}\frac{\epsilon}{k}G - C_{2\epsilon}\rho\frac{\epsilon^2}{k} \tag{2.39}$$

The three terms in the right side of equations are, correspondingly, the diffusion, generation and dissipation terms, where G is responsible for the production of kinetic energy of the turbulence:

$$G = \mu_t\Big(\frac{\partial v_i}{\partial x_j} + \frac{\partial v_j}{\partial x_i}\Big)\frac{\partial v_i}{\partial x_j}, \tag{2.40}$$

and here are the semi-empirical coefficients that are used in these equations:

$$C_{1\epsilon} = 1.44,\ C_{2\epsilon} = 1.92,\ \sigma_k = 1.0,\ \sigma_\epsilon = 1.3$$

The solution of these turbulence equations allows to calculate the effective viscosity and the effective thermal conductivity:

$$\mu_{ef} = \mu + C_\mu\rho\frac{k^2}{\epsilon} \tag{2.41}$$

$$\lambda_{ef} = \lambda + \frac{\mu_t c_p}{\sigma_t} \tag{2.42}$$

where c_p is specific heat, but σ_t is a turbulent Prandtl number. The dimensionless Prandtl number shows the ratio of impulse and heat dissipation. In laminar flows its value is calculated with following expression:

$$\mathrm{Pr} = \frac{\mu c_p}{\lambda} \tag{2.43}$$

The turbulent Prandtl number used in (2.42) has constant value which varies in the standard model from 0.7 up to 1.0 depending on numerical realization.
There are developed several modifications of this basic model, which usually differs in either the C_μ term or in the source term of the dissipation equation.

One of them is RNG model (38), where the expression for turbulent viscosity (2.37) is replaced with differential equation:

$$d\Big(\frac{\rho^2 k}{\sqrt{\epsilon\mu}}\Big) = 1.72\frac{\hat{\nu}}{\sqrt{\hat{\nu}^3 - 1 + C_\nu}}d\hat{\nu} \tag{2.44}$$

where $\hat{\nu} = \mu_{ef}/\mu$ and $C_\nu \approx 100$. In the case of high Reynolds number this equation gives the same result as (2.37). The RNG model also provides an option to account for the effects of rotation in the mean flow by modifying the turbulent viscosity in the following form:

$$\mu_t = \mu_{t0} f(\alpha_s, \Omega, \frac{k}{\epsilon}),$$

where μ_{t0} is the value of turbulent viscosity calculated from the (2.44), but Ω and α_s are the characteristic swirl numbers evaluated according to the particular numerical realization.

These and several other features make the RNG model more accurate and reliable for a wider class of flows than the standard k-ϵ model. That's why there was an attempt to use it in modeling of the melt flow in induction furnaces, when standard model and some of its modifications failed to produce correct results.
Another widespread two-equation turbulence model is k-ω turbulence model (32), which is based on transport equations for the turbulence kinetic energy k and the specific dissipation rate ω, which is analogous to the ratio of ϵ to k. These equations are similar to those of k-ϵ model. The coefficient α^* is introduced, which damps the turbulent viscosity causing a low-Reynolds-number correction:

$$\alpha^* = \alpha^*_\infty \left(\frac{\alpha^*_0 + \mathrm{Re}_t/R_k}{1 + \mathrm{Re}_t/R_k}\right) \tag{2.45}$$

where

$$\mathrm{Re}_t = \frac{\rho k}{\mu\omega},\ R_k = 6,\ \alpha^*_0 = \frac{\beta_i}{3},\ \beta_i = 0.072. \tag{2.46}$$

In the case of high-Reynolds-number flow α^* becomes 1.
The combination of k-ω model in the inner part boundary layer and k-ϵ model in the outer part is called shear-stress transport (SST) k-ω model. The latter one also includes modified turbulent viscosity formulation to account for the transport effects of the principal turbulent shear stress. Other modifications include the

addition of a cross-diffusion term in the ω equation and a blending function to ensure that the model equations behave appropriately in both the near-wall and far-field zones.

All these two-equations turbulence models belong to one class, which is based on RANS approach, and, therefore, have some common advantages and disadvantages when applied in the field of induction furnaces. Their positive side are the good prediction of the flow pattern even on relatively coarse meshes and short time required for achieving steady-state solution. On the other side, because of Reynolds time-averaged equations, they all include assumptions about isotropy of the turbulence and stability of the flow (at least when boundary conditions are time-constant). Our experience shows, that these two latter statements are not always applicable, particularly in the case of rotating flows which are formed in induction furnaces.

2.2.1 Large Eddy Simulation

Large eddy simulation (LES) is actually one of the most promising approaches for the simulation of complex turbulent flows (1). The main idea is that only small turbulent eddies are modeled, usually their size is less than grid resolution; but large flow formations are resolved directly (Fig. 2.2). This is based on consideration, that only large scales are dependent on the flow conditions like domain geometry and external forces, but the small scales tend to be more universal and isotropic.

Considering the same incompressible viscous fluid driven by electromagnetic forces $\vec{\mathbf{f}}$ we can write again Navier-Stokes equation:

$$\rho\frac{\partial \boldsymbol{v}}{\partial t} + \rho(\boldsymbol{v}\nabla)\boldsymbol{v} = -\nabla p + \mu\Delta\boldsymbol{v} + \boldsymbol{F} \tag{2.47}$$

$$\nabla\boldsymbol{v} = 0 \tag{2.48}$$

LES models compute spatial averages of the velocity and pressure with help of a space filter in order to separate the directly resolved large scale motion from the modeled small scales. For example, here are three most commonly used filters (δ represents averaging radius):

- Top hat or box:

$$g_\delta(\boldsymbol{x}) = \{ \begin{array}{ll} \frac{1}{\delta} & \text{if } \| \boldsymbol{x} \| \leq \delta/2 \\ 0 & \text{if } \| \boldsymbol{x} \| > \delta/2 \end{array} ; \tag{2.49}$$

- Gaussian:

$$g_\delta(\boldsymbol{x}) = \Big(\frac{\gamma}{\pi}\Big)^{\frac{3}{2}} \cdot \frac{1}{\delta^3} \cdot \exp\Big(-\gamma \frac{\| \boldsymbol{x} \|^2}{\delta^2} \Big), \text{ where } \gamma > 0 \text{ (often } \gamma = 6); \tag{2.50}$$

- Spectral or sharp cutoff:

$$g_\delta(\boldsymbol{x}) = \frac{\sin(k_c \| \boldsymbol{x} \|)}{k_c \| \boldsymbol{x} \|}, \text{ where } k_c = \pi/\delta. \tag{2.51}$$

The spatial averaging operator is defined by convolution:

$$\overline{\mathbf{v}}(x,t) = \int_{\mathbb{R}^d} g_\delta(x - x') \mathbf{v}(x',t) dx'. \tag{2.52}$$

Applying this operator to the Navier-Stokes equations gives the set of space-filtered Navier-Stokes equations:

$$\rho \frac{\partial \overline{\mathbf{v}}}{\partial t} + \rho \nabla \cdot (\overline{\mathbf{v}}\overline{\mathbf{v}}) = -\nabla \overline{p} + \mu \Delta \overline{\mathbf{v}} + \boldsymbol{f} \tag{2.53}$$

$$\nabla \overline{\mathbf{v}} = 0 \tag{2.54}$$

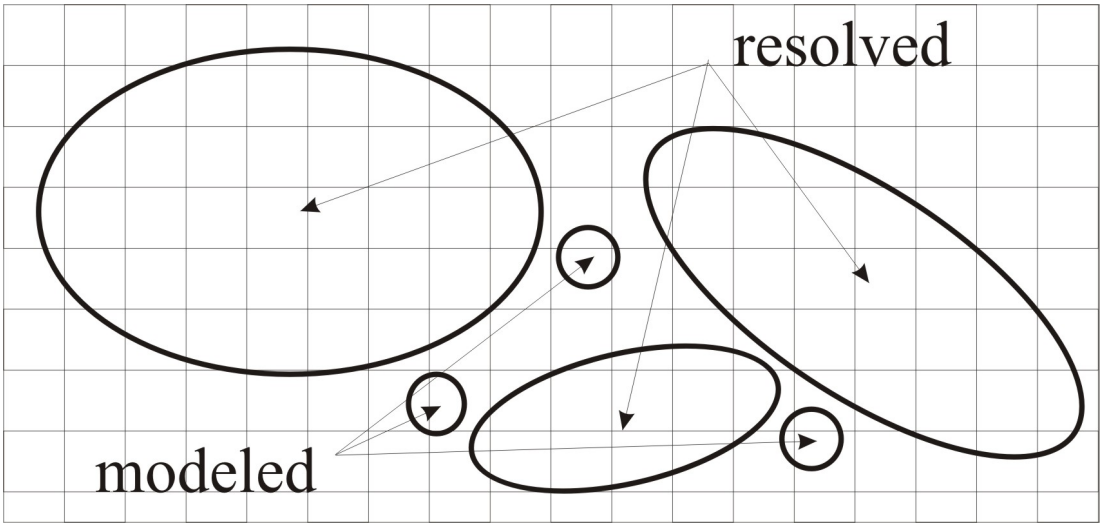

Figure 2.2: Schematic view of the different flow scales

However, this approach doesn't eliminate the closure problem connected with unknown stress tensor $\overline{\mathbf{vv}} \neq \overline{\mathbf{v}} \cdot \overline{\mathbf{v}}$, like it was in case of Reynolds averaged equations. Therefore, usually perform the decomposition $\mathbf{v} = \overline{\mathbf{v}} + \mathbf{v}'$ of the nonlinear term:

$$\overline{\mathbf{vv}} = \overline{(\overline{\mathbf{v}} + \mathbf{v}')(\overline{\mathbf{v}} + \mathbf{v}')} = \overline{\overline{\mathbf{v}} \cdot \overline{\mathbf{v}}} + \overline{\overline{\mathbf{v}}\mathbf{v}'} + \overline{\mathbf{v}'\overline{\mathbf{v}}} + \overline{\mathbf{v}'\mathbf{v}'}. \tag{2.55}$$

The first term on the right side often is called 'resolved scales', second and third terms, 'cross terms', describe the interaction of large and small eddies, and last 'subgrid scale' term represents influence of the interaction of small eddies on the mean flow. The correct estimation of the subgrid scale stress $\tau_{ij} \equiv \rho\overline{v_i v_j} - \rho\overline{v}_i\overline{v}_j$ is the aim of subgrid turbulence models. Most of them take following equation as the base:

$$\tau_{ij} - \frac{1}{3}\tau_{kk}\delta_{ij} = -2\mu_t\overline{S}_{ij} \tag{2.56}$$

where μ_t is subgrid viscosity and $\overline{S}_{ij}$ is the rate-of-strain tensor for the resolved scale:

$$\overline{S}_{ij} \equiv \frac{1}{2}\left(\frac{\partial\overline{v}_i}{\partial x_j} + \frac{\partial\overline{v}_j}{\partial x_i}\right) \tag{2.57}$$

One of subgrid viscosity models is popular Smagorinsky model (13), which is well known for its simplicity and good stability:

$$\mu_t = \rho L_s^2 \left|\overline{S}\right| \tag{2.58}$$

where $\left|\overline{S}\right| \equiv \sqrt{2\overline{S}_{ij}\overline{S}_{ij}}$ and L_s is the mixing length for subgrid scales:

$$L_s = \min\left(\kappa d, C_s\delta\right) \tag{2.59}$$

where C_s is a constant with order of magnitude 10^{-1}, k - Karman constant (usually is taken as 0.4) and d is the distance to the closest wall.
The subgrid turbulent viscosity is analogous to the turbulent viscosity of RANS modeling approaches. The main difference is that now all dependent variables are spatially filtered, but not time-averaged as they are in case of Reynolds averaged modeling. Like in k-ϵ , the subgrid turbulence in LES is assumed to be isotropic. But, it is less erroneous accordingly to the turbulent motion, which scale is smaller than the computational cell size.

LES model was initially developed for atmospheric calculations, where precise description of boundary conditions does not play significant role. As result, the near-wall flows was not the strongest side of LES since model's creation. It is believed, that local mesh refining close to the solid boundaries improves the agreement with observations. Such hope arises from the one of the main subgrid modeling properties, which states, that with increasing of the grid's spatial resolution the results converge to those of direct numerical simulation (DNS). Another expectation is, that decrease of computational cells' sizes would also decrease the subgrid transport comparing to the molecular one. But, it turns out, that significant mesh refinement does not eliminate the influence of small scale eddies on the large scale fluid motion (16). Additional functions are often supplemented in order to damp the subgrid scale transport in the regions, where mesh is fine enough (e.g. near walls) and flow can be reasonably well resolved directly. Sometimes the same damping effect is reached with dynamic subgrid models, e.g. introducing a damping constant by the Smagorinsky constant C_s. For example, the Van Driest damping function modifies the mixing length in following way:

$$L_s = C_s\delta(1 - exp(-y^+/A^+)), \tag{2.60}$$

where y^+ is non-dimensional distance to the wall and A^+ is a Van Driest constant. In another, so called, 'K-closure' approach the eddy diffusivity is related to the subgrid kinetic energy (14). The dissipation rate, which enters into energy transport equation, is calculated taking into account the distance from the solid boundary. This approach limits the growth of subgrid eddy viscosity in the near-wall regions.

Like for two-equation RANS models there is also the RNG modification for the subgrid viscosity modeling (39). The expression of the effective viscosity $\mu_{eff} = \mu + \mu_t$ becomes:

$$\mu_{\text{eff}} = \mu\left[1 + H(x)\right]^{1/3} \tag{2.61}$$

$H(x)$ is a Heaviside function:

$$H(x) = \begin{cases} x, & x > 0 \\ 0, & x \leq 0 \end{cases} \tag{2.62}$$

where

$$x = \frac{\mu_s^2 \mu_{\text{eff}}}{\mu^3} - C, \tag{2.63}$$

$$\mu_s = (C_{\text{rng}} V^{1/3})^2 \sqrt{2\overline{S}_{ij}\overline{S}_{ij}}. \tag{2.64}$$

The constants are estimated as $C_{\text{rng}} = 0.157$ and $C = 100$. The μ_{eff} tends to the value of Smagorinsky model in the highly turbulent regions and to the molecular viscosity in transitional flows and near-wall region.
Another modern approach is the Detached Eddy Simulation (DES) (33), which applies one- or two-equation RANS turbulence model inside the near wall region and LES outside.

2.3 Energy balance in turbulent flows

The energy equation for the single-phase flow has the following form:

$$\frac{\partial}{\partial t}(\rho E) + \nabla \cdot (\boldsymbol{v}(\rho E + p)) = \nabla \cdot \left(\lambda_{\text{eff}} \nabla T + (\overline{\overline{\tau}}_{\text{eff}} \cdot \boldsymbol{v})\right) + Q, \tag{2.65}$$

where

$$E = h - \frac{p}{\rho} + \frac{v^2}{2} \tag{2.66}$$

and λ_{eff} is the effective conductivity ($\lambda + \lambda_t$ - material and turbulent thermal conductivities). The enthalpy h in incompressible flow is

$$h = \int_{T_{\text{ref}}}^{T} c_p \, dT + \frac{p}{\rho} \tag{2.67}$$

The latter term Q in (2.65) is the density of external heat sources, which in our case will be the Joule heat (2.14).
Turbulent motion of the fluid greatly increases energy transfer in the direction normal to the streamlines. Correct estimation of this contribution is vital for the final results of the temperature distribution. The estimation of it's quantitative value is closely correlated with the estimation of the turbulence intensity - main task of any turbulence model. The effective thermal conductivity λ_{eff} as was shown in (2.42) directly depends on turbulent viscosity and turbulent Prandtl

number Pr_t in case of k-ϵ turbulence model. While the turbulent viscosity distribution is the product of turbulence modeling, the Pr_t is a user-defined constant. The widely used value of it vary between 0.7 and 1. There is an analytical expressions for estimating turbulent Prandtl number, which involve eddy diffusivities for momentum transfer ε_M and heat transfer ε_H:

$$\mathrm{Pr_t} = \frac{\varepsilon_\mathrm{M}}{\varepsilon_\mathrm{H}}. \tag{2.68}$$

These momentums are defined basing on eddy diffusivity concept:

$$\overline{u'v'} = -\varepsilon_M\left(\frac{\partial u}{\partial y}\right), \tag{2.69}$$

$$\overline{T'v'} = -\varepsilon_H\left(\frac{\partial T}{\partial y}\right). \tag{2.70}$$

Considering, that usually turbulent viscosity is several times higher than molecular one, the value of this dimensionless number has important influence on resulting effective thermal conductivity and, therefore, on heat transfer and temperature distribution predicted by k-ϵ turbulence model. However, it is thought, that in three-dimensional or/and recirculating flows the concept of eddy diffusivity looses it's usefulness, therefore restricting the application of turbulent Prandtl number to the two-dimensional boundary layers (17). But even there it's meaning is significantly reduced when liquid metals become the subject of modeling. The relatively high molecular thermal conductivity of metals makes the influence of Pr_t choice negligible and it can be taken as unity.

The LES implements the same approach for modeling of effective thermal conductivity, but the advantage is that the sub-grid viscosity, which replaces the turbulent viscosity, is much smaller and, hence, the value of Pr_t has less influence on modeling results. Additionally, due to the transient modeling approach the main contribution to the heat exchange is resolved directly as convective energy transfer. The finer becomes the mesh, the less remains the part of the heat conduction by molecular viscosity and subgrid turbulence.

The same rules apply for the transport of the scalar quantities in the flow, such as alloy additieves, if we consider them fine enough, that they do not influence the flow pattern and move along streamlines (inertia of the particles is sufficiently small).

3 Specifics of melt flow and heat transfer in crucible induction furnace

3.1 Crucible induction furnaces

The typical crucible induction furnace (CIF) is built of two cylindrical cylindrical vessel where the one with larger diameter is placed on the top of the smaller one (Fig. 3.1). The bottom part (also called inductor-crucible or inductor) is surrounded by the inductor coil which has several turns. Such geometry allows to operate with significantly bigger melt volumes without increasing the diameter of the inductor. It is used either as a melting furnace, as a holding furnace or as a casting furnace. This furnace is operated by electrical power in the range from the default electric network frequency up to several hundreds of Hertz. It depends on the requirements for the efficient heating and stirring for most metals. The main desired feature of these furnaces is the keeping melt in the upper vessel at the temperature high enough for casting and simultaneously preventing the melt overheating in the lower (inductor) part in order to extend the operational time. Therefore, the sufficient heat transfer between these two parts is very important. Main parameters which influence the temperature homogenization are:

- the geometry of the interface between the inductor and the bath (flange area): the larger the opening the better is heat exchange, but also the mechanical construction becomes more complex.
- the intensity of the electromagnetic stirring in the inductor: higher stirring should pump more hot melt into the bath, but also it erodes the ceramic lining in the inductor, therefore decreasing the operational life.

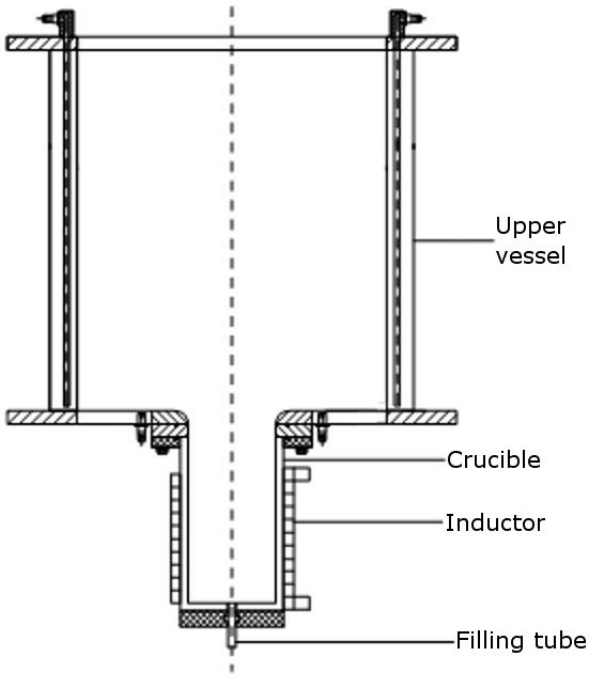

Figure 3.1: Sketch of the crucible inductor furnace (CIF).

- heat losses through the bath walls and from the free surface of the melt: this depends on the materials used for isolation and wall thickness, which again should be in balance with mechanical constraints. The heat flux from/to the surface could be either radiation (the higher temperature - the higher losses) or process specific.

Considering high assembling and operational costs for such kind of devices the numerical modeling is an important assistance for the successful development and operation of the crucible induction furnaces.

3.1.1 Overview of the research on induction furnaces

The former experimental and numerical studies of this class of induction furnaces have been mainly concentrated on the simple geometry with only one cylindrical volume - inductor crucible furnace (ICF), whch will be main topic of the next

chapter of the present work. These measurements of the velocities and turbulence of the electromagnetically stirred flow have been performed with various methods. Between them are: optical, when the surface photographs are taken under stroboscopic lighting (18) or when the laser Doppler anemometry is used in molten salts (46); thermal, when the thermal wake behind a hot-film probe is tracked (19; 27; 63), electrical, when the potential induced by the melt flow is measured with the permanent magnet probe (20; 29) and ultrasonic, when Doppler velocimetry method is used (21). These measurments deliver the information that the flow is not stable with developed turbulence. However, none of them could provide the visualization of the instantaneous flow pattern at different times, because the velocities were measured either at one point, on the surface or along the line profile. Therefore, the only global picture of the flow that could be obtained with existing measurement methods is the time-averaged velocity distribution.

First modelling attempts had analytical character due to the obvious reasons (22; 23; 24). These mathemathical formulations allowed to investigate and predict the main energetical correlations between the external current strength and frequency and the resulting melt motion and thermal regime.

The numerical modeling of the electromagnetically forced flow in the cylindrical volumes has been performed since several decades, but mainly oriented on achieving the time-averaged velocity distribution. Initially these calculations were based on the finite difference methods (25; 26; 43) and already provided good agreement with the experiment. The definition of the turbulent viscosity was often chosen accordingly to the problem conditions and represented either a constant value throughout of the computational domain or a simple function of the coordinates. Such approaches innevitably assume that the flow has homogenous turbulence distribution, which can be probably true only in the low-frequency electromagnetic fields. The development of the turbulence modeling, e.g. appearance of the k-ϵ model, allowed to perform the numerical studies of more general character, when the wide range of operational conditions and geometries could be modeled with the same set of model contstants (27; 28). The obtained velocity profiles had very good coincidence with the measured ones. Also the turbluent quantities and their distribution were compared with the oscillations observed in the laboratory

installations, but they usually gave only reasonable agreement. The extensions of the turbulence models, developed for the particular set-ups, could provide better results in terms of heat and mass transfer accordingly to the experimental observations (49). Also it was reported that the $k-\omega$ model appears to be more precise than k-ϵ model in case of recirculated and separated flows (29; 30).
Usually, since the development of the first analytical models, the hydrodynamic and electromagnetic calculations were uncoupled from each other, i.e. it was assumed that the flow does not influence the electromagnetic field. Therefore, it was possible to calculate the Lorentz forces and Joule heat only once and use them as source terms for fluid flow modeling. However, in some cases such coupling was necessary, especially when the deformation of the free melt surface became the object of the interest for the transient simulation (44; 45).
More advanced computations were performed during the last decade reflecting the increased computational capabilities. They were based on the unsteady RANS with Reynolds-Stress (7) turbulence model and Large Eddy Simulation (8; 10). One common and important advantages of these models is the possibility to model the anisotropy of the turbulence, which is actual for the modeling of the recirculated flows. However, the payment for this is the need for transient three-dimensional calculations and, hence, the increased time requirements.

3.2 Experimental results

The series of measurements were performed in the Institute of Electrotechnology (former Institute of Electroheat) Leibniz University of Hanover at the millennium break. They determined the velocity pattern in model CIF and, also the temperature distribution for the set of operational parameters including external current strength and frequency. Additionaly the influence of the furnace tilt angle was studied.
Due to the inapplicability of the industrial melts, like steel, for the experimental investigations, these measurements were performed with Wood's metal. It is an fusible alloy which consists of 50% Bismuth, 25% Lead, 12,5% Tin and 12,5% Cadmium. Due to it's high electrical conductivity and low viscosity it is widely used as a prototype melt for MHD experiments (2; 3; 4; 5). The main physical

Table 3.1: Physical properties of Wood's metal and steel

	Wood-Metal	Steel
Density, $[10^3\ kg/m^3]$	9.4 $(85°C)$	6.8 $(1700°C)$
Melting temperature, $[°C]$	74	1500
Electrical conductivity, $[10^6\ 1/m\Omega]$	1 $(80°C)$	0.72 $(1535°C)$
Dynamic viscosity, $[10^{-3}\ Ns/m^2]$	4.2 $(85°C)$	1.2 $(1600°C)$
Thermal conductivity, $[W/mK]$	18.8 $(85°C)$	33 $(1600°C)$
Specific heat, $[Ws/kgK]$	168 $(85°C)$	775 $(1500°C)$

properties in comparison with those of typical steel are provided in the Table 3.1. As it can be seen, the main advantage of this alloy is it's low melting temperature of about 74°C. The operational range from 80 up to 150°C allows using simplified measurement devices and carrying out prolonged measurements. The characteristic numbers of the Wood's metal flow in model furnace and steel flow in industrial-sized installation are provided in the Table 3.2.
Relatively low operating temperature gives the possibility to use measurement devices with permanent magnet sensors. The Vives probe (10) was used in this case. This sensor is based the Faraday's law: the electromotive force is induced when conductive medium moves through the magnetic field:

$$\vec{\mathbf{E}} = -(\vec{\mathbf{v}} \times \vec{\mathbf{B}}) \tag{3.1}$$

It consists of permanent magnet and four electrodes (Fig. 3.2). Melt flowing between the electrodes creates the potential difference, which can be measured and converted to velocity values using calibration curve. Hence, two perpendicular components of the velocity can be determined simultaneously. Also, this velocity measurement method has relatively low time-constant and, therefore, allows to recognize velocity pulsations, which exist in turbulent flows. The maximum frequency of detectable oscillations depends on the signal/noise ratio, and, due

Table 3.2: Characteristic numbers for model and industrial furnaces

	Wood-Metal	Steel
Crucible radius, [m]	0.085	0.53
Characteristic velocity, [m/s]	0.35	1
Reynolds number	6.7×10^4	3×10^6
Prandtl number	0.038	0.028
Magnetic Reynolds number	0.037	0.48

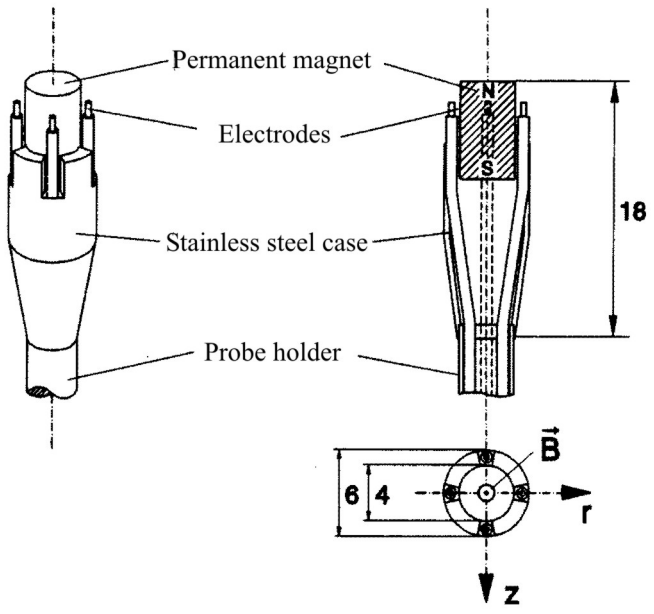

Figure 3.2: Sketch of the measurement probe.

to the relatively low voltage read from the electrodes ($1 - 20\ \mu$V), it was limited to about 20 Hz. One minute long measurement is typically required to obtain reliable time-average of the velocity magnitude in the given point.
The calibration of such sensors usually is performed in rotating channel. With known flow velocity values and corresponding voltage measured on electrodes one can derive the coefficient of the proportionality, which in our case was of order $5\ \frac{m}{mV \cdot s}$. It should be mentioned, that due to the finite dimensions of the sensor itself and extremely low signal's voltage, reliable velocity measurements start from about 5 cm/s (Fig. 3.2).
The Figure 3.4 shows the geometry of the model furnace as well as measured time-average velocity distribution. The 10-turn coil is located around the bottom part

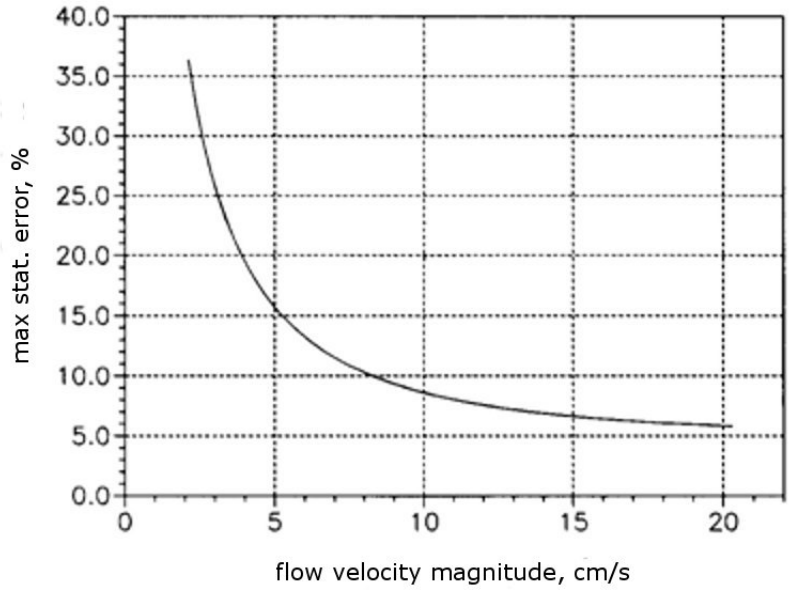

Figure 3.3: Relative deviation in velocity measurements depending on velocity magnitude (35).

of the crucible. There can be seen that flow is highly intensive in that region and almost insignificant in the bath area. The two toroidal vortices located in the inductor and driven by the electromagnetic field influence are typical for such kind of installations. However, analysis of transient measurement data revealed

that there are quite intensive velocity oscillations all over the inductor volume. Especially pronounced these oscillations are for the axial component of the velocity in the zone between the main vortices of the averaged flow (Fig. 3.5). This is the zone where the time-average axial velocity itself tends to zero $\overline{v_z} \to 0$, but it's oscillating part has maximal value across the whole crucible $\overline{v'^2} \to \boldsymbol{max}$. The amplitude of the oscillations is about 30 cm/s and this value is in the same order of magnitude as the maximum time-averaged velocity (measured on the axis), so the influence of this phenomenon on the heat and mass exchange processes has to be taken into account. Auto-correlation analysis shows that the long-time period in this case is about 3.5 seconds. We can imagine that the heat transfer is realized by the melt moving between the lower and upper region. The melt from the lower region flows into the upper region to be cooled down there, then the melt moves back to be heated up again. The temperatures inside the melt were measured with the NiCr-Ni thermocouple. These measurements are necessary in order to determine the dependency of the temperature distribution on total operational power and frequency. It is possible in this way to estimate the maximal inductor power, which is safe to apply without overheating of the melt. This experience can be later interpolated to the industrial-sized furnaces. Taking into account the relatively short response time of the thermocouple ($\approx$ 140 ms) it was also possible to record temperature oscillations.

Measured temperature distribution is displayed on the Fig. 3.6 together with main energetic in- and outflow. The thermal boundary conditions included the water-cooling of the side wall of the bath and natural convection from the melt surface. Due to the low temperature the radiation losses are of order several watts and, therefore, can be neglected. The measurements show that the thermal field in the inductor is very well homogenized by the intensive electro-magnetic stirring. At the same time, the isotherms in the bath reflect the dominance of the conductive heat transfer over the convective, because of the small flow velocities of the melt.

Combining the results of both velocity and temperature measurements it becomes possible to calculate approximately the amount of heat, which can be transferred by the low-frequency oscillations mechanism. It can be estimated by the melt movement through the virtual border between eddies in a unit of time. If we

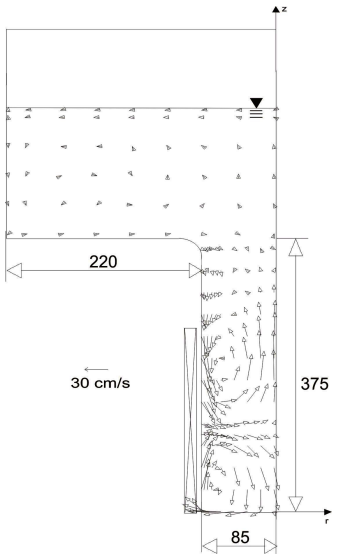

Figure 3.4: Dimensions of the experimental crucible induction furnace (axis-symmetric) and measured time-averaged velocity distribution (f = 482 Hz, I = 1908 A).

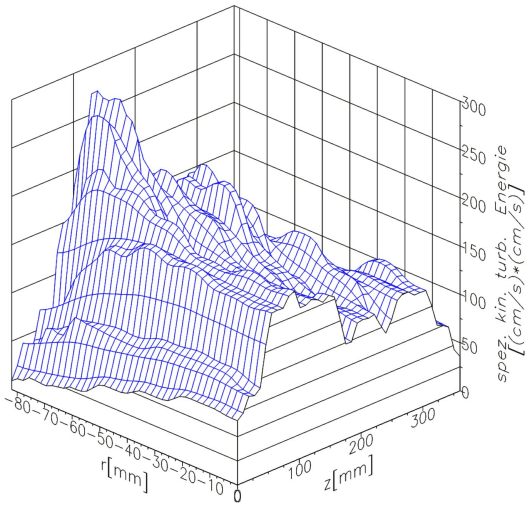

Figure 3.5: Distribution of the specific kinetic energy of the oscillations in the inductor volume obtained form the measurement data (f = 482 Hz, I = 1908 A).

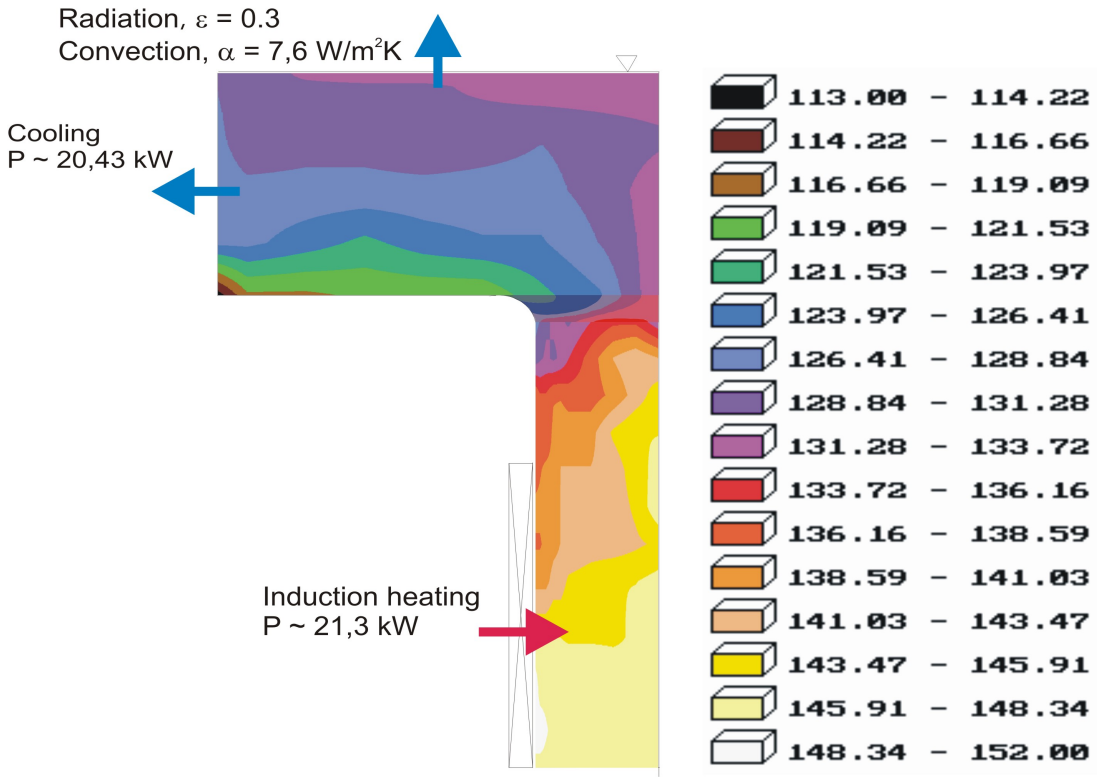

Figure 3.6: Temperature distribution measured in the experimental crucible induction furnace (axis-symmetric).

suggest that the heat brought in this way to the upper vertex region efficiently dissipates in the colder flow due to the intensive turbulence, then the heat flux Φ throug the cross-section S can be described by the moving mass of the fluid, the average temperature difference δT between the lower and upper region and the specific heat c_p:

$$\Phi = \frac{c_p m \delta T}{t} S$$

The mass flow can be calculated considering the intensity of the axial velocity oscillations, which changes in radial direction, where near the symmetry axis the oscillations are significant smaller. The result of this estimation is a total heat flux of about 9,5 kW between the lower and upper flow eddy. This estimation is in good agreement with the numerically calculated and experimentally measured induced power in the lower eddy of about 10 kW. Taken into account, that heat losses through the crucible wall are insignificant the described transfer mechanism plays the main role in heat exchange processes between the averaged flow regions. An effective thermal conductivity can be derived from the calculated heat flux and temperature gradient:

$$\lambda_{eff} = \frac{\delta \Phi}{\delta S} \times \frac{\delta z}{\delta T}$$

The effective thermal conductivity can be described by the sum of the turbulent conductivity λ_t, the molecular conductivity λ and the conductivity provided by low-frequency oscillations λ_{lf}:

$$\lambda_{eff} = \lambda + \lambda_t + \lambda_{lf}$$

It is noticeable, that λ_{lf} is of order 10^3 which is significantly higher than the molecular conductivity of the melt material.

3.3 Application of k-ϵ model

The melt flow in induction furnaces was many times simulated numerically with the help of the $k - \epsilon$ and similar two-parameter turbulence models, which are widely used for various engineering applications. These calculations usually produce good results for the averaged velocities, but as it will be shown below, that the calculated temperature distribution can be different from the experimental

results, especially when flows have rotational structure.
The numerical mesh for 2D calculations consisted of 10^5 elements, 35500 of them in the inductor. This corresponds to the average spacing of 1 mm with total volume of 0.08 m^3. The mesh was refined at the inductor wall two times with coefficient 1.5, so the width of the first element became 1/4 mm. This is considered to be enough to capture Lorentz force gradients at the wall and also to model correctly the boundary flow. All solid boundaries were defined with standard no-slip velocity condition, only the free surface on the top of the bath was set with zero shear stress. The thermal boundary conditions were adjusted to the experimental with the convection scheme accordingly to the cooling water temperature. The effective convection coefficient was estimated from measured heat losses. The convergence of the thermal solution was additionally checked with total heat balance between the energy generated by Joule heat sources and integral heat flux through the domain walls.
The Fig. 3.7 (left) shows velocity distribution calculated with 2D steady-state standard k-ϵ model. The pattern of the simulated flow coincides with the measured in the model furnace (Fig. 3.4)very well. Two intensive toroidal vortices are located in the inductor and slow melt motion in the bath as it was observed in the experiment. The comparison of the velocity profiles on the symmetry axis ($r = 0$), Fig. 3.8 show that the lower vortex is modeled quite good in terms of time-average size and velocity values. The agreement between the calculated and measured velocities in the upper vortex is not so good. Here can be seen that the Renormalization group (RNG) modification of the k-ϵ models performs better, however the dimensions of the upper vortex are overestimated. Also the velocities on the axis in the bath are predicted more precise than in case of the standard model.
The temperature distribution predicted with the 2D k-ϵ model (Fig. 3.7 right) significantly differs from the measured one (Fig. 3.6). The pattern already looks different and we can see sharp temperature gradient between the vortices, which does not exist in the plot of experimental data. The temperature value changes rapidly in the axial direction at the half height of the inductor - where the maximum of the external Lorentz forces is located. If we compare the temperature profiles (Fig. 3.9 and 3.10) taken on the symmetry axis and at the half-radius

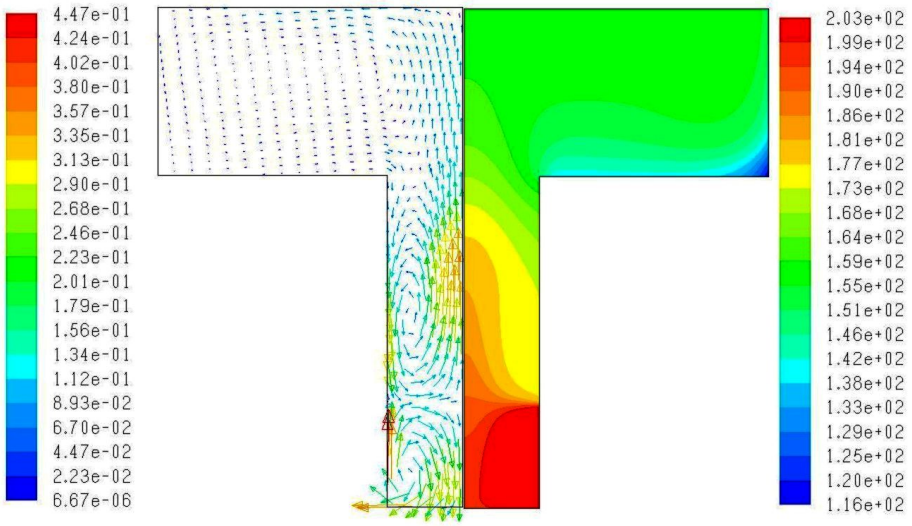

Figure 3.7: Velocity [m/s] and temperature [^{o}C] distribution calculated with the standard k-ϵ turbulence model.

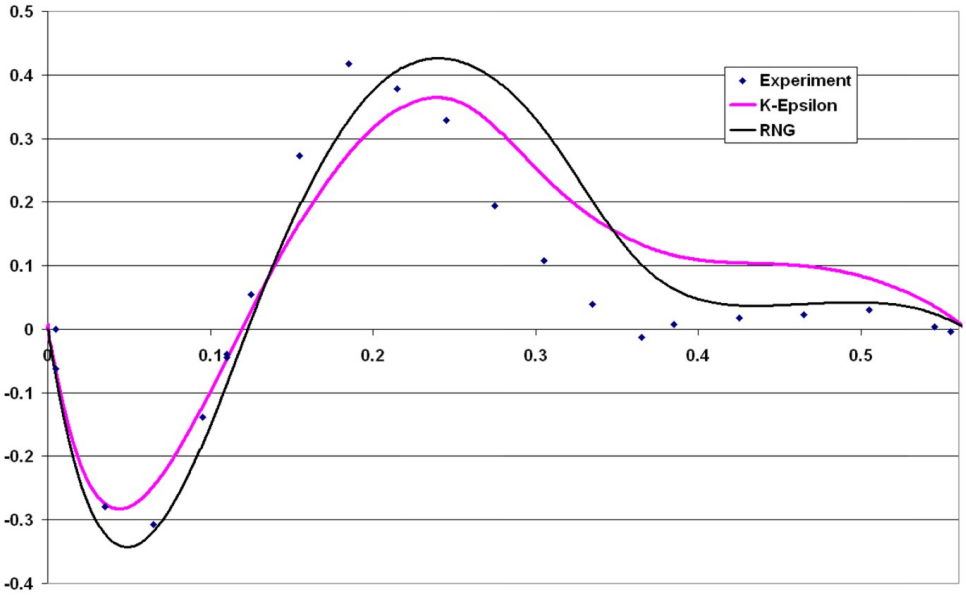

Figure 3.8: Comparison of the velocity profiles [m/s] measured and calculated with the standard and RNG k-ϵ models.

distance from the wall make it clear that heat transfer from one vortex of the averaged flow to another is not modeled correctly as it is happening in the real furnace. It is shown that there are almost no temperature difference along the symmetry axis in the inductor and a slight decay in the axial direction at the half-radius position. The RANS models, however, predict from 10 to 15^{o}C and from 15 to 20^{o}C temperature step correspondingly. The results of the RNG model have less steep temperature curve comparing to the standard k-ϵ model, but it is nevertheless in worse agreement with experiment as the velocity profile discussed above. The difference between the overall level of the temperatures appears because of the adjustment of the heat transfer coefficient at the bath side-wall (where the maximum heat losses take place) to the experimental data. Therefore we have comparable temperatures at that boundary but extremely high temperature values in the inductor due to the under-predicted heat exchange efficiency. Obviously it is because of lack of the transport mechanism which would provide energy transfer from one vortex to another. The convective heat exchange is insignificant because the streamlines are looped inside one vertex. The modeling of the turbulent heat transfer relies on the turbulent thermal conductivity, which directly depends on the predicted turbulence intensity values and is proportional to the turbulent viscosity (2.42). But, as it is shown on the figure with modeled turbulent kinetic energy distribution (Fig. 3.11 left), the zone between the vortices is supposed by the k-ϵ model to be less turbulent than other areas of the flow. The maximums of the turbulence kinetic energy in the centers of the vortices arise from the velocity-gradient-based generation term in the k equation (2.40) and due to the looped character of the flow produced energy does not spread throughout the whole volume. As a result the zone between the vortices, where the velocities and their gradients are rather small, lacks of the turbulent energy, which is neither produced nor brought there. Consequently (2.37), the turbulent viscosity distribution (Fig. 3.11 right) also has minimum in this area and the turbulent heat transfer does not contribute to the energy exchange between the vortices. The low-frequency oscillations, which are observed in the experiment and are thougt to be responsible for the heat and mass exchange between the vortices, could not be simulated with the two-parameter turbulence models because all flow fluctuations are modeled inside the turbulent kinetic energy term. The evaluation of this

term based on the local velocity gradients allows to take into account mainly the high frequency small scale velocity perturbations, which are isotropic and are not significantly influenced by the large flow structures. Therefore, the magnitude of the $\sqrt{\overline{v_z'^2}}$, which plays main role in the low-frequency transport mechanism between the considered rotating flow formations, is practically equal to zero in case of RANS modeling.

The question may rise, why the solution of the energy equation produces unacceptable results and at the same time the results of the momentum equation are in the good agreement with the measurement? On the first sight the delivered by the turbulence model values of the turbulent viscosity and thermal conductivity are proportional and momentum transfer should be as well erroneous as the heat exchange. The answer is that such different behavior is spotted because of the different character of the boundary conditions for these both equations. The heat losses in the bath due to the water-cooling of the side-wall make the heat flow from the lower vortex to the upper one crucial for the total temperature distribution. But the momentum boundaries are in principle analogous for the both vortices and the latter ones could be considered as two independent structures (although they are not, as it will be shown further) without making too big mistake.

Since the effective thermal conductivity $\lambda_{eff} = \lambda + c_p \mu_t / Pr_t$ (where Pr_t is the turbulent Prandtl number and μ_t is turbulent viscosity) directly depends on the turbulent viscosity, this leads to the underestimation of the heat transfer between the eddies. At the same time, the analysis of the experimental results of the ICF reveals that the maximum level of the low-frequency pulsations is located at half-height of the inductor (between the main vortices). Therefore the most intensive mixing should take place in this zone. But the $k - \epsilon$ equations are unable to describe low-frequency pulsations, which arise due to the large scale flow dynamics. Furthermore, the discussed $k - \epsilon$ model is based on the hypothesis of isotropic turbulence, but experiments show, that significant anisotropy takes place not only close to the crucible walls, where axial oscillations are dominating, but also at the symmetry axis, where radial oscillations are prevalent. Relative isotropy can be observed only in the centers of large vortices. The Reynolds stress model could be applied in order to take into account local flow anisotropy, but

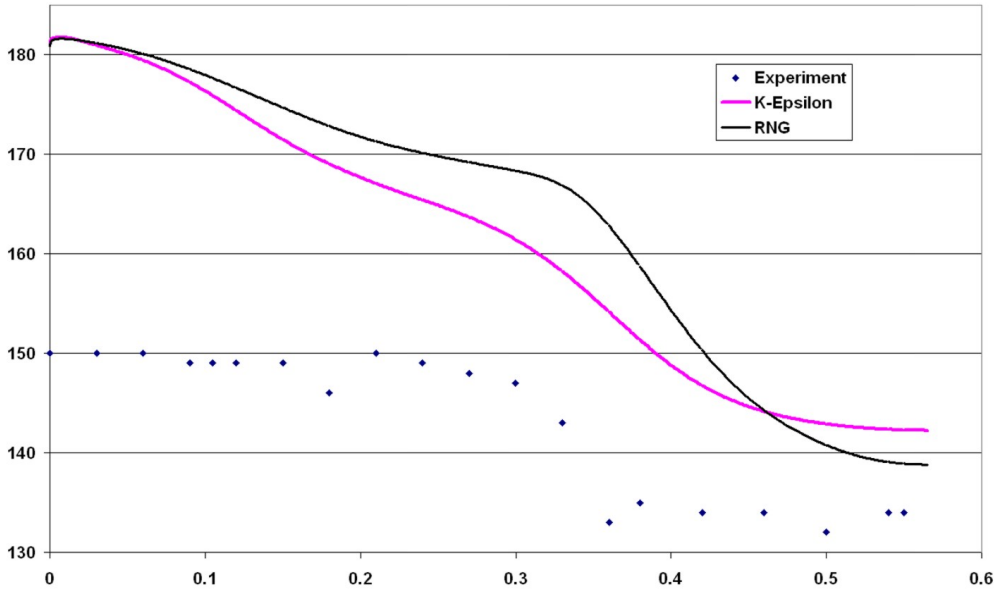

Figure 3.9: Comparison of the temperature profiles [^{o}C] along the symmetry axis measured and calculated with the standard and RNG k-ϵ models.

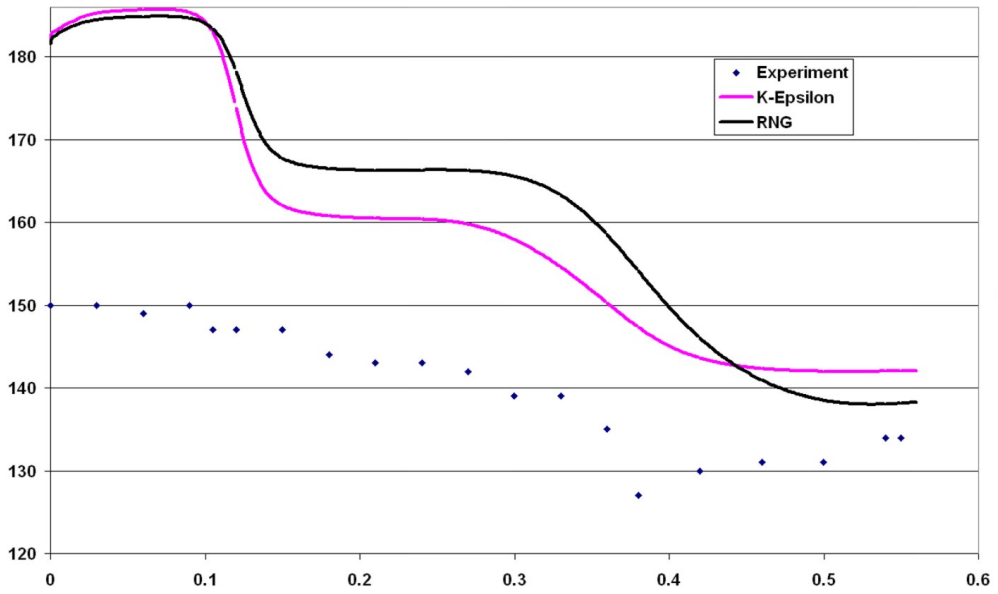

Figure 3.10: Comparison of the temperature profiles [^{o}C] at R/2 measured and calculated with the standard and RNG k-ϵ models.

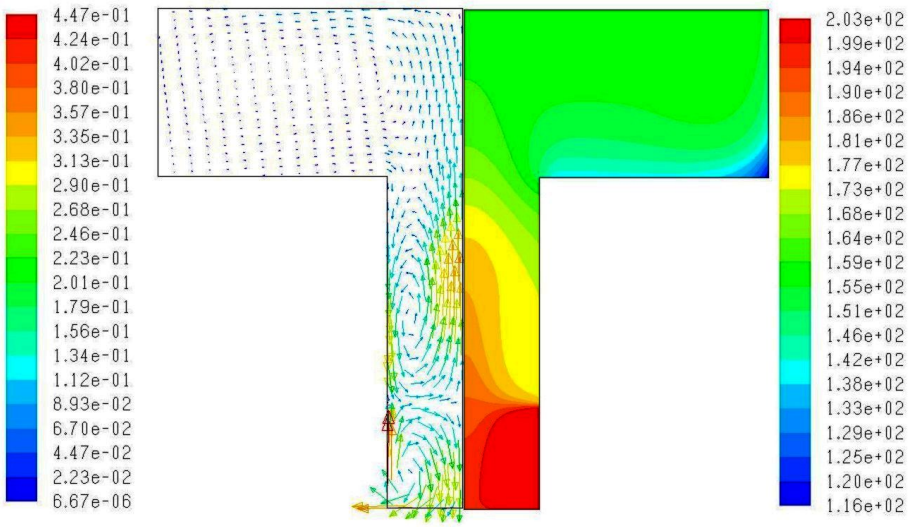

Figure 3.11: Turbulent kinetic energy (left) [m^2/s^2] and effective viscosity (right) [kg/m·s] distribution calculated with the standard k-ϵ model.

at the cost of additional equations to be solved. The unsteady modification of this approach (URANS) allows to perform transient investigations of the flow (7), however the turbulence modeling still has mainly empirical character.

3.4 Application of LES model

The main requirements of the LES modeling are the transient calculations and relatively high mesh resolution. Together it makes these method quite time-consuming. But, if we consider permanently growing computational power available to end-user, it is becoming more and more accessible for the practical applications. The mesh for the model of CIF consisted of $3.9 \cdot 10^6$ hexahedral elements, about 1/3 of them in the inductor. The mesh density was varied between regions in order to reduce the computational time. The typical size of the element edge in the inductor was about 1.8 mm and in the bath - 2.9 mm. The time-step of the transient simulation was chosen accordingly to the Courant number $\mathrm{Cr} = \mathrm{v} \cdot \delta\mathrm{t}/\delta\mathrm{x}$, which recommended value should be below 1. In the case of $\delta t = 0.005$ used in the described simulation the $\mathrm{Cr} \approx 1.05$. Another criteria is the characteristic lentgth

which corresponds to the border between the inertial and dissipation scales of turbulence. It can be estimated as $l_D = 60\eta$, where

$$\eta = \frac{L}{Re^{\frac{3}{4}}}. \tag{3.2}$$

Taking the Reynolds number $\mathrm{Re} = 5 \cdot 10^4$ and the largest scale of the flow structure $L = 0.085\ m$ we become $l_D = 1.5 \cdot 10^{-3}\ m$. Hence, the mesh in the inductor is adequate to the both conditions. The same number for the bath region is of order $l_D \approx 18\ mm$ due to the significantly slower melt motion and therefore reduced Reynolds number.

Definition of the starting conditions is another important question which appears for LES calculations due to their transient nature. The variant with the zero velocity field and uniform temperature distribution corresponds to the real situation in the experiment. But the real time required to achieve quasi-stable (with not changing time-average picture during several turnover times of the main vortices) solution may be too long because it includes prolonged transformation of the system from homogeneous fields to the operational state. Especially this relates to the temperature field, which is strongly influenced by the processes taking place in the bath. If velocities in the inductor converge relatively fast, the melt flow in the larger bath zone and with smaller velocity values needs more time to come to the established state. But this slow flow driven by the inertia and buoyancy plays important role in the energy transfer. The other mean of the heat flux here is the molecular thermal conductivity. The corresponding P*é*clet number is about 500, hence, the flow pattern can not be assumed as negligible. Therefore, the solution of the steady-state calculations with RANS model may be more preferable as a starting condition for LES simulation. The velocity distribution predicted with k-ϵ model usually is in good agreement with the measured time-average data. So, using this as initial field allows us to save significant amount of the computational time. The calculations now should last enough time to achieve the stable thermal field. This process is taking less time in this case, since the velocity pattern in the bath, which is responsible for the convective energy transfer, is already initiated. Otherwise it would take long time to simulate process of momentum transfer from electromagnetically-driven vortices in the inductor to the inertia-driven flow in

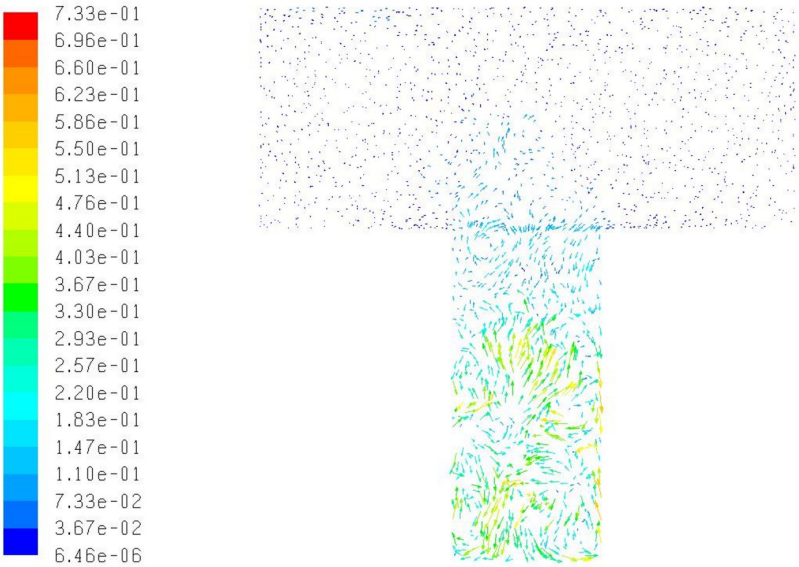

Figure 3.12: Example of intermediate velocity field [m/s] calculated with the Smagorinsky LES model.

the bath.

The time constant can be introduced, which would characterize the time required for a system to achieve the stable state. It will certainly depend on the characteristic velocity or on the turnover time of the largest vortices, since they play the main role in heat and mass distribution in the recirculated flows with large Péclet number. It can be stated that 3 or 4 turnover times are necessary to become the time-average solution for the transient flow. In our case these times are quite different for the two regions: bath and inductor. While in the inductor one vortex makes a turn in about 2 seconds, the same action in the bath takes about 30 seconds. This makes the LES calculations of the CIF very time consuming, but, due to the specific geometry of this furnace, the steady-state calculations usually are not able to provide reliable results for temperature distribution.

The Fig. 3.12 shows intermediate velocity distribution during LES calculations. The structure of the main flow vortices is not clearly outlined, but the pattern contains several smaller vortices of different size instead. Observing the movie made from consequent images it can be seen how vortices created in the inductor

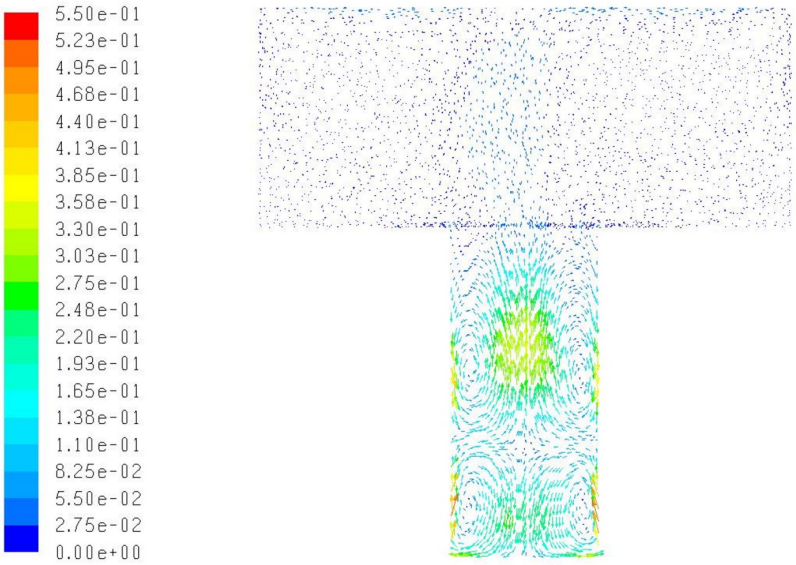

Figure 3.13: Time-averaged velocity field [m/s] calculated with the Smagorinsky LES model (total simulated time 140 seconds).

move up in to the bath, therefore initiating melt movement in there. This process transfers not only momentum, but also provides effective energy transport mechanism. Due to the spatial and temporal dimensions of these vortices, they can not be modeled with the RANS turbulence models.

However, the time-averaged velocity distribution shown on the Fig. 3.13 resembles the results of the k-ϵ simulation (Fig. 3.7). The flow pattern is symmetric with two toroidal vortices and the velocity profile on the axis follows the experimental curve (Fig. 3.14), although the values are slightly smaller than measured ones. The reason may be the three-dimensional character of the simulated flow. The examining of the results of the simulation reveal the presence of the tangential flow with magnitude about 5 cm/s. This should not exist in the completely symmetric system, and it is thought that it will decrease if the time-averaging period is prolonged. Than the magnitude of this component would append to the axial velocity value. Also, it can be noticed that LES predict the time-averaged velocities more accurately than the k-ϵ models (Fig. 3.8).

The profile from the intermediate velocity field is also shown on the Fig. 3.14.

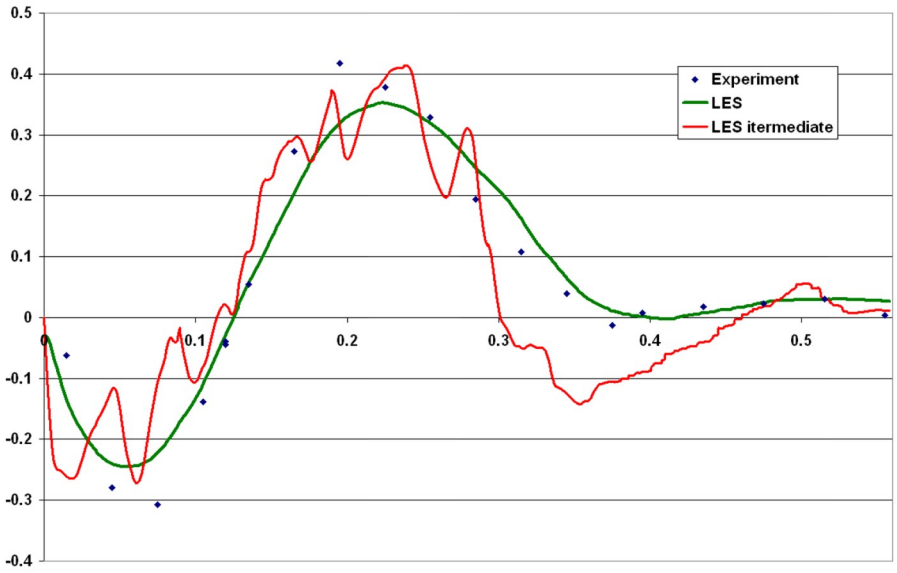

Figure 3.14: Comparison of the velocity profiles [m/s] at symmetry axis measured and calculated with the Smagorinsky LES model.

There can be seen how the two-vortex structure is perturbed by local flow oscillations. Should be noted, that while in the inductor these perturbations have size comparable to the that of the main vortices, in the bath region their dimension is significantly reduced. This demonstrates the possibilities of LES to resolve the energy transfer cascade from large scales to the small ones down to the size of the grid cell.

The Fig. 3.15 shows time-average temperature distribution calculated with the LES model. It does not have completely symmetric look because, as it was discussed above, the thermal field requires more time to achieve stable state than velocity field since starting conditions for the temperatures are further from the reality than the starting conditions for the velocities. However, the LES results agree with the measurements (Fig. 3.6) much better than RANS predictions both in terms of the temperature scale and the temperature distribution. The inductor is the hottest place with average temperature of order of 150^{o}C. Also there is a jet along the symmetry axis, which brings hot melt to the bath surface and then loops by the side wall and the bath's bottom. The symmetry in the bath is more

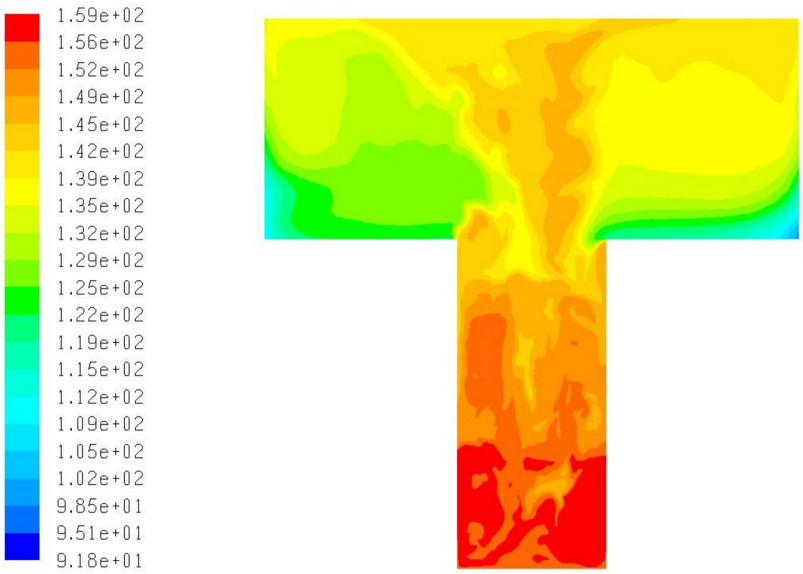

Figure 3.15: Time-averaged temperature field [^oC] calculated with the Smagorinsky LES model.

disturbed than in the inductor accordingly to the difference in the time constants for these regions.

The graph on the Fig. 3.16 shows the comparison of the temperature profiles analogous as it was presented for the k-ϵ simulation (Fig. 3.9 and 3.10). There are shown temperatures along the symmetry axis and the line located at the half-radius distance from it. Despite the slight shift of the overall level of these curves above the values from the experimental data, they show good agreement in terms of the temperature decrease rate form the inductor bottom to the bath surface. There are no more steep gradients between the vortices at the half height of the inductor. Therefore, the difference of the temperatures in the lower vortex and the melt top level is only about 10-12^{o}C, while the experiment provides the value of about 15^{o}C.

It can be concluded that application of the LES to this problem has brought significantly better results, than k-ϵ model. The reason of the improvements in the calculations of the heat transfer between the different flow structures is the transient resolving of the large to small scales of the flow oscillations. This also

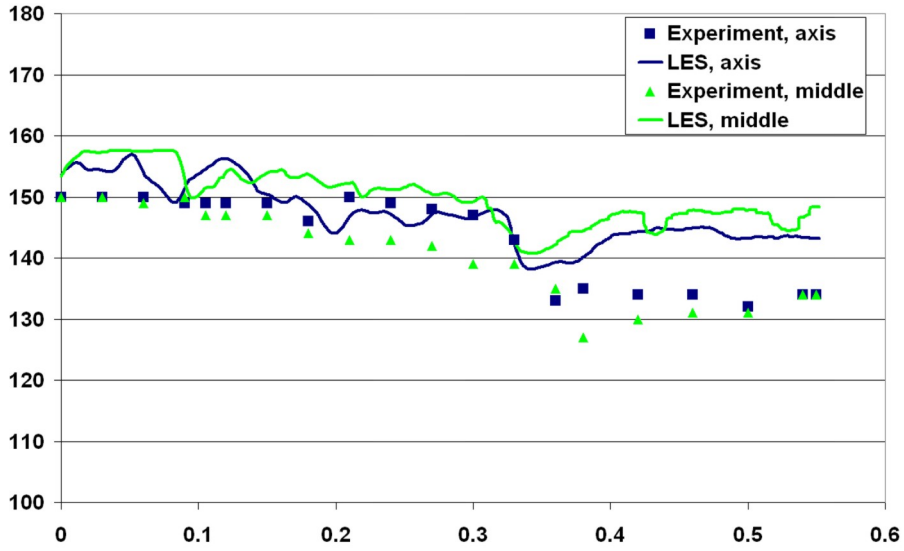

Figure 3.16: Comparison of the temperature profiles [°C] at symmetry axis and R/2 measured and calculated with the Smagorinsky LES model.

can be demonstrated on the contour plot (Fig. 3.17), which shows the distribution of the velocity's standard deviation value derived from the transient LES results. This quantity is defined with the following equation:

$$\sigma = \sqrt{\frac{1}{n}\left(\sum_{i=1}^{n} v_i^2\right) - \bar{v}}, \tag{3.3}$$

where v_i is the velocity value at the time-step i, n is the number of time-steps and $\bar{v}$ - the time-average value of the velocity magnitude. This plot can be opposed to the Fig. 3.11 (left) where the distribution of the turbulent kinetic energy is shown. Here is shown, that unlike k-ϵ results, most oscillating zone is located between the main vortices of the averaged flow, which corresponds with the measurement results shown on the Fig. 3.5.

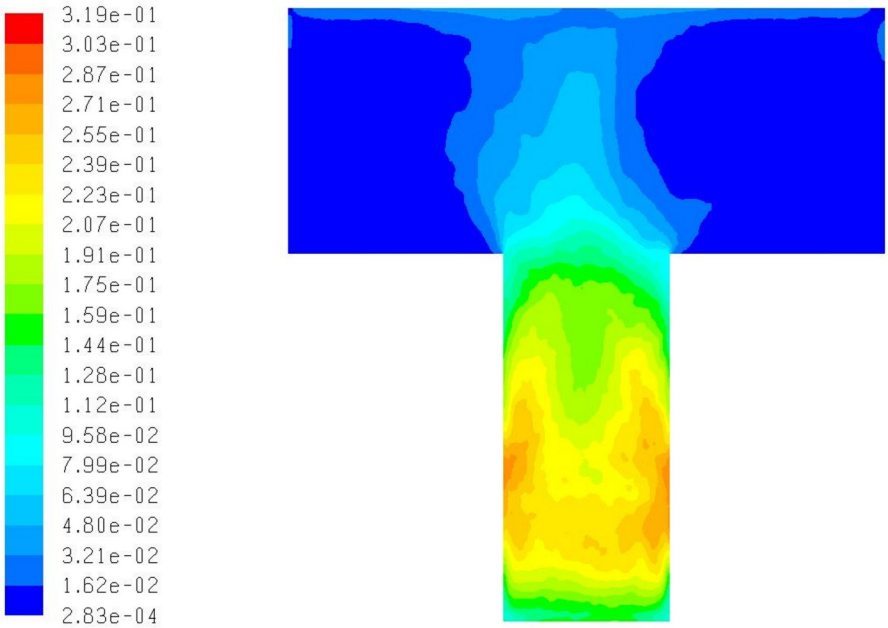

Figure 3.17: The distribution of the standard deviation values [m/s] of the velocity magnitude calculated with the Smagorinsky LES model.

4 Turbulent metal flows in induction crucible furnaces

4.1 Induction crucible furnaces

As it was mentioned before, the induction crucible furnaces (Fig. 4.1) are widely used in metallurgical industry for melting of various metals and alloys and keeping them in the liquid state for prolonged period of time. The homogeneous temperature and add-ons distribution is important for successful process operation. The absence of the vessel above (unlike the CIF) makes the situation easier for numerical modeling in terms of reduced requirements for the element count and also reduced process' time-constants, which allows shorter simulation time. Therefore, the ICF is more suitable for the parameter study task, which involve the turbulent model choice and mesh size influence on the simulation results. On the other side practically homogenous thermal boundary conditions leave almost no space for the evaluation of the heat transfer processes between the different flow structures, since the energy input and output in them does not vary too much. However the study of flow instabilities and their influence on the transport of scalar quantities can be performed without limitations.

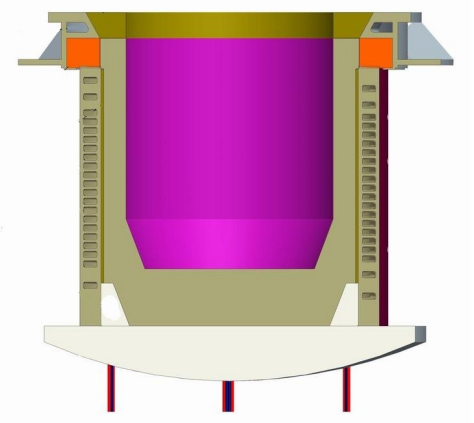

Figure 4.1: Sketch of the industrial ICF

4.2 Experimental investigations in the model induction crucible furnace

The experimental background for the numerical calculations was derived from the results of the measurements performed in the model ICF. The melt flow velocities were determined in a laboratory induction crucible furnace (Fig 4.2). The Wood's metal was used as the model melt like in the experiments with the CIF described in the previous chapter. The main parameters of this model furnace are given in the Table {tb:icfpar.

The experimental set-up chosen for the comparison with numerical modeling had the twelve-turn inductor of the ICF fed with alternating current at the frequencies around 400 Hz. The total input power from generator could go up

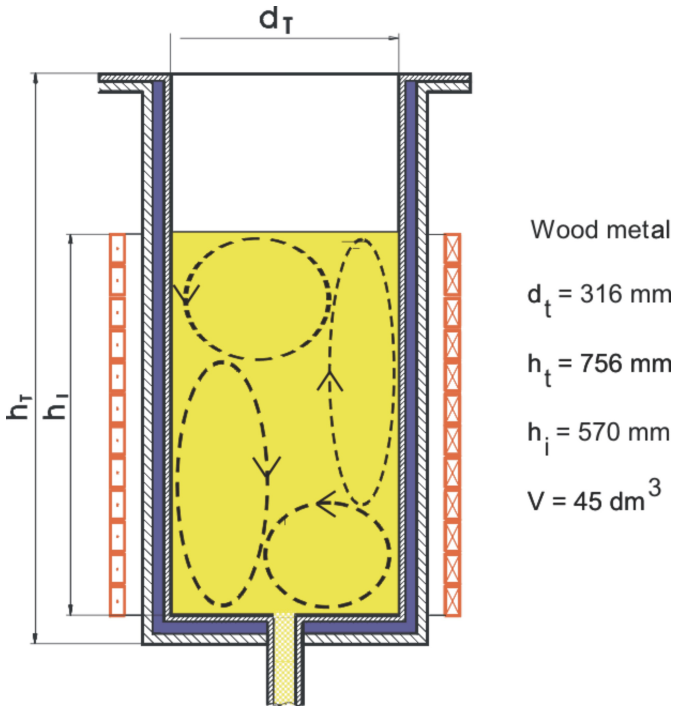

Figure 4.2: Experimental induction furnace used for 2D and 3D hydrodynamic modeling. Flow directions and vortices' shapes are schematically shown for the unstationary flow regime

Table 4.1: Main parameters of the model furnace

Radius of crucible (R)	0.158 m
Height of inductor (H_I)	0.57 m
Filling level (H/H_I)	50 - 120 %
Melting temperature (T_m)	72^o C
Melt density (ρ)	$9,700$ kg/m^3
Melt dynamic viscosity (μ)	$4.2 \cdot 10^{-3}$ kg/m $\cdot$ s
Melt elec. conductivity (σ)	$1 \cdot 10^6$ S/m

to 85 kW high with corresponding inductor current above 2 kA. Accordingly to the inductor design, the melt is subject of the Lorentz forces (2.15) and Joule heating (2.14) along the whole height of the crucible's side wall. Therefore, due to the rotational flow structure the temperature field is thought to be almost homogeneous, the thermal gradients in the melt to be negligible and the melt properties - constant. The overheating of the melt was prevented by means of the water-cooling of the crucible walls.

Potential difference velocity probe with incorporated permanent magnet (10) was used to measure simultaneously two of three velocity's components with scanning rate about 20 Hz. The sensitivity of the probe is about 2 μV per 1 cm/s of flow velocity.

The initial velocity measurments were performed in the beginning of 90's (34) with the same measurement system which was described in the previous chapter. It was for the first time observed, that intensive velocity oscillations take place in the electromagnetically driven rotational system with two large vortices of the averaged flow. These experiments were repeated later also by author of this work using more up-to-date data acquisition measurement system which is based on Top Message device from Delphin firm and portable computer Pentium III 700 MHz, connected into network TCP/IP Ethernet. The Top Message device has

a 24 bit A/D converter and provides the processing of signals from 15 analogue inputs. The high precision of the converter allowed to refuse of using DC preamplifiers and connected with this additional disturbances. The measuring system possibilities also allowed to refuse of using physical filters for suppression the alternating current disturbances and to change them for mathematical filtration of the signal. The results of these new measurments were in agreement with the original also in terms of the spatial distribution of the oscillations' intensity.
When the filling level of the furnace is about 100% (melt height H is equal with the inductor height H_I), measured mean flow pattern consists of two typical toroidal vortices, as it was expected, considering that flow is mainly driven by the Lorentz forces, which are clearly dominant over the buoyant convection. The characteristic flow velocity v_{ch} is about 15 cm/s. It should be mentioned, that the value of the velocity magnitude near the crucible wall ($r \to R$) is not suitable for the definition of the characteristic flow velocity v_{ch}, because high radial velocity gradient near the crucible wall makes the determination imprecise either numerically (grid size limitations) and experimentally (finite dimensions of the measuring probe). Thus, the maximal time-average velocity near the symmetry axis of the crucible is used for the characteristic velocity v_{ch}.
Transient velocity measurements also revealed, that melt flow is unstable and the amplitude of the oscillating velocity $v' = v - \bar{v}$ is comparable with the characteristic velocity magnitude $v'_{max} \approx v_{ch}$. Also, the presence of periodic low-frequency flow oscillations was exposed: most intensive of them are located close to the crucible wall between the main vortexes and have the characteristic time period about 8-12 seconds (Fig. 4.3, left). Pulsations with shorter period (about 1-2 seconds) can be observed as well. The oscillation intensity is decreasing when the distance from the wall is increasing, e.g. at the half radius their amplitude is only 50% of the 40 cm/s which is observed close to the crucible wall. The major oscillation frequency f increases proportionally to the time-averaged velocity: $f \sim v_{ch} \sim P$, where P is power input (Fig. 4.5). Examining experimentally derived and filtered (2 Hz$<$ f $<$9 Hz) oscillations energy, the following low-frequency oscillations were not taken into account:

- which evolution is determined by the global flow structure, i.e. rotation in the low-viscosity fluid and macroscopic vortices interaction;

Table 4.2: Measured dependance of large-scale oscillation period on operational power

Power, kW	Oscillation period, s	Oscillation frequency, Hz
50	8.5	0.118
65	6.7	0.149
87	3.9	0.256

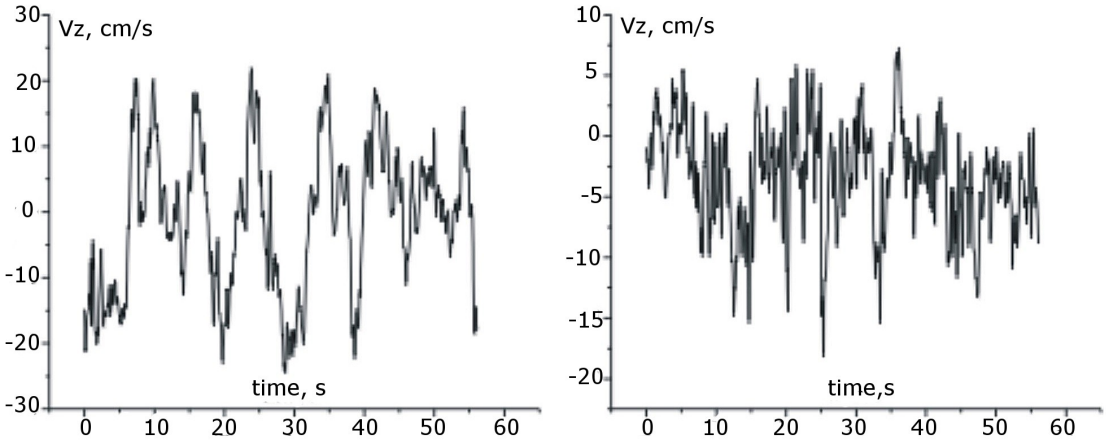

Figure 4.3: Measured axial velocity oscillations at the half-height of the inductor r=0.14m (left) and r=0.06m (right)

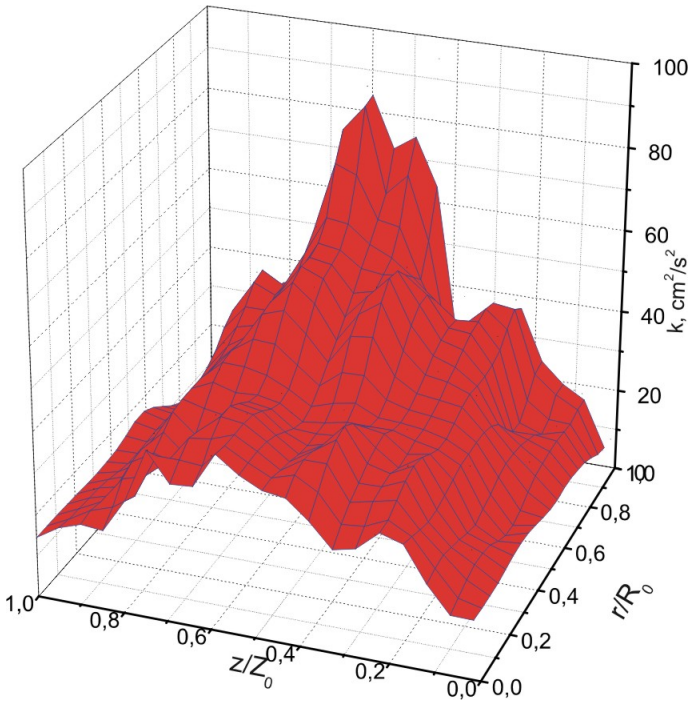

Figure 4.4: Kinetic energy of the velocity oscillations measured in model furnace

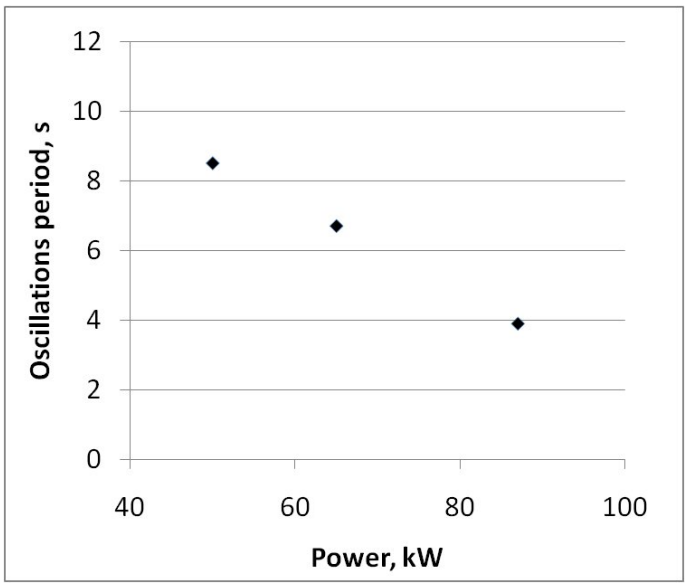

Figure 4.5: The dependency of low-frequency oscillation period on operational power

- which are significantly anisotropic and have non-homogeneous distribution across the domain - noticeable maximum of k_z is in the zone: $r \to R$ and $h = 0.5H$.

Analysis of the remaining part of the energy spectrum reveals that spectral amplitude is changing accordingly to the power function of the frequency: $E_{exp} \sim f^{-1.5}$. The EM field frequency is $f = 400$ Hz, therefore, considering the finite penetration depth, which is usually $\approx R/3$ and large fluid inertia, its direct influence on the oscillations is practically excluded. The discussed type of turbulent flows has characteristic Reynolds number $Re \approx 10^3 \div 10^5$. As a consequence, the local isotropy of the turbulence is probable and an expression of Kolmogorov spectrum $E_{teor} \sim f^{-5/3} \approx f^{-1.7}$ (37) could be applied for the inertial range of the flow, where the frequencies are high enough. Thus, experimental results, considering the limited frequency range available for analysis ($f < 9$ Hz), are in quite good agreement with the theoretical estimations. Higher frequencies were not measured because of their very low spectral intensity, e.g. at 10 Hz it was 4 times lower than at 1 Hz. Hence, limiting the measured frequency range allowed to shorten the measuring time and to reduce processed data amount.

4.3 Application of k-ϵ model

The inducton crucible furnace is well suited for the 2D modeling due to it's axis-symmetric geometry. The electromagnetic and fluid-flow analysis are performed separately under assumption that the influence of the moving melt on the external electromagnetic field is negligible. This is acceptable if we consider that the EM field penetrates only about 20 mm inside the liquid and that the velocity vectors are mainly parallel to the EM field lines in this layer.
The well-known $k - \epsilon$ model (31) was the first turbulence model applied for the numerical studies of the melt flow inside ICF. As it was mentioned before, this model has relatively low mesh requirements and is widely used and verified in various numerical engineering applications. It usually produces fast good quantitative results for the time-averaged velocity distribution in case of stationary

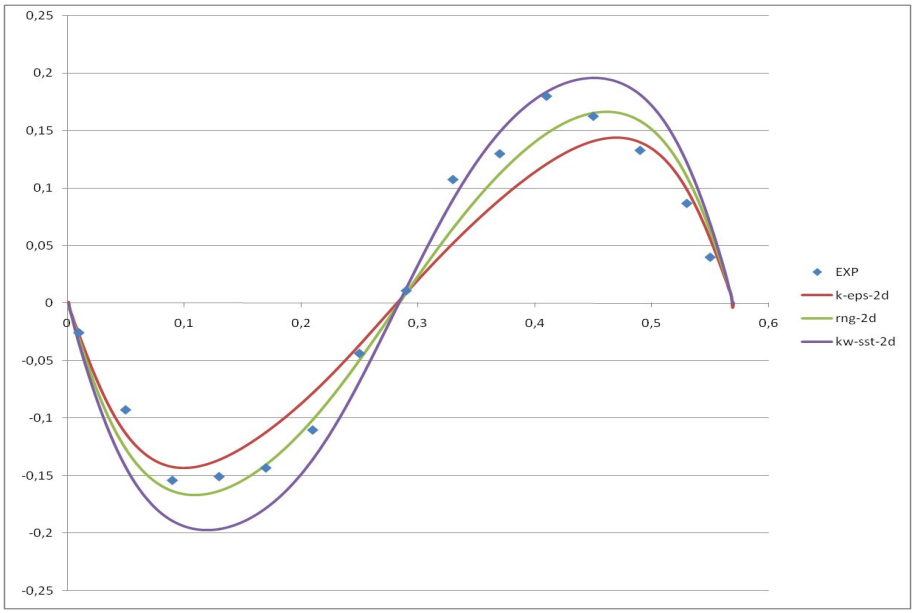

Figure 4.6: Comparison of the axial velocity profiles measured and calculated with various 2D RANS turbulence models

two-dimensional calculations. The Fig. 4.6 demonstrates that two-equation turbulence models perform their task very well when it comes to the prediction of the velocity pattern. The RNG and $k-\omega$ models are added to the standard k-ϵ model on this graph, and it can be seen that all of them have relatively good agreement with the experiment, with RNG slightly in the lead. But, the results of $k-\epsilon$-like simulation with standard set of constants predicted highest values of turbulent viscosity in the eddies centers and lowest between the eddies. Such distribution is characteristic for the $k-\epsilon$ model even in case of 3D transient simulations, as will be shown below (Fig. 4.15).

As was mentioned before, the low-frequency oscillations observed in the experiment are supposed to have three-dimensional nature and, therefore, they can not be modeled with help of 2D numerical model. Considering this, the 3D transient calculations were performed, which were based on the same standard $k-\epsilon$ turbulence model and mesh with about 230,000 tetragonal elements inside the crucible. The simulation converged to the almost stationary state with symmetric recirculated flow eddies. Considering, that the time averaging of the flow, during

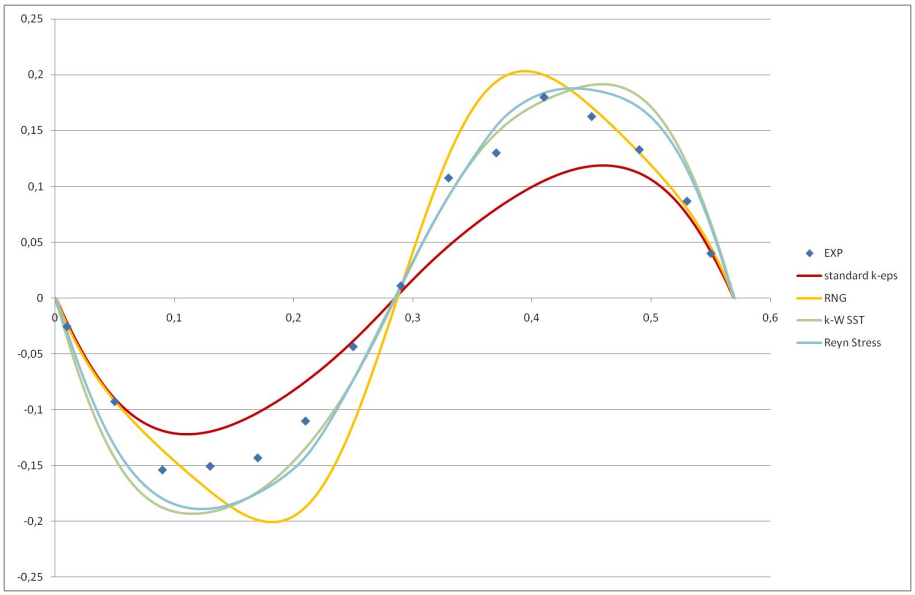

Figure 4.7: Comparison of the axial velocity profiles measured and calculated with various 3D RANS turbulence models

iterations at each time step, is able to damp flow perturbations, the time-step interval was reduced, but the flow remained stationary without oscillations. One of the reasons which may damp the oscillations, is the presence of relative high values of the turbulent viscosity (up to 10^3 times higher than molecular viscosity) in the centers of the eddies.

Following series of the calculations were performed with the mesh consisting of about $15 \cdot 10^6$ elements. These mesh resolution is suitable also for LES, therefore, the results from RANS models and LES can be directly compared. In total 3 RANS models were consequently applied for the stationary calculations. The standard k-ϵ model has shown the worst results when we compare the calculated velocity profiles with the measured ones (Fig. 4.7). The RNG model again performed significantly better than the standard k-ϵ , obviously because of the accounting for the low-Reynolds-flows. The velocity magnitude predicted with the RNG model is in good agreement with the experimental one. But the position of the velocity maximum on the crucible axis is shifted to the center. Best results have shown the $k-\omega$ and Reynolds Stress models both in terms of velocity

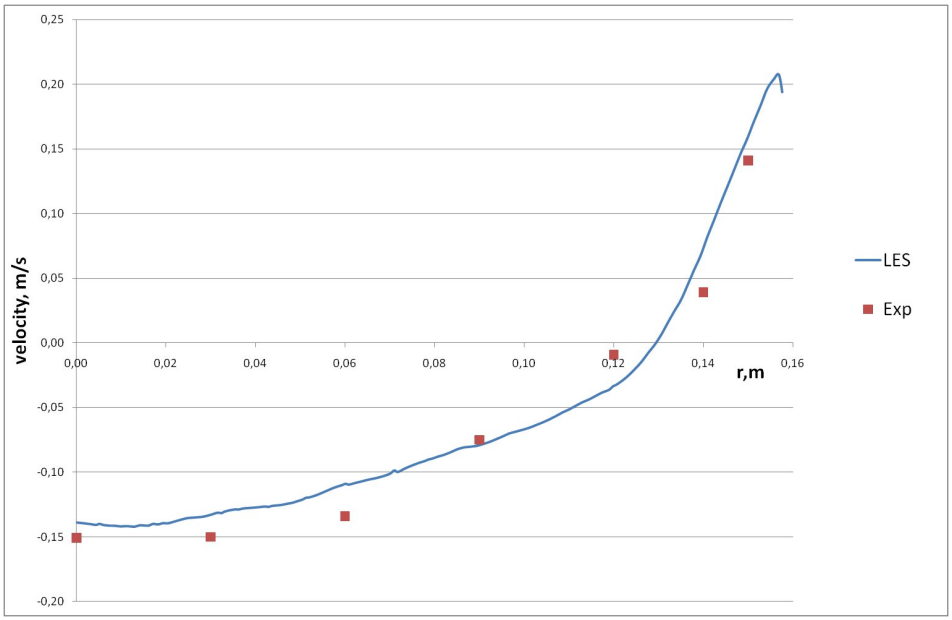

Figure 4.8: Comparison of the radial velocity profiles measured and calculated with 3D LES turbulence model

magnitude and flow pattern.

4.4 Application of LES model

The LES was performed using parallel computing with up to 32 processors distributed betweeen 5 nodes, nevertheless, the study of one parameter set (calculation of 60 seconds of the flow time) was taking several weeks depending on the time-step size. The residuals, which are flow rate weighted, converged to the $1 \cdot 10^{-3}$ at each time-step within 2-5 iterations. The central-differencing discretization scheme was used for the momentum equation and the body-force-weighted scheme was applied for pressure interpolation.

First calculations were performed on mesh with 230 thousand elements and time-step $1 \cdot 10_{-2}\ ms$, but the results were found inacceptable. Further numerical investigations with the same time-step but increased mesh resolution up to 3.5

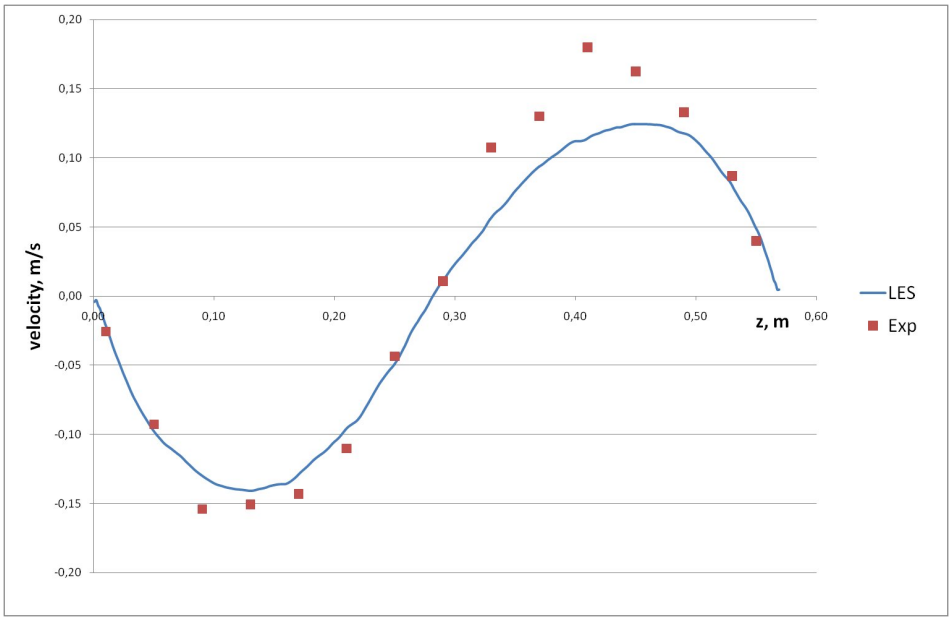

Figure 4.9: Comparison of the axial velocity profiles measured and calculated with 3D LES turbulence model

millions elements revealed flow instabilities similar to those observed in the experimental induction crucible furnace. It was simulated about 2 minutes in total. In order to investigate the reliability of these results, the mesh was refined again to 15 millions elements and the 45 seconds were simulated with the time-step of $1 \cdot 10_{-3}\ ms$. The time-averaged velocity profiles from the latter simulation are shown on the Fig. 4.8 and 4.9. They demonstrate good agreement with the experimental data even for such time interval for averaging.

Examining numerical results, it was found out that axial velocity component oscillates with the amplitude of approximately 15 cm/s near the crucible wall in the region of vortexes interaction (Fig. 4.13), but at the half-radius of the crucible these oscillations are approximately two times less intensive. The main oscillations, which have period about 10 seconds, are combined with less intensive high frequency ones, like in the experiment. The amplitude of these oscillations remains the same for different mesh resolution levels and time-step values, also the computational time grows together with number of elements and number of time-steps. It is also noted, that initial simulation conditions are not so impor-

Table 4.3: Calculated and measured characteristic properties of low-frequency oscillations

Grid elem., 10^6	Sub-grid turb. scheme	$0.5\overline{v^2_{l,max}}, cm^2/s^2$	Oscill. period, s
0.4	S-L	44	14
3.5	S-L	50	12
3.5	RNG	30	10.5
15	S-L	50	12
Exp. data	-	65	9

tant, because if we start LES with zero velocity field, then in the beginning flow pattern becomes symmetric and at this state resembles results of steady-state calculations. Since we are not interested in every detail of the flow, but mainly in the global parameters, such as dynamics of the large structures and intensity of the velocity oscillations, the choice of initial flow conditions is not the decisive factor.

The Table 4.3 includes together with Smagorinksy-Lilly scheme also results of the Renormalization group (RNG) sub-grid viscosity model for Large Eddy Simulation (39), which introduces low-Reynolds-number effects mainly in the region near the wall. Both sub-grid viscosity schemes produced qualitatively similar results, but RNG predicted lower intensity of velocity oscillations, while results of Smagorinsky-Lilly were very close to the measured values, especially when finer mesh resolution was used.

The transient calculations show that after starting the flow intensity is growing driven by the electromagnetic forces and the axial-symmetric flow is formed. Together with the velocities grows the Reynolds number, therefore, the main toroidal vortexes become unstable with three dimensional large-scale oscillations with characteristic spectral properties, which depend on geometry of the domain. Comparing the graphs with the Fourier analysis of the experimental and numerical data (Fig. 4.10), one can see that the calculated results include not only the main frequency, but they also show several additional pulsations with higher and lower frequencies. The presented graph shows that the spectrum of the numeri-

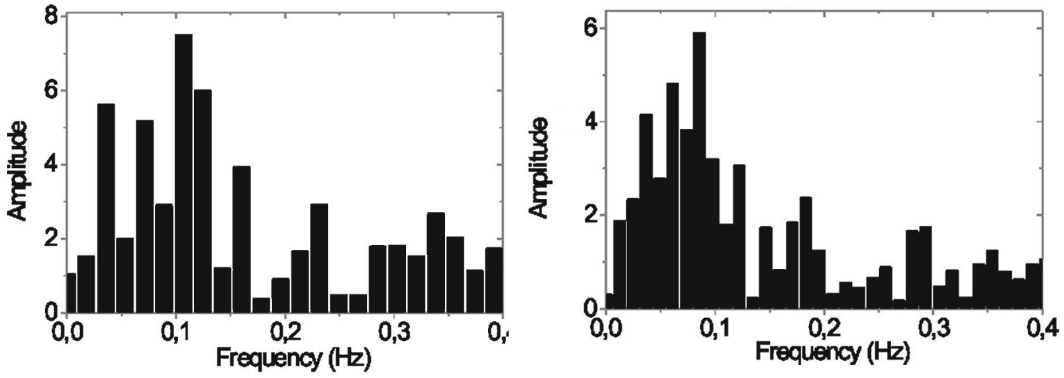

Figure 4.10: Fourier analysis of measured (left) and simulated (right) oscillations in the region between the main vortices

cal results is shifted in the direction of the lower frequencies in comparison with the experimental data. This tendency remains when spatial grid resolution is decreased. Unfortunately, further experiments with mesh refinement are confronted with too high consumption of calculation time and computational resources.

The experiments in the model induction crucible furnace show, that if the characteristic flow velocity is about $v_{ch} \approx 0.15$ m/s, the maximum amplitude of large scale oscillations $v_{l,max}$ has the same order of magnitude ($v_{ch} \sim \mid v_{l,max} \mid$). The maximum value of the specific kinetic energy of these oscillations (in the zone near the crucible wall, between the main flow vortices) has a value of $k_{max}^{exp} \approx 65$ cm^2/s^2 (Fig. 4.11). LES calculations have confirmed these results and also agreed with the experiment in terms of:

- time-averaged flow pattern, symmetry and intensity;
- the period of the prevalent oscillations $T \approx 10$ s;
- maximal specific kinetic energy of oscillations - $k_{max}^{num} \approx 50$ cm^2/s^2.

Several numerical movies based on transient calculations were produced with different crucible cross-sections in order to visualize the three-dimensional flow development during numerical simulation. One of them shows contours of the velocity magnitude on the melt surface. Videos which were taken above the melt

surface of an industrial ICF melting processes show periodic regions with relatively high flow intensity, which move around the central point. It is clearly noticeable that the numerical movie based on transient calculation has common details with the video movie of the industrial furnace.
The transient eddies dynamics can be examined on the animated sequence with vertical cross-section of the crucible. It becomes clear, that the melt flow looses any symmetry in phase of fully developed oscillations. At the beginning, when the simulation starts from the zero flow field, the symmetrical flow pattern is formed. Futher, after less than one vortices' turn-over time, the main vortices of the mean flow start to deform and finally break up into smaller ones, which move between different regions and provide in this way intensive heat and mass exchange in the entire melt (e.g. Fig. 4.12). This process is also visible on the graph with the axial velocity dependance on time $v_z(t)$ in the two points between the main vortices (Fig. 4.13). The initial period when axial velocity component is close to zero (as it should be in these points in case of symmetrical flow pattern) ends after about 5 seconds from the start of the simulation. The oscillations grow in amplitude and have achieved their full strength already at 18 seconds mark. The period of the large scale oscillations can be roughly derived from the same graph and compared with experimental results (Fig. 4.3). When the measured and calculated velocity oscillations are put together on the same graph (Fig. 4.14) one can notice that they have much in common, also experimentally derived curve show less details for high-frequency fluctuations because of the lower sampling rate.

The Fig. 4.15 shows the turbulent viscosity (for k-ϵ model) and sub-grid viscosity (for LES model) distribution. As it can be seen, the character of the distribution as well as the absolute values are very different between these turbulence modeling approaches. The sub-grid viscosity is not only at least one order of the magnitude lower then the turbulent viscosity of k-ϵ model, but also has the tendency to decrease with the cell size. This allows us to assume, that simulation results will become more indepedent from such semi-empirical parameter as turbulent viscosity when the mesh resolution is increased.

The transient LES simulation aslo provide the possibility to calculate and visualize the distribution of the separate components of the low-frequency velocity

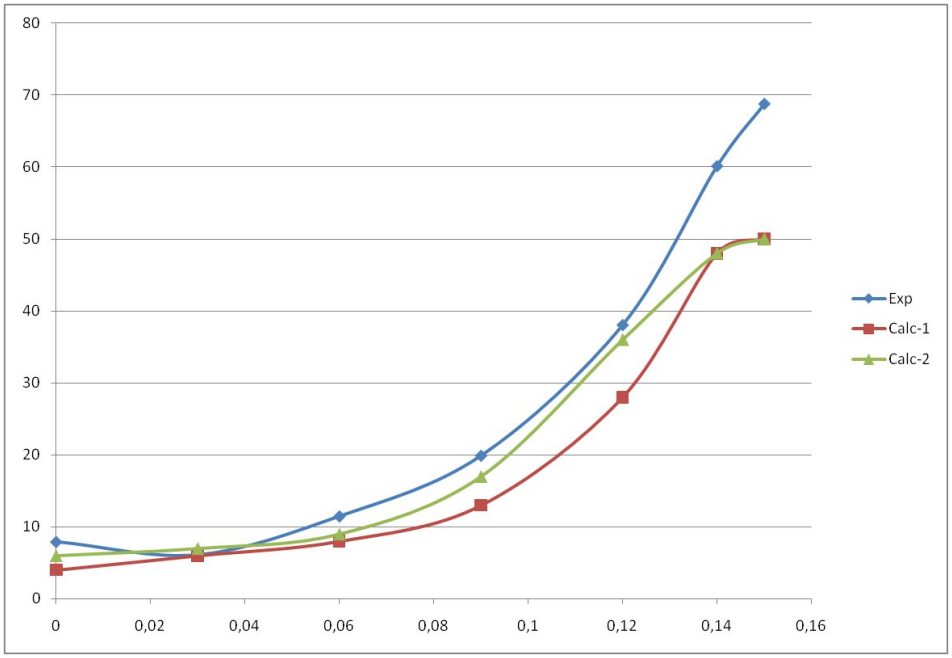

Figure 4.11: Characteristic energy [cm^2/s^2] of the flow velocities oscillations on the border between the large vortices of the averaged flow measured in experiment and calculated with LES turbulence model on $3.6 \cdot 10^6$ and $15 \cdot 10^6$ elements meshes

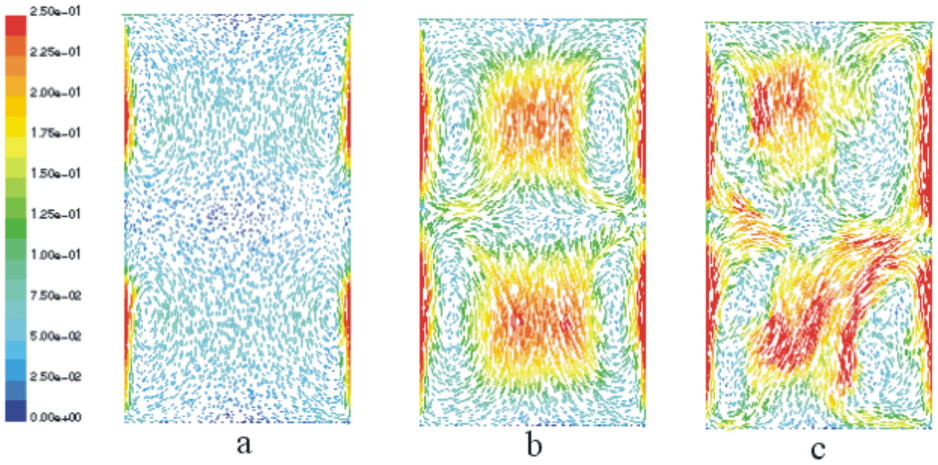

Figure 4.12: Flow pattern $[m/s]$ after 2, 6 and 10 seconds of calculations

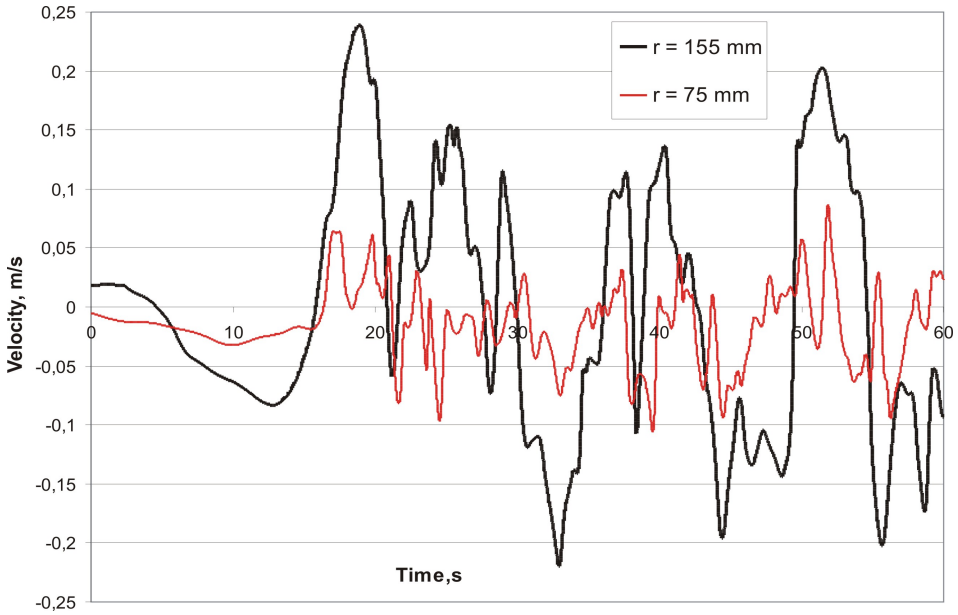

Figure 4.13: Axial velocity oscillations in the points located between the large vortices of the averaged flow calculated with LES turbulence model on $3.5 \cdot 10^6$ elements mesh

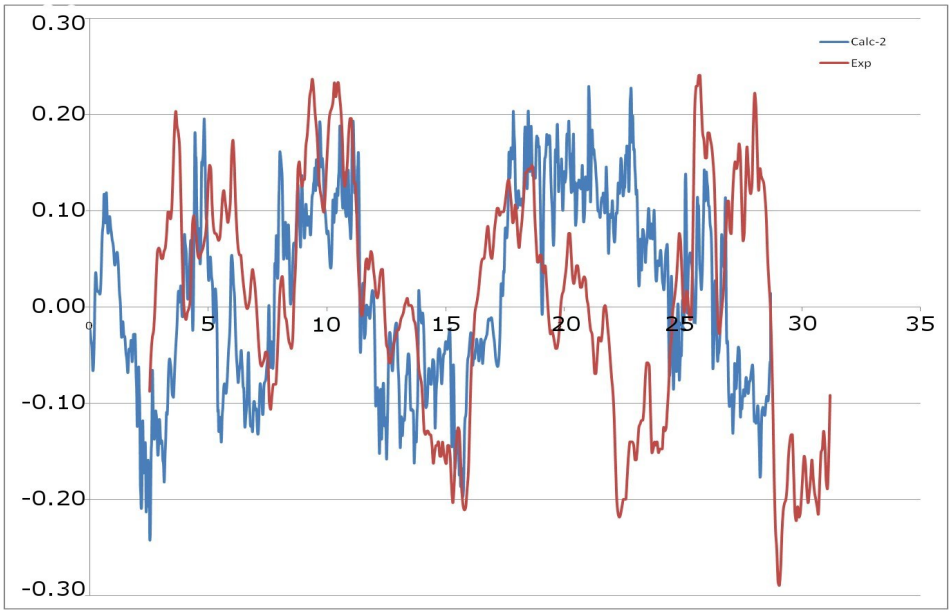

Figure 4.14: Axial velocity oscillations measured in model furnace (red) and calculated with LES turbulence model on $15 \cdot 10^6$ elements mesh (blue)

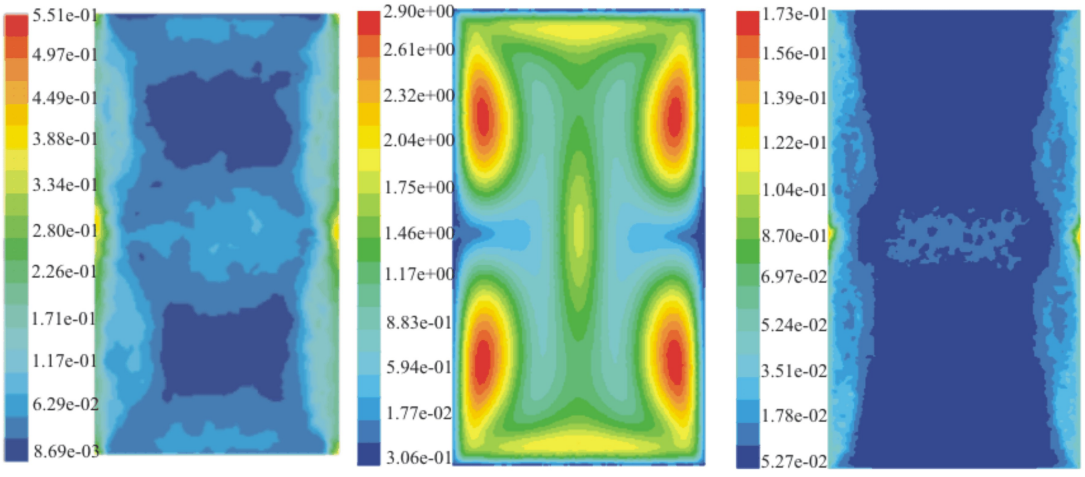

Figure 4.15: Turbulent viscosity distribution $[kg/m \cdot s]$ in case of $k - \epsilon$ (middle) and LES 3D modeling on mesh with $0.23 \cdot 10^6$ (left) and $3.5 \cdot 10^6$ (right) elements

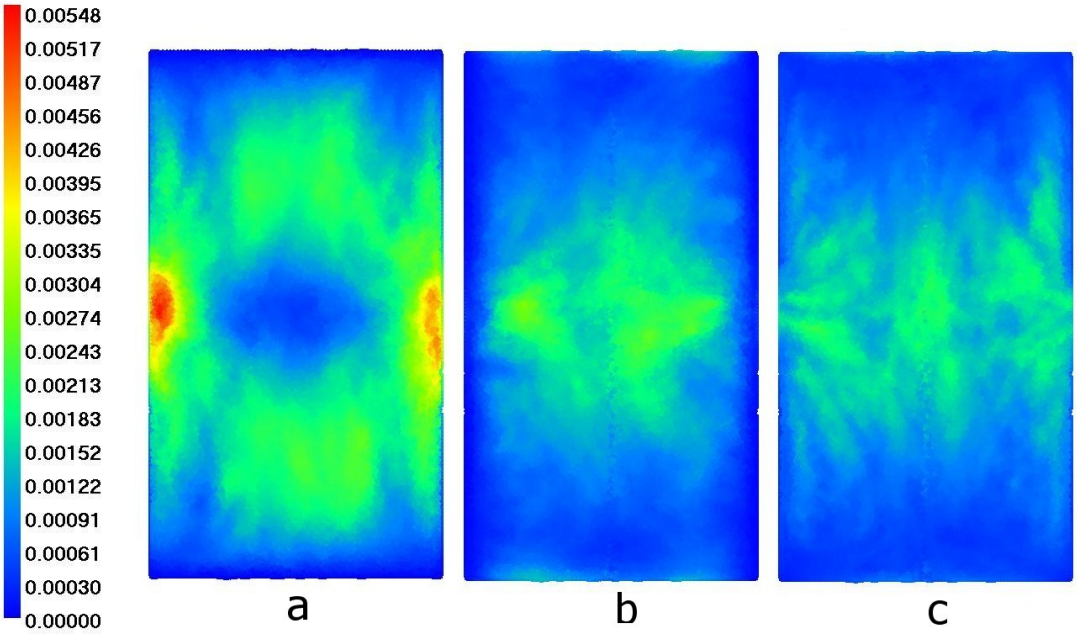

Figure 4.16: Distribution of the components of the characteristic energy of the flow velocities oscillations calculated with LES turbulence model (a - axial, b - radial, c - tangential).

oscillations' kinetic energy as shown on Fig. 4.16. It can be seen that these distributions are significantly non-homogenous, and different components have different patterns. While axial velocity oscillations dominate at the middle-height close to the crucible wall and on the axis, the other two components are more intensive in the central region of the crucible's volume. This means, that the oscillations are non-isotropic and this phenomenon can not be captured by the conventional turbulent models, because of their assumption about isotropy of the turbulence.

4.5 Particle tracing approach

The discrete particle tracing approach has been carried out to illustrate convective scalar transport mechanism in the considered flow. In the very beginning virtual particles are placed on the top of computational domain. These particles

are assumed to have the same density as the fluid and this leads to the expectation that their path will coincide with the streamlines of the flow. When the flow in closed domain without inlets and outlets is stationary, the streamlines are also closed and particle trajectories should be looped. In this case it is improbable that particle will penetrate into the neighboring flow region if the turbulent transfer is neglected. Therefore, transport processes between the main flow eddies generally would have diffusive character in steady-state flow. In this case scalar exchange intensity will strongly depend on the semi-empiric turbulent parameters such as turbulent viscosity and turbulent Prandtl ($Pr_t = c_p\nu_t/\lambda_t$) or Schmidt ($Sc_t = \nu_t/\rho D_t$) number. Both latter parameters magnitude often depends on the type of fluid and flow properties and has to be determined experimentally. The flexibility of using such approach for different industrial installations is rather low. The sub-grid viscosity models seem to have more universal character. Transient

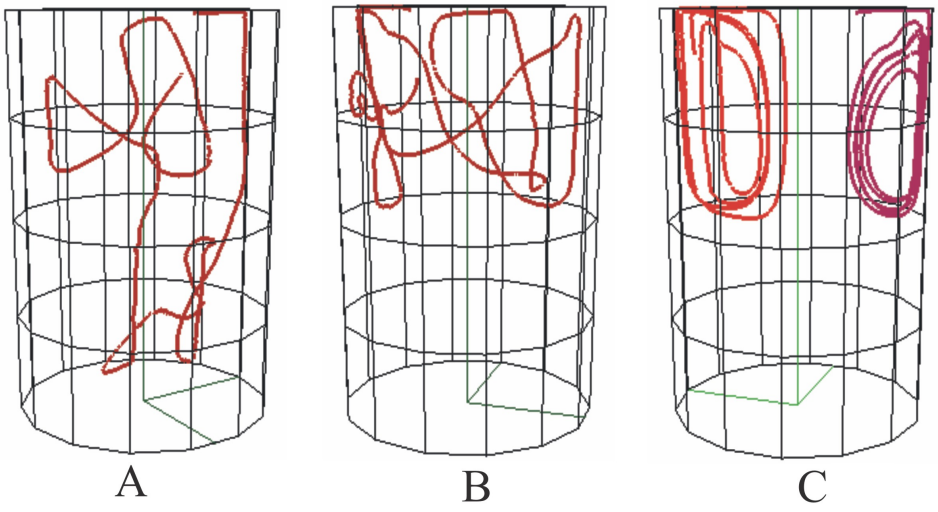

Figure 4.17: Results of particle tracing A, B in transient simulation and C in long time period averaged flow

simulations with a small time step and appropriate meshing allow resolving the wide range of flow formations involved in scalar transport. Particle trajectories, traced in such instationary simulations, show that estimated convective mass exchange between the main flow eddies is quite intensive (Fig. 4.17a,b). Four

Table 4.4: Properties of the industrial furnace

Property	Value
Radius of crucible	0.49 m
Height of inductor	1.34 m
Density	6800 kg/m^3
Dynamic viscosity	$6.3 \cdot 10^{-3}$ kg/m $\cdot$ s
Conductivity	$7.7 \cdot 10^5$ S/m

particles were launched simultaneously at $z = H, r = R/2, \delta\varphi = \pi/2$ and traced for 20 seconds (about 5-6 eddy turnover times). The choice of starting position was chosen also for conformity with industrial alloying process, when additional components are added on the melt surface. The typical tracing result states, that most particles don't stay in one eddy longer than two or three turnover times. Hence, it is possible to come to the conclusion that convective transport mechanism plays significant role in the heat and mass exchange between the main flow eddies. The same tracing procedure was used with the time-averaged velocity field from transient LES calculations. As it was expected, all particles rotated in the initial eddy with relatively small azimuthal drift (Fig. 4.17c).

4.6 Numerical modeling of melt flow in industrial-sized furnaces

The turbulent melt flow in an industrial furnace (Fig. 4.18) was simulated at the next stage of the LES numerical investigations. This furnace has a melt volume of about $0.9m^3$ at 100% filling level. Table 4.4 summarizes the main properties of the furnace and the melted material (grey cast iron). The three-dimensional model consisted of about 7×10^5 elements and the time step in the transient calculations was 10^{-2} s. Industrial crucible furnace differs from the experimental installation with significantly larger linear dimensions, higher EM forces density and noticeable free surface deformation (meniscus). This deformation was calculated with the help of self-developed Delphi programm based on balance equation 2.17.

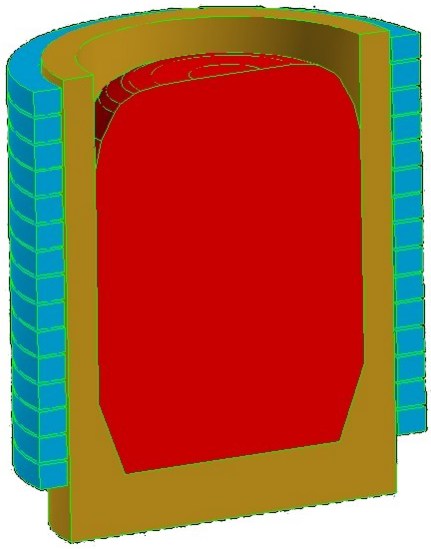

Figure 4.18: 3D model of the industrial furnace

The calculations results included the time-history of the velocity distribution in three orthogonal planes. These data allowed to receive the time-averaged velocity pattern (Fig. 4.19) as well as the information about the flow oscillations. This comparative analysis of LES and experimental data from model furnace allowed applying this numerical method also for industrial scale installations, and qualitatively similar phenomena was achieved:

- the period of the low-frequency oscillations became smaller - 2 seconds - because of significant increase of the rotational velocity of the flow eddies in accordance with the hypothesis concerning inertial waves (36), which period can be estimated with the following expression: $T \approx \mathrm{C} \cdot \mathrm{r_{ch}}/\mathrm{v_c h}$. The distribution of inertial waves along the axis of the vortexes may be one of the factors which disturb the regular flow pattern. Also, the instability can occur due to the two jets directed towards each other at the crucible wall. Further, this perturbation travel with the main flow and it is possible

to estimate its turnover time, which coincides with that of the vortex:

$$T \approx 2\pi(\frac{r/2 + H/2}{2})v_{ch} \approx \frac{\pi}{2}(r + H)v_{ch}. \quad (4.1)$$

Nevertheless, the initial vortex structure is hardly identifiable during the phase of fully developed large-scale oscillations. From the typical experimental data we consider: $r_c h = 0.08$ m, $v_c h = 0.15$ m/s (maximum time-averaged velocity on the symmetry axis) and C=10. For the industrial furnace, correspondingly we consider:$r_{ch} = 0.25$ m, $\mathrm{v_{ch}} = 1.5$ m/s. These data lead to an estimation that $T_I \approx 3$ s, which is very close to the period length derived from numerical simulation.

- initially axial symmetrical flow pattern becomes fully three-dimensional, but considering the time-averaged situation the symmetry of the flow pattern remains.

- the absolute values of the sub-grid viscosity are higher (Fig. 4.20) because of the increased cell size, but it's distribution is analogous to that in the model furnace (Fig. 4.15).

Numerically predicted maximal specific kinetic energy of the flow oscillations in the industrial furnace is more than two orders of magnitude higher than that measured ones in the model furnace. Although, the spatial distribution of the kinetic energy of the flow fluctuations corresponds to the experiment (Fig. 4.21), concerning, that the maximum is located in the zone between the macroscopic flow eddies close to the solid wall, where the kinetic energy values are 3-4 times higher than average. The intensity of the axial velocity oscillations $< v'_z >$ constitutes the most part of the full kinetic energy k, while two other components $< v'_r >$ and $< v'_\varphi >$ are at least three times smaller and their distribution is relatively homogeneous. Unlike the axial component k_z, the radial k_r and azimuthal k_φ components are mainly made up of the turbulent fluctuations ($f > 1$ Hz). Obviously, the significant difference in energy levels is caused by the previously mentioned dominating low-frequency oscillations near the crucible wall, which are the part of k_z. Therefore, any numerical simulation based on the time-averaged flow calculations, independently on the chosen semi-empirical turbulence model,

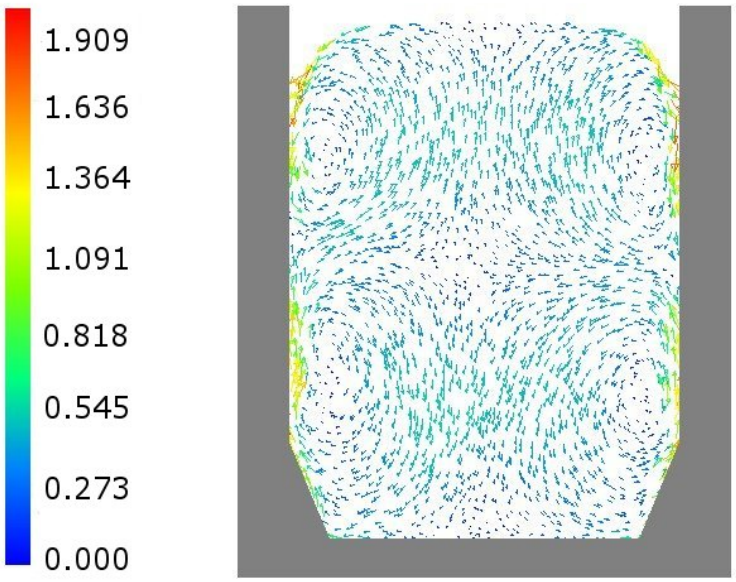

Figure 4.19: Time-averaged velocity distribution $[m/s]$ calculated with the LES turbulence model in the industrial furnace

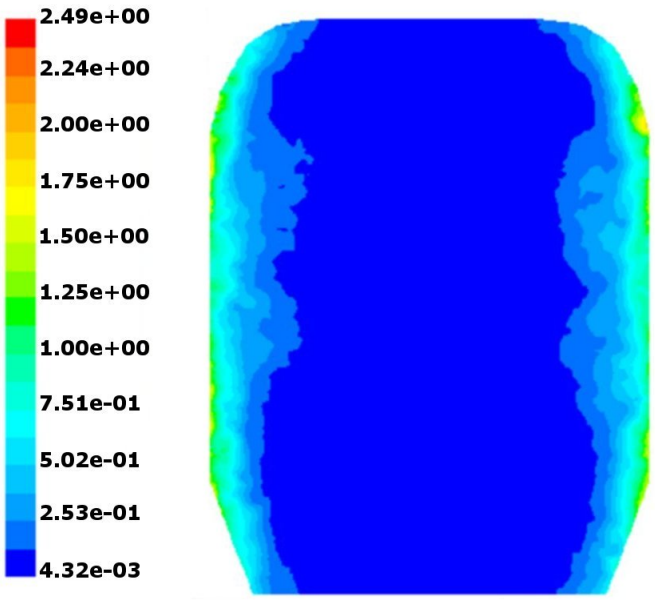

Figure 4.20: Intermediate sub-grid viscosity distribution [kg/m·s] calculated with the LES turbulence model in the industrial furnace

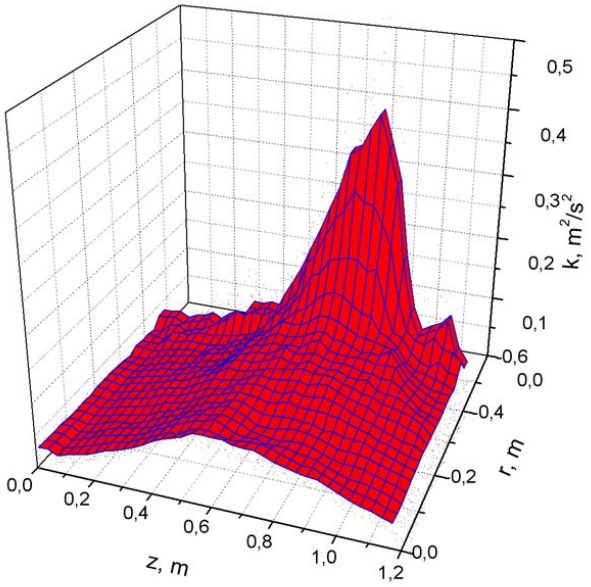

Figure 4.21: Kinetic energy of the velocity oscillations in industrial furnace calculated with 3D LES model

will not be able to predict correctly the heat and mass transfer processes between the macroscopic flow eddies.

5 Numerical simulation of melt flow in induction furnaces with cold crucible (IFCC)

5.1 Specifics of the IFCC

Growing attention is devoted in the last decades to the implementation of cold crucible melting technology. The induction furnace with cold crucible (IFCC) offers various technological and economical advantages, like high-purity cast products as well as melting, alloying and casting in one process-step (51; 52). This furnace consists of copper crucible made of base part and split wall segments which are isolated from each other in order to allow the alternating electromagnetic field, which is initiated by the inductor wound around the crucible, to couple with the charge material (Fig. 5.1). The eddy currents induced in the charge generate Joule heat for melting the metallic material. Both the crucible segments and the base plate are intensively water-cooled in order to prevent the crucible itself of being melted. As result, the charge material which is in contact with the construction parts, remains in the solid state (skull) and efficiently isolates the melt from the contamination. It should be mentioned, that the physical properties of the skull are significantly different from those of the liquid material, because of it's porous structure and it brings an unknown variable to the thermal balance of the system. Additionaly, the chemical composition of the solidified layer may variate and influence in this way the composition of the cast product.
With typical (for the installation described in this work) operating frequency of 10 KHz the most of the molten mass is being pushed from the walls by the electromagnetic field (semi-levitated) and the meniscus is formed, therefore pre-

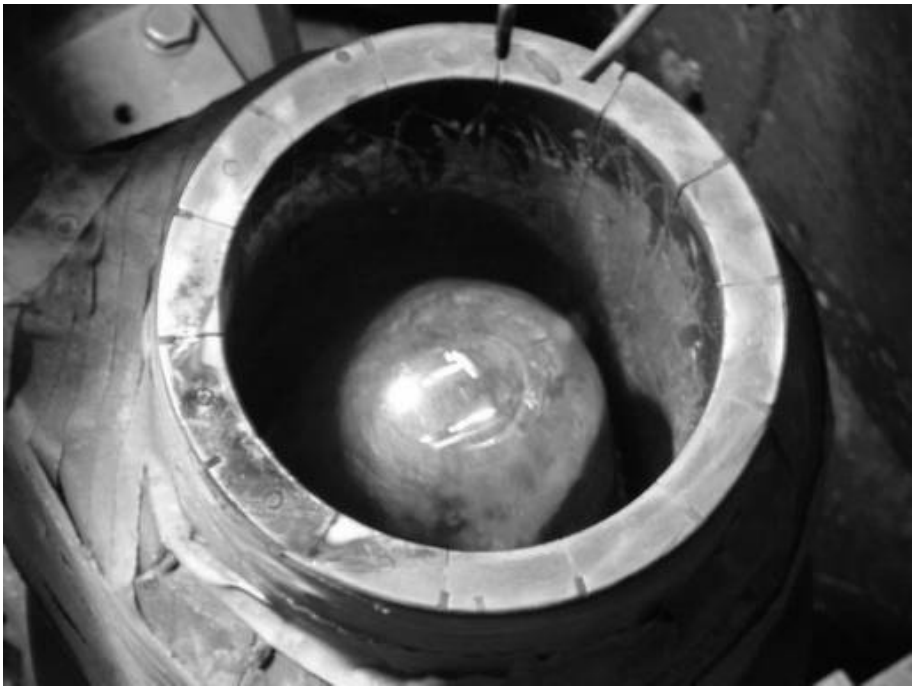

Figure 5.1: IFCC with Aluminium melt

venting the excessive heat losses and providing high overheating temperature. Also, the intensive stirring driven by the Lorentz forces assures good chemical homogenisation of the melted alloys. Melting process can take place in normal or controlled atmosphere as well as in vacuum. The process itself can be periodical with separate pouring (trough the nozzle or by tapping the whole crucible) into the forms, or uninterrupted, when bottom of the crucible continuously descends with solidified material and new charge material is being loaded from the top.

The research work on further optimization of the IFCC is concentrated on the improvement of the electrical and thermal efficiency of the installation. Optimal operation considers minimal melt contact area with the crucible material in order to decrease the heat losses from the melt and therefore to achieve higher overheating temperature. The increased operational temperature also reduces the thickness of the skull layer, which, as it was mentioned before, has influence on the final alloy composition. Additionally, pushing the molten material away prevents interaction of the chemically agressive melt components with the cru-

cible and allows to extend the lifecycle of the furnace. On the other side, the electrical efficiency is greatly reduced when melt is pushed too far, because of the worse electromagnetic coupling between the currents in the inductor and the ingot. Therefore, the right choice of the ratio between the meniscus height (H) and crucible inner diameter (D) is one of the main targets of the numerical optimization. The wide choice of the parameters which can be adjusted in order to influence the H/D relation include external current strength and frequency, the crucible diameter itself, the melt mass, the crucible design (e.g. number of sections) and others. Considering non-obvious correlations between the effects of changing these input data, the optimization of the IFCC becomes non-trivial task.

The numerical modelling of the melting of the metals in IFCC has been performed since decades, with early works mainly focused on electromagnetic aspects (53; 54; 55; 57). The described models gave the possibility to estimate how the efficiency of the melting process depends on various parameters of the installation. The 3D electromagnetic calculations were also reported already in 90-ties (56; 58; 59). They often used boundary elements method in order to save computational resources exploiting the fact that at typical for IFCC high field frequencies the penetration depth was very small. The modelling of the melt flow in the cold crucible had mainly two-dimensional character based on modifications of the RANS models (60; 61; 62).

5.2 Experimental investigations

The described meniscus formation is an important part of the melting process in the furnace with cold crucible. Therefore, the experimental investigations should involve this phenomena. This leads to the requirement for high-intensity magnetic fields, which are able to push the melted material from the crucible walls. At the same time, this innevitably causes the proportional generation of Joule heat inside the ingot. The resulting rapid temperature increase may provide complications when low-melting-temperature alloys are used. Possible technical solutions for this problem often will bring additional factors to the process, which should

Table 5.1: Physical properties of Aluminium and Titan-Aluminium alloy

	Al	TiAl
Electrical conductivity $[10^6\ S/m]$	3,6	1,0
Density $[kg/m^3]$	2300	3750
Melting temperature $[^oC]$	660	1500
Dynamic viscosity $[10^{-3}\ kg/m \cdot s]$	1,29	1,1
Specific heat $[J/kg \cdot K]$	1133	1000
Heat conductivity $[W/m \cdot K]$	120	70
Penetration depth @10 KHz $[mm]$	2,6	5,0

be then included in the numerical model. Considering this, the usage of aluminium as a model melt was approved to be a compromise. It has lower melting temperature than the Titan-Aluminuim alloy (Table 5.1), which is more popular subject of practical applications, but it can be melted in the same installation without the need of any adjustments to the process. However, the experimental investigations in cold crucible induction furnace with aluminium melt are usually more challenging than measurements in Wood's alloy. It is because of significantly higher operating temperature of about 700^{o}C and very reactive chemical nature. However, it is possible, with some adjustments, to use the similar measuring techniques as in case of the Wood's metal. The use of the Wood's metal as a model melt in cold crucible is complicated due to it's high density and difficulties with the control of the thermal regime. The latter one is important since the overheated Wood's metal may produce toxic fumes wich contain Cadmium and are dangerous for experimentator's health. The experimental investigations included two separate measurement's series: 1) temperature measurements; 2) velocity measurements. Both of them were performed using 6 kg pure aluminium (99.5%) in the cold crucible with a radius of 78 mm and a height of 260 mm

Figure 5.2: Temperature measurements in liquid Aluminium with thermocouple placed in a protective ceramic tube.

(Fig. 5.1). The output power of the generator was 200 kW at the frequencies 9-10 kHz. The meniscus height from the last contact point with the crucible wall to the melt top reached up to ≈225 mm under those conditions. With these process parameters the meniscus shape of the melt surface is quite stable and therefore it is possible to perform detailed investigations of the free melt surface itself, the temperature field and the turbulent melt flow. The characteristic numbers of the melting process are provided in the Table 5.2.

5.2.1 Temperature measurements

The temperature distribution was measured using NiCr-Ni thermocouples, which were placed in a protective ceramic tube (Fig. 5.2) to avoid their destruction in the very aggressive aluminium environment during long-lasting experiment. However, due to this protection, the thermal inertia of the thermocouple was quite long (≈2.75 s), therefore, it was possible to measure only time-averaged temperature values. In order to investigate temperature oscillations in several

Table 5.2: Characteristics of the experimental IFCC with Aluminium melt

	Aluminium
Crucible radius, [m]	0.078
Melt mass, [kg]	6
Operational frequency, [Hz]	9500
Current strength, [A]	4600
Characteristic velocity, [m/s]	0.30
Reynolds number	4.3×10^4
Prandtl number	0.012
Magnetic Reynolds number	0.1

characteristic points of the melt, the thermocouple was used without ceramic protection. In this case the response time became approximately 0.8 s, but the operational time for one thermocouple decreased to the 10-15 minutes. Obtained temperature oscillations (Fig. 5.3) can be compared with the results of the transient 3D modeling using LES. The very long-period temperature changes (with characteristic times of 1-2 minutes) also were noticed during measurements. They can be explained with unstable thermal regime of the entire melt, e.g. when some part of the skull becomes melted and mixed with other material. And, if we apply the high-pass filter to those data, then oscillations amplitude is within range of 1-2 degrees.

The time-averaged temperature field as it was measured is shown on the Fig. 5.12. There is clearly seen how temperature distribution is influenced by the thermal boundary conditions. The lowest temperatures are at the water-cooled bottom, where was detected the solid skull layer with thickness about 10 mm. Also the radiation losses from the free surface lead to the formation of relatively cold area at the top. The highest temperatures are observed in the

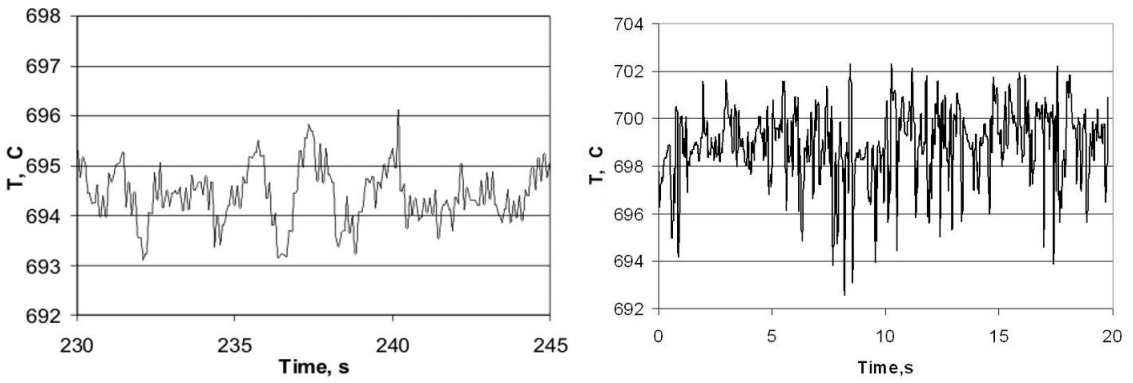

Figure 5.3: Temperature oscillations on the axis measured (left) and calculated (right) in aluminium melt.

intensive inductive heating region, which is located in the area surrounding the contact point of the melt surface and crucible wall (Fig. 5.9). The temperature distribution in the rest of the melt is more or less homogeneous.

5.2.2 Velocity measurements

With the melt temperature higher than the maximum working temperature of the velocity sensors with the permanent magnet (about 450^{o}C) there appears distinct, partially irreversible, not reproducible weakening of magnetization. That is why the sensors with the permanent magnet, measuring the flux, have very limited application in liquid aluminium. No induction methods for measuring local flow velocity in liquid metals within the temperature range between 600^{o}C and 700^{o}C are known from the literature (9). That is why for the application in the aluminium melt the electromagnetic velocity sensor shown in Fig. 5.5 was developed and made (34).

Unlike the probe rod with the permanent magnet, the magnetic field of the electromagnetic sensor is created by the excitation coil along which the direct current is flowing. The case of the sensor, magnetic core and the coil case are made of steel. During the measurements the coil current was kept on the level of 10 A. The corresponding magnetic field strength achieved 0.03 T. The indicated level of the current was chosen taking into consideration the provision possibly high strength

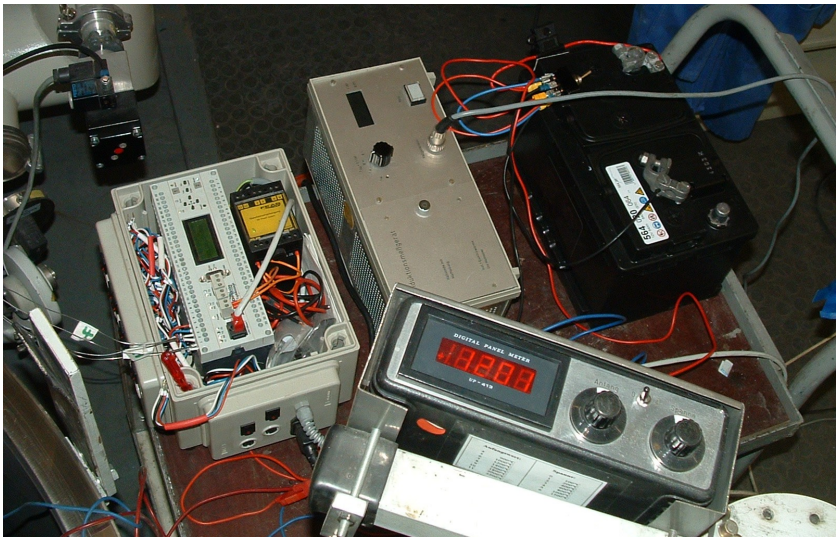

Figure 5.4: Equipment for velocity measurements in laboratory IFCC

of the field with the limited density of current in the coil wire. Low corrosion durability of the flow velocity measuring sensor in the aluminium melt appeared to be the greatest problem in the measurements performed. After 10-20 minutes of operation the magnetic steel core and the steel case were so greatly corroded that the sensor became unfit for the further operation. To prolong the lifetime of the sensor at the expense of other materials application such as platinum or tungsten, is impossible as they do not have long durability against the aluminium melt (9). The attempts to prolong the operation period of the sensor protecting it with the ceramic cover did not bring the desired results as well.

The device for measuring velocity of aluminium alloys consists of electromagnetic sensor, source of direct current of the sensor coil, system of the sensor fixation in the specified point of the melt, data acquisition system and connecting wires and cables (Fig. 5.4). All sensors were calibrated in the induction crucible furnace with Wood's metal, which has melting temperature of 72^oC. The measured sensitivity of the sensors varied through the range $0.3 - 0.8$ V/(cm*s^{-1}). The problem of zero drift was possible to solve with periodical changing of the direct current power supply source polarity in the process of measurement.

Due to to the mentioned technical problems it was possible to perform velocity

measurements only for one set of process parameters and the main results of these investigations in the liquid aluminium have shown, that flow pattern consists of two vortexes and the zone of their interaction is located between z=70 and z=90 mm. The maximum axial velocity detected in the upper vortex on the symmetry axis was 0.4 ± 0.05 m/s.

5.3 Modeling and investigation of electromagnetic effects in IFCC

The cold crucible installation (Fig. 5.6) has basically axis-symmetric geometry, but at the closest look it is not so, because of the gaps in the crucible wall. Since the crucible sections are made of conducting material, the eddy currents are excited in them and the electromagnetic field distribution is significantly influenced. Therefore, two-dimensional EM simulations of IFCC should take into account this phenomenon. There are several ways to do this: implement the effective magnetic permeability of the crucible material (40), or estimate the eddy currents in the walls. The use of mentioned approximations is complicated by the fact, that the amount of melt in the crucible and its shape changes the field as well. Hence, the qualitative estimations, which are suitable for one system, may produce incorrect results for another. Also the evaluation of power balance in the system may be misleading, because in reality significant amount of the electrical losses belongs to the slit crucible (about 50%). 2D model does not calculate these losses directly. Initially the 2D approximation has been used taking into account the ratio between the crucible section and gap width. This approach was tuned for our experimental installation and was used for the series of calculations with varied diameter of the crucible. It's main advantage is the short solution time, which is significant for the iterative process of meniscus shape calculation. However, the constant growth of the computational power allows us to perform the three-dimensional calculations on the common workstation. The 3D simulation with sufficient mesh resolution can be completed within reasonable time period. The commercial software ANSYS was used for this purpose.

The experimental IFCC, which was modeled, is built of 14 segments and has

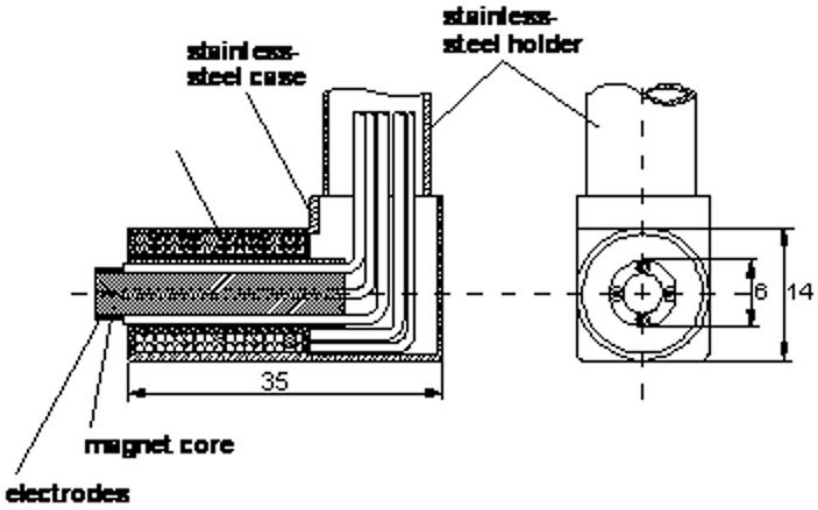

Figure 5.5: Electromagnetic sensor

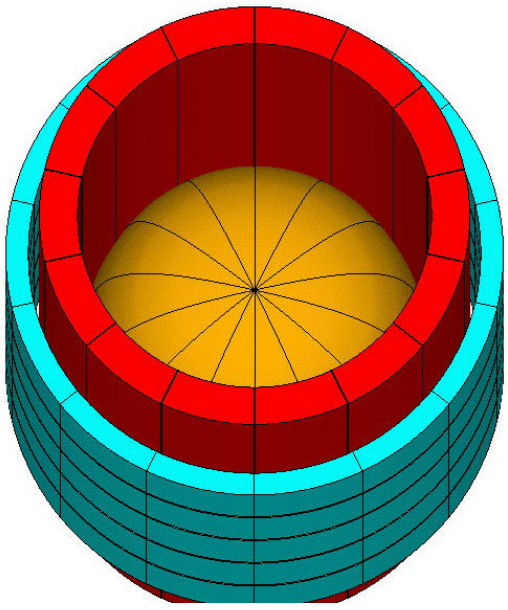

Figure 5.6: The 3D model of the IFCC, which contains parts important for the electromagnetic analysis.

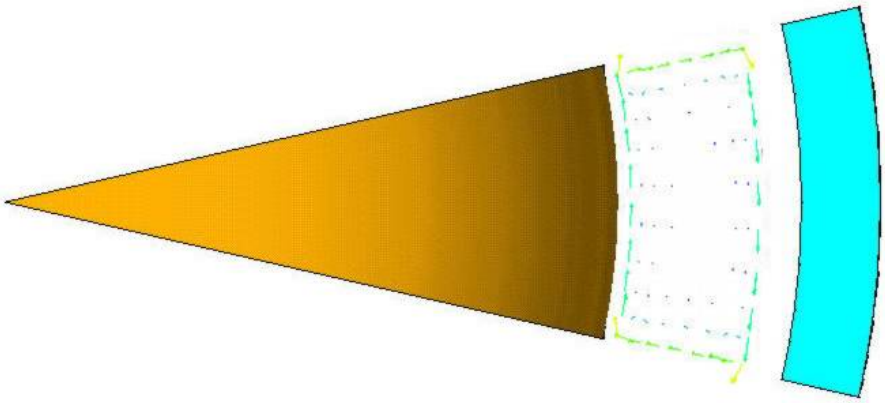

Figure 5.7: The top view of the modeled part of the cold crucible geometry. The cuurents in the water-cooled secion are shown.

the inner crucible diameter of 16 cm. The 5-turn inductor height is about 20 cm and the operational power varies from 150 up to 200 kW. The 3D model contains a sector with half of crucible segment and half of the attached gap, which in our case corresponds to the 12.86 angle. The (Fig. 5.7) shows double size of the typical model with the aim to illustrate the distribution of the cuurents induced in the section. The flux-parallel condition is applied on the side boundaries, but on the other boundary planes the vector-potential is set to zero. The current strength is applied to each inductor turn and its distribution inside the coil is calculated during the solution. The results of simulation contain induced currents in all conducting regions; therefore it is possible to calculate the total power losses in the whole system. The use of 3D electromagnetic model also brings another advantage because it gives the non-symmetrical (real) Lorentz force and Joule heat distribution in the melt. Figure 5.8 shows how the intensity of Joule heat sources at the melt surface depends on the angular position for different heights. The shape of the melt interface is calculated by establishing point-to-point balance of all involved forces. The equation is

$$\rho g \delta z - P_{EM} - \gamma(1/R_1 + 1/R_2) = \delta P \tag{5.1}$$

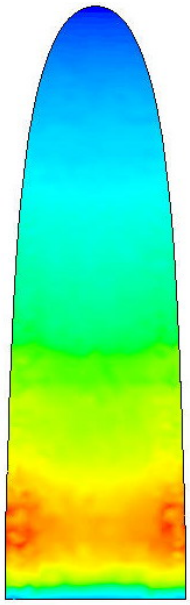

Figure 5.8: The Joule heat sources distribution on the melt surface.

where $P_{EM} = B^2/2\mu$ is the electromagnetic pressure, is the surface tension coefficient and R_1, R_2 are the curvature radii. The surface profile is divided into the equal sections by the 40 nodes. Then the shape is adjusted in iterative way, until the δP becomes the same for each point. The electromagnetic calculations are performed on a 3D ANSYS model. The obtained magnetic field intensity data are used then by external code which makes shape adjustments.

The Fig. 5.9 shows typical distribution on the intensity of Joule heat sources in the TiAl melt for different H/D ratio. The steeper is the the meniscus, the closer to the coil middle-height is the maximum of the induced heat. The distribution of the force density has obviously similar character, with force vector directed into the melt and perpendicular to the surface. The maximum of Joule heating corresponds to the maximum of Lorentz forces, which usually divides flow into the two vortexes.

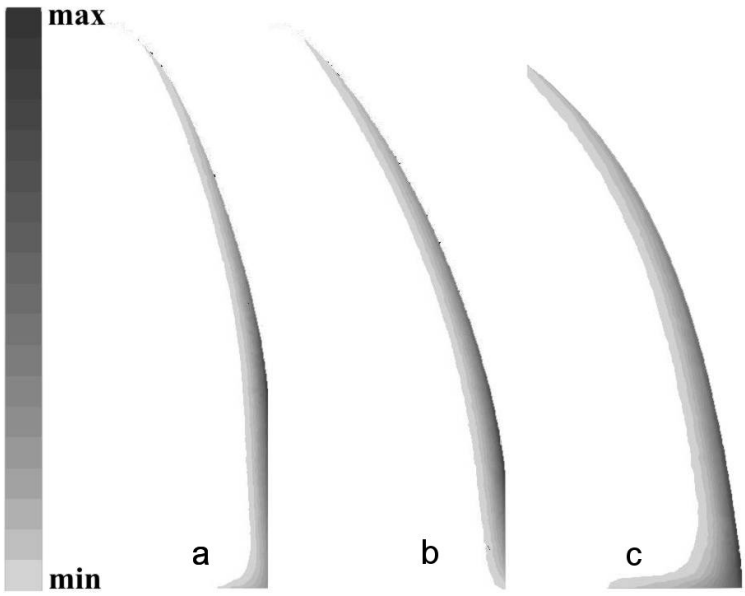

Figure 5.9: Joule heat sources distribution in TiAl melt for different H/D ratio. a) 1.67; b) 1.20; c) 0.84

5.4 Modelling of the fluid flow and temperature distribution

The RNG modification of the k-ϵ model has been applied for the 2D simulation of the cold crucible melting process. According to previous numerical studies, it has delivered more accurate predictions about turbulence properties in the recirculated flows than the standard model. But, both of them usually underestimated the heat transfer intensity between the main flow eddies formed by the external electromagnetic force. As it is shown on the velocity plot (Fig. 5.10 left) the time-averaged flow pattern consist of two vortexes. The thermal boundary conditions for upper and lower vortexes significantly differ - the radiation from the free surface above ($\varepsilon = 0.4$) and water-cooled bottom below (the constant melting temperature was used in numerical model). The estimated heat flux distribution shows that only 6% of the thermal energy are lost due to the radiation. The rest of the heat is carried away with the cooling water through the crucible bottom. As far as the heat exchange between the two parts was

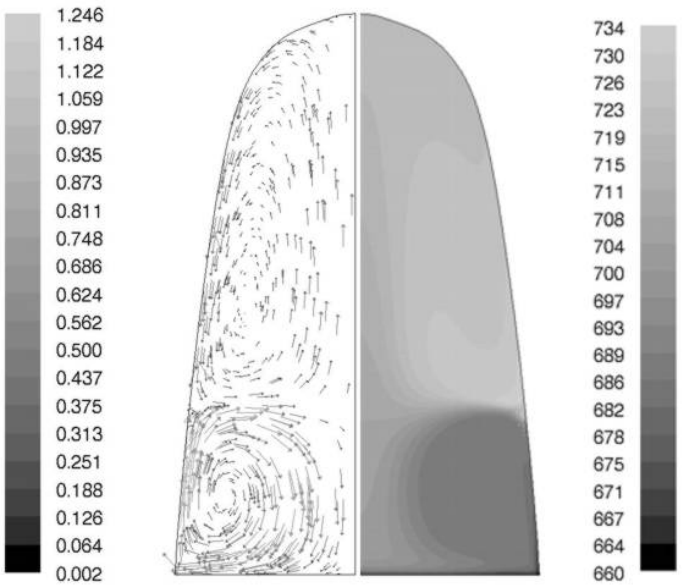

Figure 5.10: Velocity vectors (left, m/s) and temperature distribution (right, °C) calculated with 2D RNG $k - \varepsilon$ turbulence model

underestimated, the 2D steady-state simulation predicted too high temperature in the upper region of the melt (Fig. 5.10 right), which is not confirmed by experimental data (Fig. 5.12). Considering former experiences with modeling of the inductor furnaces (see previous two chapters) it was suggested that the use of the Large Eddy Simulation could better deal with this two-vortex flow pattern. These LES calculations ran on the three-dimensional model, which consisted of approx. 4 millions finite elements, with time-step 10 ms. It took about one month for simulation of 30 seconds flow development using parallel computation with 8 processors. The resulting time-average velocity field (Fig. 5.11) looks very similar to the one predicted with 2D steady-state k-ϵ calculations (Fig. 5.10), as well as quite good agrees with experimental observations. The maximal axial velocity on the axis in LES results is ≈ 0.35 m/s, while measured was ≈ 0.4 m/s (see above). However, 3D transient approach allows modelling accurately the heat transfer processes in such flows, where two or more recirculated eddies are interacting. The calculated flow pattern at the each time-step is not symmetrical and simulation shows that complex vortex structure is developing due to

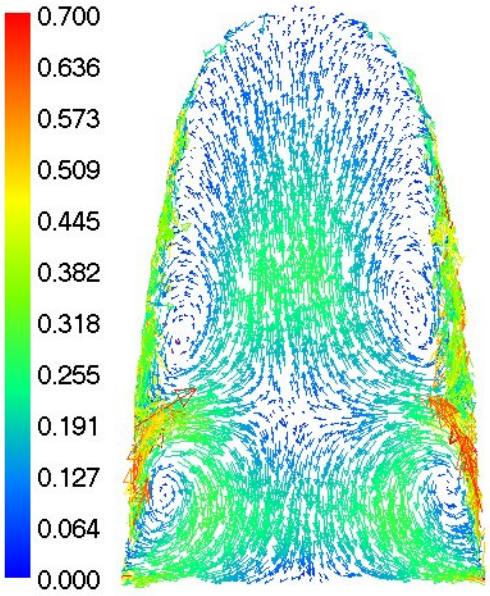

Figure 5.11: Time-averaged velocity vectors (m/s) calculated with 3D LES turbulence model

the turbulent and low-frequency instabilities, especially in the zone of the main two eddies interaction. Those unstable vortexes, which have size up to half of characteristic radius and lifetime of several seconds, are transferred by the flow in the different regions of the melt. Observed phenomenon provides convective heat transfer mechanism, which is possible to simulate numerically only using transient three-dimensional calculation techniques. Also, in the pictures series with temperature field at the consequent time-steps, it can be observed how relatively cold melt masses from below penetrate into upper vortex area and are dissolved there. The time-averaged temperature distribution calculated with LES is more homogeneous, than in case of 2D k-ϵ modelling and resembles the measured temperature field (Fig. 5.12). The temperature oscillations (Fig. 5.3) also look similar to those received in the measurements. It should be taken into account here, that higher frequencies in measured oscillations are "filtered" by thermocouple, while the time step in the calculations was 0.01 s.

The main noticeable disagreement with measurements is seen in the lower vortex region directly at the melt surface. The temperatures in this area seem to be un-

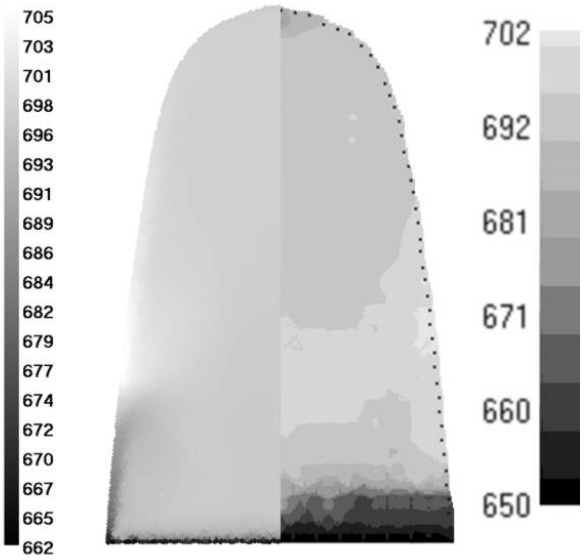

Figure 5.12: Measured (right) and calculated with LES (left, time-averaged) temperature distribution in aluminium melt in IFCC [°C]

derestimated in simulation, if we are comparing with the experiment. Probably this is caused by too primitive radiation model on free boundary, which does not take into account the presence of another hot surface (crucible) just opposite of the free surface. Therefore, it could lead to the overestimation of radiation heat losses.

The 3D numerical investigations of TiAl melting process produced similar results in terms of transient and time-averaged flow pattern. The first one is very unstable with practically no symmetry at any given time moment, which leads to the intensification of the temperature homogenization. The (Fig.5.13) shows as example the temperature distribution in TiAl melt with 0.1 seconds interval. It can be seen, that there is no clear interface between the colder and hotter regions unlike in the predictions of 2D calculations. The melt mass was the same 6kg, but the meniscus height in this case is lower due to the increased density of the TiAl material (1.6 times heavier as Aluminum). The flow velocities are slightly higher (maximal average velocity at r = 0 is about 55 cm/s), therefore the temperature distribution is more homogeneous, than in aluminium. Calcu-

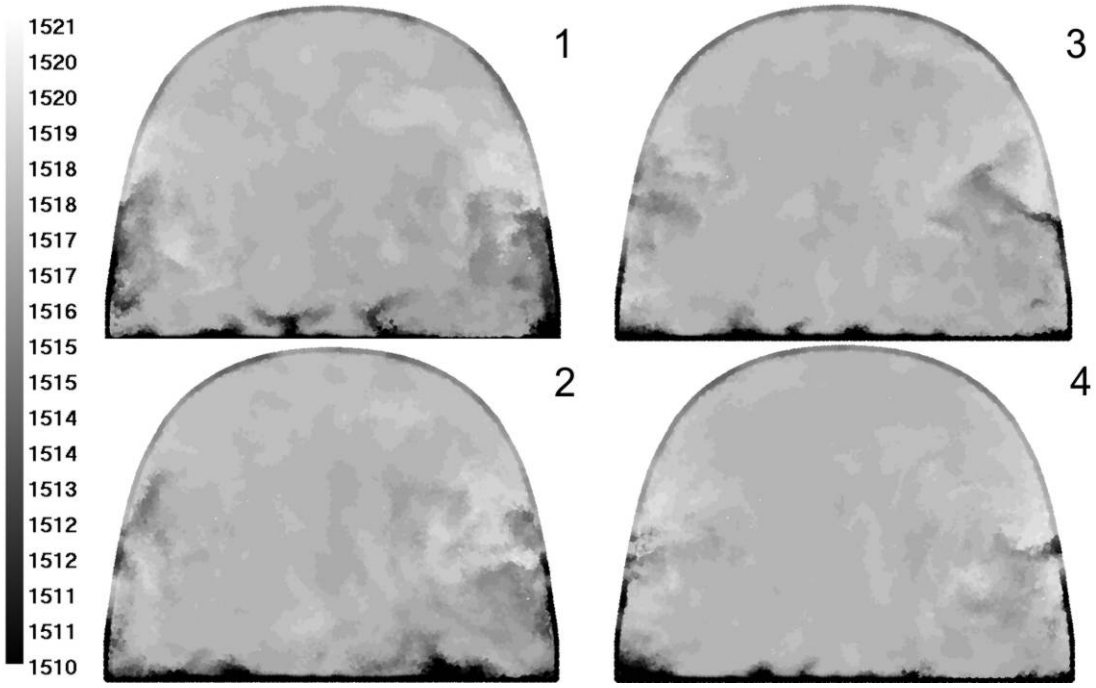

Figure 5.13: Instationary temperature distribution in TiAl alloy with 0.1 second interval [°C].

lated temperature oscillations have similar amplitude (3-4 K) as these measured in aluminium (Fig.5.14).

Due to the noticeably lower H/D ratio of the melt shape, the low-velocity zone exists in the middle of the bottom region, which may lead to the thicker skull layer above the water-cooled base. Therefore, the modification of the crucible's geometry or load is considered as a possible way to improve the efficiency of the process.

There were performed calculations for the three different H/D ratios (Table 5.3), but the power induced in the melt was kept the same. The Fig.5.15 shows the time-averaged velocity and temperature distribution for the existing crucible geometry, but the Fig.5.16 shows the futher results for two two proposed ratios: 1.20 (left) and 1.67 (right) additionally to the 0.84 ratio shown on Fig.5.15. As it can be seen, the flow is more intensive near the central axis in case of smaller diameter crucible. This can prevent the formation of the thick layer of the solid-

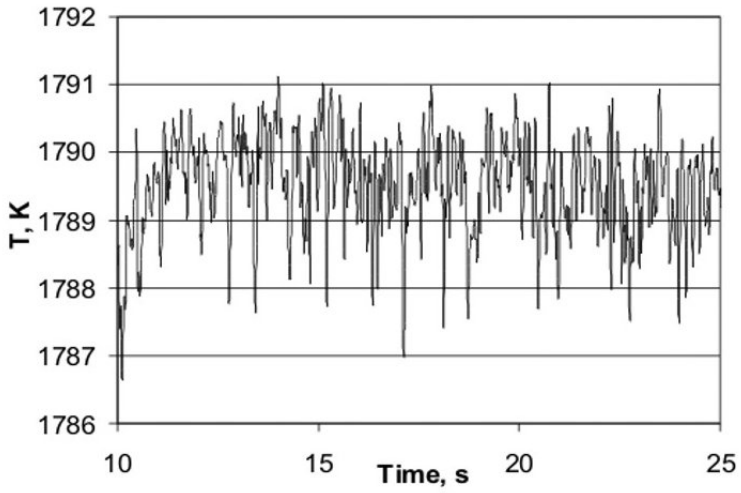

Figure 5.14: Temperature oscillations calculated for TiAl melt.

ified material at the bottom. But, at the same time, the melt has larger contact area with the crucible walls, which can lead to the changes in the electromagnetic forces and Joule heat sources distribution in the melt (Fig. 5.9), as well as to increased heat flux to the water-cooled slits. But, the comparison of electrical efficiency of these systems show (Tab. 5.3), that only about 18% of the full power are induced in the melt in case of H/D=0.84, while for the larger ratio it is 36%. Therefore, the same amount of Joule heat can be generated with significantly lower total energy consumption.

Also, the influence of the electromagnetic field frequency was studied (Table 5.4). The Fig.5.17 demonstrates the melt shape and the time-averaged flows for two cases: 5 and 20 kHz. The melt height decreases at higher frequencies (the induced Joule heat was kept about the same value of 40 KW). The velocities are noticeably smaller in the 20 kHz case (almost twice on the axis), which may lead to the less intensive mixing. These particular calculations show, that maximum temperature for 20 kHz is by 7 K (or 28% from temperatures range in the melt) higher then for 5 kHz. This can be considered advantageous, because increasing of the overheating temperature is useful for practical applications.

Table 5.3: Energetical parameters for melting process of 6kg of TiAl in IFCC with frequency 10 kHz and different crucible radii.

Crucible diameter, m	Ratio of the melt, H/D	Inductor current, kA	Total power, KW	Power in the melt, KW	Power in the melt, %	Overheat. temper., K
0.16	0.84	4.6	275.3	50	18.2	20
0.14	1.20	4.0	188.0	50	26.6	15
0.12	1.67	3.7	138.6	50	36.1	17

Table 5.4: Energetical parameters for melting process of 6kg of TiAl in IFCC with different frequencies.

Frequency, KHz	Ratio of the melt, H/D	Inductor current, kA	Total power, KW	Power in the melt, KW	Power in the melt, %	Overheat. temper., K
5	0.96	6.5	171	36	21	22
10	0.82	5.0	179	39	22	27
20	0.74	4.0	186	45	24	34

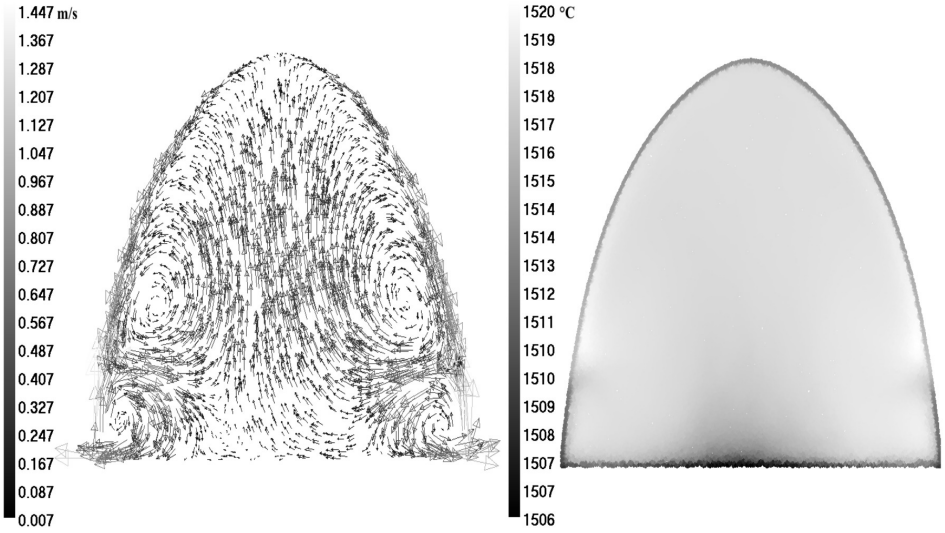

Figure 5.15: Time averaged velocity and temperature distribution in TiAl alloy.

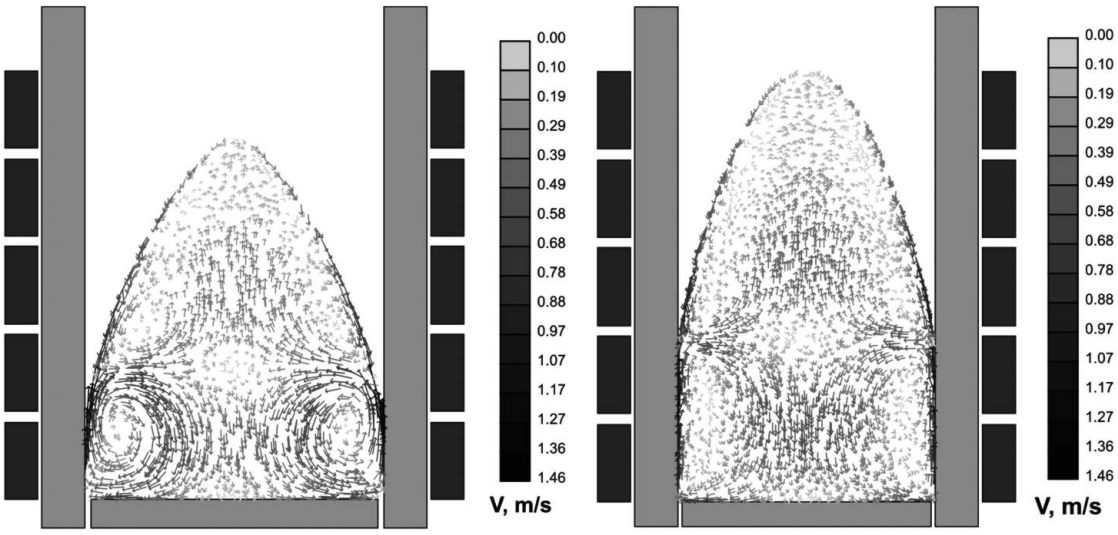

Figure 5.16: Velocity vectors of TiAl melt in cold crucible with H/D ratios 1.20 (left) and 1.67 (right).

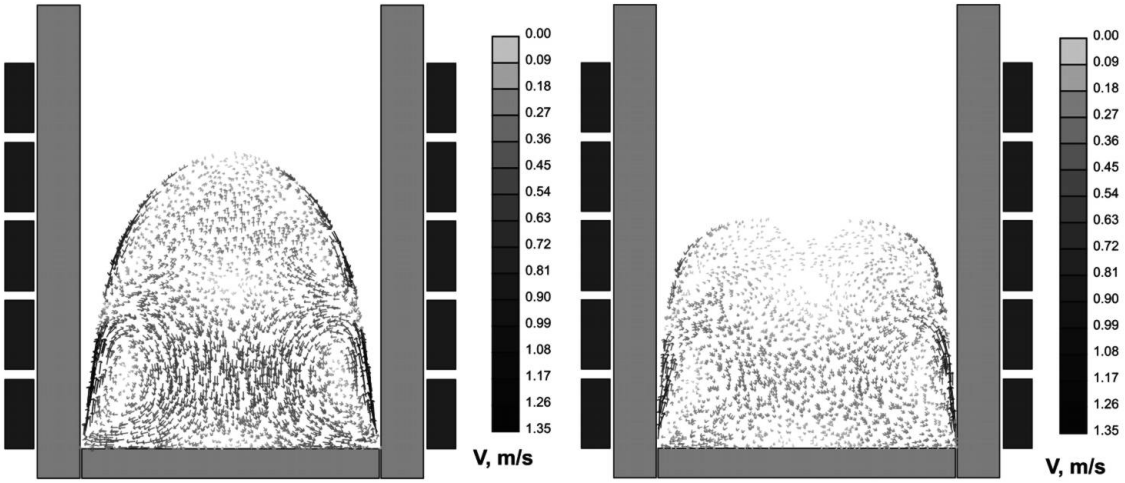

Figure 5.17: Velocity vectors of TiAl melt in cold crucible with e-m field frequency 5 kHz (left, H/D=0.99) and 20 kHz (right, H/D=0.77).

5.5 Skull modeling possibilities

The formation of solid layer on the crucible inner surface influences the temperature distribution and also the flow pattern. The composition analysis of the skull material which remains in the crucible after puoring, show that the elements distribution in it is not homogenous (41; 42). Particularly, in case of TiAl melting, the proportion of Titanium in the skull is noticably higher than in the melt. Therefore, the amount of the solidified material at the crucible walls during the melting process may influence the ratio of the alloy components in the melt, and as result, the quality of the final product.

The calculations involving the solidification process required more flexible temperature boundary conditions on the contact areas between the melt and water-cooled sections. However, the thermal resistance coeficient, which would characterize the heat transfer through the skull material is unknown and the series of additional specific experiments could be necessary in order obtain it's approximate value. Therefore, the rough estimation was made in order to achieve the thickness of the solid layer in simulation one order of magnitude with the ob-

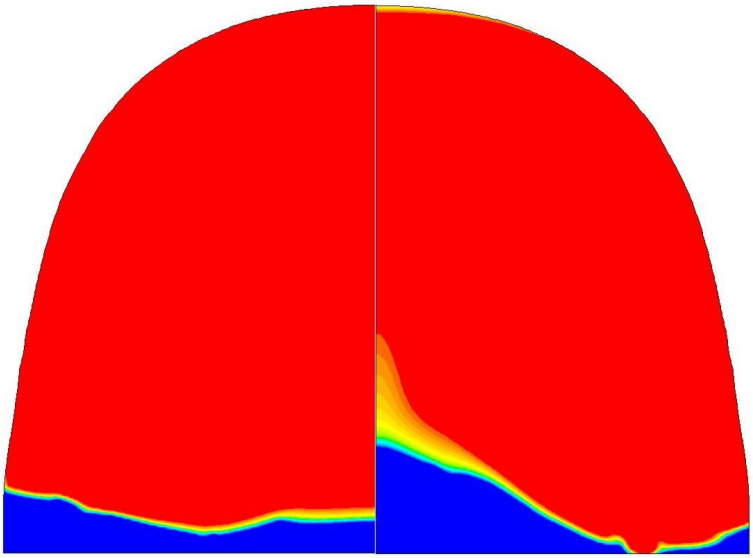

Figure 5.18: Skull distribution calculated with 2D RANS model with different Joule heat and Lorentz force distribution profiles. left) section middle; right) gap middle.

served in real melting process.

The 2D steady-state calculations with k-e model show, that there is noticeable difference in results depending on from which profile the heat sources and Lorentz forces are taken: opposite of the gap or middle of the sector wall Fig. 5.18. The skull thickness in both cases vary depending on radial coordinate, but in the profile which is opposite of the gap the layer of solidified material grows near the central axis. The Fig. 5.19 shows that the form of skull layer significantly depends on the flow pattern and, of course, the flow pattern is influenced by the skull form. The important difference between the left and right velocity distributions is that on the left hand side we see only one large vortex, but on the right there is pronounced second one. The thermal behavior of the single- and double-vortex system may differ, but 2D modeling is not able to take into account the 3D character of the cold crucible geometry. It is necessary to choose a profile with sources' distribution, but neither of them will be the correct one. This explains, why 3D approach could be more preferable.

There were performed calculations of the skull formation with 3D stationary k-ϵ

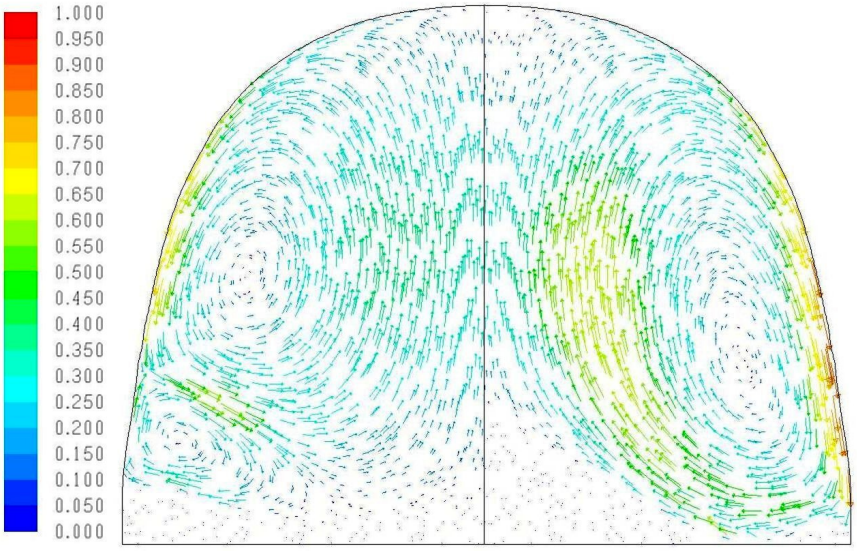

Figure 5.19: Velocity patterns calculated with 2D RANS model with fifferent Joule heat and Lorentz force distribution profiles. left) section middle; right) gap middle.

model and 3D input data from electromagnetic analysis. The Fig. 5.20 shows that the skull height changes not only in the radial, but also in azimuthal direction. However, if we compare these results to the experimentally obtained skull profile (Fig. 5.21), then it can be seen, that in reality the skull surface has less homogenous profile. This shows that the actual flow is far from axissymmetric and there are acting several local vortexes which are one or two orders of magnitude smaller then the main votexes of the averaged flow. These conclusions were also supposed by transient LES result.

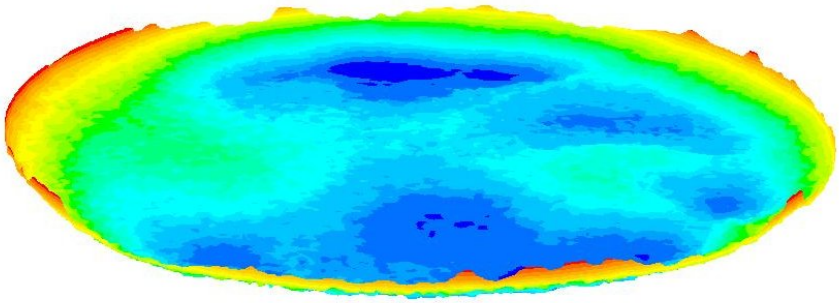

Figure 5.20: Skull height distribution calculated with 3D RANS model.

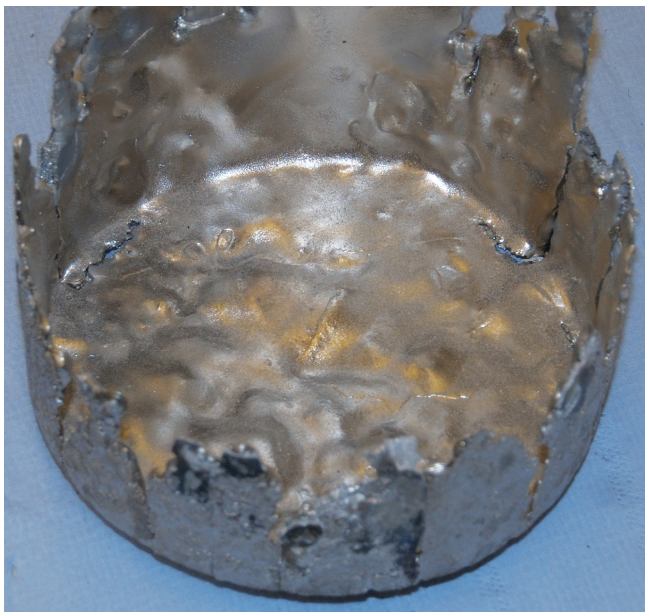

Figure 5.21: Solidified material after experimental TiAl melting.

6 Conclusions

Intensive numerical studies concentrated on applying the actually availaible methods for modelling of the recirculated melt flows have been done together with experimental investigations in the model induction furnaces. The comparative analysis shows a good coincidence between the numerical and experimental results when LES method is used not only in terms of mean flow, but also for the turbulent fluctuations and their kinetic energy. The studies reveal that the low-frequency velocity oscillations play a main role in convective heat and mass transfer when flow structure contains two or more large vortexes of the mean flow. Therefore, the correct estimation of the characteristic parameters of these oscillations applying the LES method leads to creation of a universal and reliable numerical approach, which can be used for solving fluid dynamics and thermal problems in practical melting applications. The main results of this work are summarized below:

1. The comparative analysis of the experimental and numerical results of the melt flow and temperature distribution in model crucible induction furnace has shown the inability of the RANS based steady-state and transient two-equation turbulence models to predict correctly the temperature distribution in the melt. However the averaged velocity field was modeled accurately. The hypothesis was suggested about significant role of the low-frequency flow oscillations in energy transfer inside the recirculated flow structures.

2. Transient three-dimensional hydrodynamic calculations with use of the newly developed modeling approach based on Large Eddy Simulation turbulence model captured accurately the heat transfer process between the vortices of averaged flow. The achieved temperature distribution was in better agreement with the experimental observations than those of RANS turbulence

models. These results have stimulated further numerical research of the applicability of the LES turbulence model for the typical recirculated flows systems (also in channel induction furnaces (64)).

3. Measurements in the model induction crucible furnace were performed together with the analysis of the existing results of experimental investigations in order to study quantitatively the phenomenon of the low-frequency flow oscillations and to provide the base for the comparative numerical analysis. The oscillations' periods and characteristic energy values have been determined and it was found out that their intensity is extremely non-homogenously distributed inside the melt volume. Also, it was shown that the axial component of velocity oscillations has dominating role in the zone of large vortices interaction and contribute the most part to the heat and mass transfer processes.

4. The numerical analysis of the melt flow in the model induction crucible furnace has shown good agreement with the experiment in terms of the oscillations amplitude, period and spatial distribution and, therefore, confirmed the reliablity of the proposed modeling method. Additionally, these calculations provided the ability to visualize the processes taking place in the unstationary flow, and, therefore, supplemented to the understanding of vortices dynamics. The numerical studies also confirmed and extended the knowledge about the oscillations' anisotropy. The study of the mesh quality influence on the results has revealed the constraints for the application of mentioned modeling approach and determined the sufficient numerical discretization level for achieving reliable results. The particular comparison with the actual RANS two-equation models has confirmed the advantage of the LES in terms of heat and mass transfer modelling for such kind of flows.

5. The series of measurements of the temperature distribution and velocity magnitude in aluminium melt during the melting process in induction furnace with the cold crucible created the basis for the consequent numerical analysis. The obtained averaged temperature distribution has shown small

temperature difference between different flow regions. Also the presence of low-frequency temperature osciallations was captured.

6. The parametric three-dimensional electromagnetic model based on finite element method for the induction furnace with cold crucible has been created for ANSYS software and consequently coupled with the self-written code for calculating the deformation of the melt's meniscus shape formed by the electromagnetic pressure. It has been shown that melt shape form significantly influences the flow and heat exchange. The following coupled hydrodynamic and thermal numerical simulation of the Aluminium melting process has presented good agreement with the experiment in terms of the temperature distribution and characteristic velocity magnitudes. This result has provided another confirmation for the consistency of the proposed modeling approach in terms of the prediction of heat transfer proceses in recirculated flows.

7. The parametric studies of the Titan-Aluminium melting process in the IFCC performed using the developed method have shown that overheating temperature is more dependend on the external current density than on the melt's height to crucible's diameter ratio.

References

[1] P. Sagaut Large Eddy Simulation for Incompressible Flows Springer-Verlag, Berlin, 2nd Edition, 2002. ISBN 3-540-43753-3 15

[2] M. Iguchi, H. Tokunaga, H. Tatemichi Bubble and liquid flow characteristics in a Woods metal bath stirred by bottom helium gas injection *Metallurgical and Material Transactions B*, Vol. 28B, 1997, pp. 1053-1061 24

[3] B.Q. Li, J.W. Evans, and D.P. Cook An improved mathematical model for electromagnetic casters and testing by a physical model *Metallurgical and Material Transactions B*, Vol. 22B, 1991, pp. 121-134 24

[4] D. Bhunia, S. P. Mehrotra, R. Shekhar A novel probe for measuring current distribution in Wood's metal in a simulated Hall-Heroult cell *Mineral Processing and Extractive Metallurgy*, Vol. 115, No. 4, 2006, pp. 206-212 24

[5] C. Vives Effects of a forced couette flow during the controlled solidification of a pure metal *International Journal of Heat and Mass Transfer*, Vol. 31, Issue 10, 1988, pp. 2047-2062 24

[6] B. G. Thomas, Q. Yuan, S. Sivaramakrishnan, T. Shi, S. P. Vanka and M. B. Assar. Comparison of four methods to evaluate fluid velocities in a continuous slab casting mold. *Science*, vol. 267 (1995), pp. 476–483.

[7] R. Schwarze and F. Obermeier. Modelling of unsteady electromagnetically driven recirculating melt flows. *Modelling and simulation in materials science and engineering*, vol. 12 (2004), pp. 985–993. 24, 37

[8] O. Pesteanu, K. Schwerdtfeger Contribution to the Large Eddy Simulation of Flows in Electromagnetic Stirrers for Continuous Casting *ISIJ International*, Vol. 43, No 10, 2003, pp. 1556-1561 24

[9] A. Buchholz, W. Schmitz and S. Engler. Anwendung induktiver Magnetsendoren bei der Strömungsmessung in flüssigem Aluminium. *Metall*, vol. 46 (1992), no. 10, pp. 1018–1023. 75, 76

[10] F. Felten, Y. Fautrelle, Y. Du Terrail, O. Metais. Numerical modelling of electromagnetically-driven turbulent flows using LES methods. *Applied Mathematical Modelling*, vol. 28 (2004), pp. 15–27. 9, 24, 25, 47

[11] X. Wang, Y. Fautrelle, J. Etay, R. Moreau A Periodically Reversed Flow Driven by a Modulated Traveling Magnetic Field: Part I. Experiments with GaInSn *Metallurgical and Material Transactions B*, Vol. 40B, 2009, pp. 82-90 9

[12] R. Moreau. Magnetohydrodynamics. 1990, p. 76. 9

[13] J.S. Smagorinsky General circulation model of the atmosphere *Monthly Weather Review*, vol. 91 (1963), pp. 99–164 17

[14] J. Zanden, H. Simons, F.T.M. Nieuwstadt Application of large eddy simulation to open-channel flow *European Journal of Mechanics, B/Fluids*, vol. 11 (1992), pp. 337-347 18

[15] R. Schiestel Modelling and simulation of turbulent flows 2008, p.

[16] S. Zahrai, F.H. Bark, R.J. Karlsson On anisotropic subgrid modeling *European Journal of Mechanics, B/Fluids*, vol. 14 (1995), pp. 459-486 18

[17] W.M. Kays Turbulent Prandtl Number–where are we? *Journal of Heat Transfer*, vol. 116 (1994), pp. 284–295 20

[18] E.D. Tarapore, J.W. Evans Fluid Velocities in Induction Melting Furnaces:Part I. Theory and Laboratory Experiments *Metallurgical Transactions B*, Vol. 7B, 1976, pp. 343-351 23

[19] J.M. Galpin, Y. Fautrelle Liquid-metal flows induced by low-frequency alternating magnetic fields *J. Fluid Mech.*, Vol. 239, 1992, pp. 383-408 23

[20] R. Ricou and C. Vives Local velocity and mass transfer measurements in molten metals using an incorporated magnet probe. *Int. J. of Heat Mass Transfer*, vol. 25 (1982), pp. 1579-1588 23

[21] A. Cramer, C. Zhang, S. Eckert Local flow structures in liquid metals measured by ultrasonic Doppler velocimetry *Flow Measurement and Instrumentation*, Vol. 15, 2004, pp. 145-153 23

[22] W. Esmarch Zur theorie der kernlosen induktions¨ofen *Wiss. Ver¨off. D. Siemens-Konzerns*, 1932 23

[23] L. Tir Modeling the thermal field in a molten smelter charge *Magnetohydrodynamics*, Vol. 3, No. 1, 1967, pp. 81-84 23

[24] L. Tir Features of mechanical energy transfer to a closed metal circuit in electromagnetic systems with azimuthal currents *Magnetohydrodynamics*, Vol. 12, No. 2, 1976, p. 200 23

[25] Yu. Mikelson, A. Yakovich and S. Pavlov Numerical investigation of averaged MHD flow in a cylindrical region with the adoption of working hypotheses for turbulent stresses *Magnetohydrodynamics*, Vol. 14, No. 1, 1978, pp. 42-49 12, 23

[26] Y. Fautrelle Analytical and numerical aspects of the electromagnetic stirring induced by alternating magnetic fields *J. Fluid Mech.*, Vol. 102, 1981, pp. 405-430 23

[27] N. El-Kaddah, J. Szekeley, E. Taberlet, Y. Fautrelle Turbulent Recirculating Flow in Induction Furnaces: A Comparison of Measurements with Predictions over a Range of Operating Conditions *Metallurgical Transactions B*, Vol. 17B, 1986, pp. 687-693 23

[28] Ben Q. Li A finite-element analysis of magnetically driven recirculationg flow in electromagnetic near net shape casting *Journal of Materials Processing Technology*, Vol. 55, 1995, pp. 351-359 23

[29] A. Bojarevics, V. Bojarevics, Yu. Gelfgat, K. Pericleous Liquid metal turbulent flow dynaics in a cylindrical container with free surface: experiment and numerical analysis *Magnitnaja Gidrodinamika*, Vol. 35, No 3, 1999, pp. 258-277 23, 24

[30] K. Heyerichs, A. Pollard Heat transfer in separated and impinging turbulent flows *Int. J. Heat Mass Transfer*, Vol. 39, No 12, 1996, pp. 2385-2400 24

[31] B.E. Launder and D.B. Spalding Lectures in mathematical models of turbulence. *Academic Press Inc*, 1979 12, 51

[32] D.C. Wilcox Turbulence modeling for CFD *DCW Industries, Inc, La Canada, California*, 1998 14

[33] P.R. Spalart, W-H. Jou, M. Strelets, S.R. Allmaras Comments on the feasibility of LES for wings, and on a hybrid RANS/LES approach *Advances in DNS/LES*, 1997, pp. 137-147 19

[34] E. Baake Grenzleistungs- und Aufkohlungsverhalten von Induktions-Tiegelöfen. PhD Thesis. *VDI-Verlag*, 1994 47, 75

[35] A. Eggers Untersuchungen der Schmelzströmung und des Wärmetransports im Induktions-Rinnenofen. PhD Thesis. *VDI-Verlag*, 1993 3, 27

[36] L.D. Landau, J.M. Lifschitz Gidrodinamika *3rd ed., Nauka, Moscow*, 1986, pp. 63-65 65

[37] W. Frost, T. Moulden Handbook of turbulence *Plenum Press, New York*, 1977, p. 536 51

[38] V. Yakhot, S.A. Orszag Renormalization group analysis of turbulence. I. Basic theory *Journal of Scientific Computing*, Vol. 1, Num. 1, 1986, pp. 3-51 14

[39] A. Yakhot, S. A. Orszag, V. Yakhot and M. Israeli Renormalization group formulation of large-eddy simulations *Journal of Scientific Computing*, Vol. 4, Num. 2, 1989, pp. 139-158 18, 56

[40] E. Westphal, A. Muiznieks, A. Mühlbauer Electromagnetic Field Distribution in an Induction Furnace with Cold Crucible *IEEE Transactions on Magnetics*, Vol. 32, No. 3, 1996, pp. 1601-1604 77

[41] G. Jingjie, S. Yanqing, J. Jun, D. Hongsheng, L. Yuan, R. Zhijiang Mechanism of skull formation during induction skull melting of intermetallic compounds *Int. J. Cast Metals Res.*, Vol. 12, 1999, pp. 35-40 89

[42] S. Yanqing, G. Jingjie, J. Jun, L. Guizhong, L. Yuan Composition control of a TiAl melt during the induction skull melting (ISM) process *J. of Alloys and Compounds*, Vol. 334, 2002, pp. 261-266 89

[43] J. Szekeley, S. Asai The general mathematical statement of tubulent recirculatory flows *Trans. ISIJ*, Vol. 15, 1975, pp.270-275 23

[44] R. Kageyama, J.W. Evans A mathematical model for the dynamic behavior of melts subjected to electromagnetic forces: Part I. Model development and comparison of predictions with published experimental results *Metallurgical and Material Transactions B*, Vol. 29B, 1998, pp.919-928 24

[45] R. Kageyama, J.W. Evans A mathematical model for the dynamic behavior of melts subjected to electromagnetic forces: Part II. Measurement of surface waves and comparison with predictions of the mathematical model *Metallurgical and Material Transactions B*, Vol. 30B, 1999, pp.331-339 24

[46] D. R. Sadoway, J. Szekely A new experimental technique for the study of turbulent electromagnetically driven flows *Metallurgical and Material Transactions B*, Vol. 11B, 1980, pp.334-336 23

[47] V. Bojarevics, G. Djambazov, R. A. Harding, K. Pericleous, M. Wickins. Investigation of the cold crucible melting process: experimental and numerical study. *Magnetohydrodynamics*, vol. 39 (2003), no. 4, pp. 395–402.

[48] J. Fort, M. Garnich, N. Klymyshyn Electromagnetic and Thermal-Flow Modeling of a Cold-Wall Crucible Induction Melter *Metallurgical and Material Transactions B*, Vol. 36B, 2005, pp. 141-152

[49] A.Jakovich, A.Mühlbauer Use of k-ϵ turbulence model for calculation of flows in coreless induction furnaces *Progress in Astronautics and Aeronautics*, Vol. 162, 1994, pp. 323-336 24

[50] E. Baake, A. Mühlbauer, A. Jakowitsch, W. Andree Extension of the k-e Model for the Numerical Simulation of the Melt Flow in Induction Crucible Furnaces *Metallurgical and Material Transactions B*, Vol. 26B, 1995, pp. 529-536

[51] Induction Melting of Metals in Cold, Self-Lined Crucibles *US Patent* 3,775,091, 1973 69

[52] Cold crucible *US Patent* 4,058,668, 1977 69

[53] N. Nikiforova, S. Pavlov, L. Tir Calculation of Electromagnetic, hydrodynamic, and energy characteristics of induction furnace with cold crucible on basis of two-dimensional model *Magnetohydrodynamics*, Vol. 20, No. 2, 1984, pp. 191-199 71

[54] A. Gagnoud, I. Leclercq Electromagnetic modelling of induction melting devices in cold crucible *IEEE Transactions on Magnetics*, Vol. 24, No. 1, 1988, pp. 573-575 71

[55] T. Tanaka, K. Kurita, A. Kuroda Mathematical Modelling for Electromagnetic Field and Shaping of Melts in Cold Crucible *ISIJ International*, Vol. 31, No. 4, 1991, pp. 350-357 71

[56] P.-R. Cha, Y.-S. Hwang, Y.-J. Oh, S.H. Chung, J.-K. Yoon Numerical Analysis on Cold Crucible Using 3D H-ϕ Method and Finite Volume Method with Non-staggered BFC Grid System *ISIJ International*, Vol. 36, No. 9, 1996, pp. 1157-1165 71

[57] K. Iwai, S. Asai The effect of design parameters on the magnetic field distribution around a cold crucible and the heat generation rate in it *Modelling Simul. Mater. Sci. Eng.*, Vol. 3, 1995, pp. 473-484 71

[58] H. Tsuboi, M. Tanaka, F. Kobayashi, T. Misaki Three-dimensional Eddy Current Analysis of Induction Melting in Cold Crucibles *IEEE Transactions on magnetics*, Vol. 29, No. 2, 1993, pp. 1574-1577 71

[59] M. Enokizono, T. Todaka, K. Yokoji, Y. Wada, I. Matsumoto Three-Dimensional Moving Simulation of Levtation-Melting Method *IEEE Transactions on Magnetics*, Vol. 31, No. 3, 1995, pp. 1869-1872 71

[60] V. Bojarevics, K. Pericleous, and M. Cross Modeling the Dynamics of Magnetic Semilevitation Melting *Metallurgical and Materials Transactions B*, Vol. 31, No. 1, 2000, pp. 179-189 71

[61] E. Baake, B. Nacke, F. Bernier, M. Vogt, A. Muhlbauer, M. Blum Experimental and numerical investigations of the temperature field and melt flow in the induction furnace with cold crucible *COMPEL: The Int. J. for Comp. and Math. in Electrical and Electronic Eng.*, Vol. 22, Iss. 1, 2003, pp. 88-97 71

[62] V. Bojarevics, K. Pericleous, R. A. Harding, M. Wickins The development and experimental validation of a numerical model of an induction skull melting furnace *Metallurgical and Materials Transactions B*, Vol. 35, No. 4, 2004, pp. 785-803 71

[63] E. Taberlet and Y. Fautrelle Turbulent stirring in an experimental induction furnace *Journal of Fluid Mechanics*, Vol. 159, 1985, pp. 409-431 23

[64] E. Baake, M. Langejuergen, M. Kirpo, A. Jakovics Analysis of transient heat and mass transfer processes in the melt of induction channel furnaces using LES *Magnetohydrodynamics*, Vol. 45, No. 3, 2009, pp. 385-391 94